FACULTY OF TECHNOLOGY

THE OPTIMIZATION OF THE SCALE GROWTH MODEL FOR LINE ANNEALING IN STAINLESS STEEL PRODUCTION

Karri Vaarala

Master's programme of process engineering

Master's thesis

July 2021

TIIVISTELMÄ
OPINNÄYTETYÖSTÄ Oulun yliopisto Teknillinen tiedekunta

Koulutusohjelma (kandidaatintyö, diplomityö) Prosessitekniikka		Pääaineopintojen ala (lisensiaatintyö)	
Tekijä Vaarala Karri Joonas Mikael		Työn ohjaaja yliopistolla Laukka A., TkT ja Heikkinen E-P., TkT	
Työn nimi Nauhahehkutuksen hilseenkasvumallin optimointi ruostumattomien terästen valmistuksessa			
Opintosuunta Prosessimetallurgia	Työn laji Diplomityö	Aika Heinäkuu 2021	Sivumäärä 104

Tiivistelmä

Tämän työn tavoitteena oli optimoida teollisessa mittakaavassa käytössä oleva ruostumattoman teräksen loppuhehkutuksen hilseenkasvumalli. Työtä varten tehdyn tutkimuksen pääpainoina olivat hehkutuslämpötilan ja hehkutusuunissa vallitsevan atmosfäärin vaikutus hilseenkasvun määrään, jonka lisäksi hehkutusajan vaikutusta hilseenkasvuun tutkittiin mikroskopoimalla. Kokeellisen työn tulokset sovitettiin kirjallisuusselvityksessä löydettyihin malleihin, joiden ansiosta hilseenkasvua pystytään ennustamaan termodynaamisesti. Työtä varten suoritettiin kirjallisuuskatsaus liittyen teollisen mittakaavan loppuhehkutukseen, teollisissa prosesseissa käytettäviin polttoaineisiin sekä niiden vaikutuksista mm. hilseenkasvuun sekä olemassa oleviin matemaattisiin mallinnuskeinoihin ja niiden hyödyntämiseen.

Kokeellisessa osuudessa simuloitiin kylmävalssattujen AISI 304, AISI 309 sekä AISI 441 loppuhehkutusta hehkutus- ja peittauslinjalla. Kokeiden tarkoituksen oli simuloida hilseenkasvua tuotantolinjalla ja saada tietoa hehkutusolosuhteiden vaikututuksista muodostuvan hilseen määrään. Hehkutusolosuhteina käytettiin 950 - 1250 °C lämpötiloja, 15 minuutin pitoaikoja sekä kolmea eri atmosfääriä, jotka simuloivat maakaasun polttoa ilmalla ja happirikastetulla ilmalla sekä vedyn polttoa happirikastetulla ilmalla. Lisäksi AISI 304 ruostumattomalle teräkselle tehtiin pysäytyskokeita, joiden pitoajat olivat yksi, viisi, kymmenen ja 15 minuuttia hehkutusajan vaikutuksen tutkimiseksi. Kokeet suoritettiin pystysuorassa putkimaisessa hehkutusuunissa, ja näytteiden massaa mitattiin jatkuvasti uunin yläpuolelle kiinnitetyn vaa'an avulla. Mikroskopoinnissa käytettiin FESEM-EDS-laitteistoa.

Suurimassa osassa tapauksia korkeamman lämpötilan havaittiin aiheuttavan enemmän hapettumista. Yksikään simuloiduista atmosfääreistä ei noussut selkeästi kaikista eniten hapettumista aiheuttavaksi, vaan tilanne vaihteli tapauskohtaisesti. Pidemmän hehkutusajan havaittiin aiheuttavan enemmän hapettumista. Verrattaessa ilmalla poltettua maakaasua ja happirikastetulla ilmalla poltettua vetyä hehkutuksen polttoaineena, ei havaittu merkittävää eroa hilsekerrosten koostumuksen tai syvyyden suhteen.

Kokeellisesta työstä saadut tulokset sovitettiin toimiviksi havaittuihin malleihin, jonka tuloksena saatiin laskettua aktivaatioenergiat ja taajuustekijät Arrhenius-yhtälön avulla. Näiden tuloste ansiosta hehkutuksessa syntyvän hilseen määrä pystytään ennustamaan termodynaamisesti, ja tuloksia voidaan sovittaa teolliseen mittakaavaan.

Muita tietoja

Asiasanat: hehkutus, hilse, kasvu, malli, ruostumaton teräs

ABSTRACT
FOR THESIS

University of Oulu Faculty of Technology

Degree Programme (Bachelor's Thesis, Master's Thesis) Master's programme of process engineering	Major Subject (Licentiate Thesis)
Author Vaarala Karri Joonas Mikael	Thesis Supervisor Laukka A., D.Sc. (Tech) and Heikkinen E-P., D.Sc. (Tech)

Title of Thesis

The optimization of the scale growth model for line annealing in stainless steel production

Major Subject	Type of Thesis	Submission Date	Number of Pages
Process Metallurgy	Master's Thesis	July 2021	104

Abstract

The aim of this thesis was to optimize an industrial scale growth model for stainless steel annealing. The focus of the experimental work conducted for this thesis was on the effect of annealing temperature and atmosphere within the annealing furnace on the amount of scale formed during annealing. In addition, the effect of annealing time was studied through the means of microscopy. The results of the experimental work were fitted into mathematical models discovered during the literature review. Thanks to this, the amount of scale formed during annealing can now be predicted thermodynamically. A literature review was performed for this thesis on industrial scale final annealing, the fuels used in industrial scale processes and their effects on e.g., the scale growth during the process and existing mathematical modelling methods and appliances.

The experimental work consisted of simulating the annealing of cold rolled AISI 304, AISI 309 and AISI 441 on an industrial scale annealing- and pickling line. The purpose of the experiment was to simulate the scale growth taking place on an industrial scale annealing furnace and gather information on the effect of annealing temperature and atmosphere within the furnace on the amount of scale formed. Studied annealing temperatures ranged between 950-1250 °C and the holding time was 15 minutes. Three different atmospheres were used, simulating the usage of liquid natural gas burned with both air and oxygen enriched air as well as hydrogen burned with oxygen enriched air. In addition, stoppage experiments were conducted on AISI 304 with annealing times of one, five, ten and 15 minutes to study the effect of annealing time on scale growth. The experiments were conducted in a vertical tube furnace, with a weighing scale fixed above the furnace hanging and measuring the mass of the samples. The equipment used for microscopy was a FESEM-EDS.

In most cases it was noted, that a higher temperature would cause a higher amount of oxidation. None of the simulated atmospheres were found to cause explicitly more oxidation than the other two between the studied atmospheres, and differences varied from temperature to temperature. A longer annealing time was observed to cause more oxidation, as was expected. When comparing the simulated liquid natural gas burned with air to hydrogen burned with oxygen enriched air as a fuel, no major difference was found in the morphology or depth of the scale formed.

The results from experimental work were fitted into functional models. Using the Arrhenius-equation, activation energies and frequency factors could be calculated. These results permit the thermodynamic prediction of the amount of scale formed, and their implementation to an industrial scale.

Additional Information

Keywords: annealing, growth, model, scale, stainless steel

FOREWORD

This thesis was done for the University of Oulu laboratory of process metallurgy from the 21st of February until the 14th of July 2021 for the TOCANEM project in conjunction with the Outokumpu Stainless Oy Tornio steelworks. Outokumpu Oy provided the stainless steels used in the experimental work.

I would like to thank my supervisors Aleksi Laukka and Eetu-Pekka Heikkinen and professor Timo Fabritius for providing an interesting subject to study and do thesis on. I would also like to thank laboratory technician Tommi Kokkonen for guidance during the experimental work and laboratory engineer Riku Mattila for helping me with practicalities related to working at the research unit. In addition, I would like to thank the whole Process Metallurgy Group for interesting conversations and advice an anything I needed.

I would also like to thank Outokumpu Stainless Oy for providing me with the opportunity to work for them for four summers, all the way throughout my studies. I would also like to thank them for their involvement in both of my Bachelor's and Master's theses. The people working at the AP2 -line kept me motivated, and it was an honour to return to Tornio and work with them every summer.

Lastly, I would like to thank my friends and family, who helped me through the journey known as university. Without your support, I would have given up after my first year. I would especially like to thank my father for teaching me the importance of hard work and never giving up.

Oulu, 19.7.2021

Karri Vaarala

TABLE OF CONTENTS

ABBREVIATIONS AND SYMBOLS USED

α	mass per surface area
Ωox	Volume of formed oxide per diffused ion
ϕM	Matt potential
ΔG^0	Free energy
Δm	Change in mass
A	Frequency factor
a	Distance between maximum and adjacent minimum of an energy barrier
dm	Change in mass
dt	Change in time
E	Electrostatic field in oxide film
e	Euler's number
E_a	Activation energy
g	Stoneham-Tasker-parameter
k	reaction rate constant
k_c	Cubic reaction rate constant
k_p	Parabolic reaction rate constant
k_q	Quadratic reaction rate constant
$k_{1.7}$	Reaction rate constant for the "1.7"-model
L	Oxide thickness
m	Mass
R	Universal gas constant
T	Temperature

n	Number of ions in unit area
t	Time
v	Ioniq attempt frequency of a jump
W	Rate limiting energy barrier
AISI	American Iron and Steel Institute
EBSD	Electro Backscatter Diffraction
EDS	Energy-Dispersive X-ray Spectroscopy
FESEM	Field Emission Scanning Electron Microscope
LNG	Liquid natural gas
LPG	Liquefied petroleum gas
NO_x	Nitrogen oxides
RAP5	Rolling, Annealing and Pickling line in Outokumpu Tornio Works
TGA	Thermo Gravimetric Analysis
TOCANEM	Towards Carbon Neutral Metals project
WDS	Wavelength-dispersive spectroscopy

1. INTRODUCTION

Cold rolling of a stainless steel strip causes strong consolidation. As a result, the yield strength of the strip is very high and close to tensile strength, and ultimate elongation is low. Annealing processes use various types of energy sources due to emission requirements, availability and market price. Lowering of emissions is the strongest driving force for studying new energy sources, but the atmosphere within the furnace affect the scaling significantly enough to mandate studies on the effects of these atmospheres. Scale forms on the surface of the stainless steel strip due to oxidation in high temperatures. This causes material losses and creates a need for a process to clean the surface of the scale. This process is called pickling, and it can take place directly after annealing and cooling, or further down the process chain. However, pickling must be performed before surface finishing processes, e.g. final rolling, in order to prevent damage on process equipment and to create a clean surface. Different atmospheres inside annealing furnaces effect the scaling in different ways. The amount of scale formed can differ, as well as the morphology of the scale formed. These together affect the properties and processability of the stainless steel strips further down the process chain, e.g. surface quality and effectiveness of pickling.

The aim of this thesis is to optimize an already existing scale growth model used in stainless steel production in an annealing-pickling line. The effects of temperature, annealing time and atmosphere are studied. The main focus is on the amount of scale formed in the experiments. The results of these experiments are used to optimize the scale growth model.

The three steel grades studied in this thesis are AISI 304, AISI 309 and AISI 441. The samples were provided by Outokumpu Stainless Ltd.

2. FINAL ANNEALING AND PICKLING LINE

There are four annealing and pickling lines in the Cold Rolling Mill 1 of the Outokumpu Tornio steelworks, and also one in the RAP5. Two of the four lines are only used for annealing and pickling cold rolled steel strips, whereas the other two lines are capable of processing both hot and cold rolled strips.

The annealing and pickling line is a continuous production line, which means that the production only halts for maintenance or when the temperatures of the furnace and/or acids used in pickling need to be adjusted. It is a crucial part in steel production, and especially important in the case of stainless steel, where the aesthetics of the product are often of the upmost importance. Annealing and pickling take place after hot and cold rolling, and sometimes in the middle of cold rolling. This thesis is aimed towards stainless steel which has already been cold rolled, so the annealing and pickling of hot rolled strips will not be considered here. According to Metallinjalostajat (2014), the aim of annealing and pickling is to soften the steel strip after cold rolling, to shape the size of steel grains and to form the passive protective layer of chromium oxide, which gives stainless steel its ”stainless” properties. The softening of the steel and the wanted grain size are achieved through a phenomena known as recrystallization. A depiction of the final annealing and pickling line is presented in **Figure 1.**

The operation of the annealing and pickling line in Outokumpu Tornio works starts from preparation, where non-rolled ends are cut from each end of the coil. The head of the prepared coil is welded to the tail of the previous coil, which is currently being processed. After welding the strip goes through grease removal, where the oil used as lubricant and coolant in cold rolling is removed. To ensure a constant operation speed of the furnace, there are two accumulators, one before the furnace, and another one after pickling. The strip goes through the accumulator and enters the furnace, where the annealing takes place, i.e. where the grain size is altered, and scale forms the surface of the strip. This scale is washed off in the pickling phase with mixed acids, which consist of e.g. nitric acid and hydrofluorid acid. Any leftover acids are washed from the steel’s surface with water, and the dried strip is inspected for surface defects by an operator, in some cases with the assistance of an automatic surface inspection system. Finally the strip is reeled

into a coil and sent forward to be further processed, e.g. finishing rolling or cutting into final length and width.

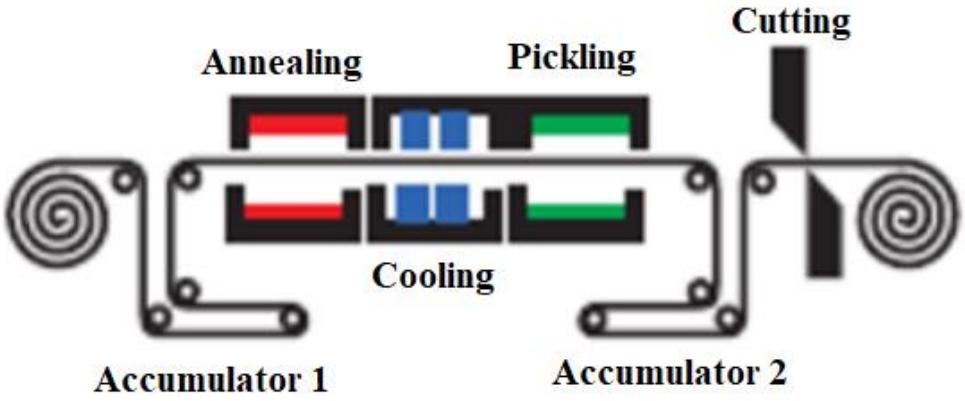

Figure 1. Final Annealing and Pickling, modified from Palosaari (2020).

2.1 Scale formation in annealing

Heating a strip in a furnace causes a layer of oxide called scale to form on the surface. The scale has both wanted and unwanted properties depending on the steel's composition and the process parameters of the furnace. Wanted and unwanted properties are antonyms of each other, and they include e.g. continuity of the scale layer, mechanical strength and adherence. A continuous, uniform scale layer stabilizes the speed of the oxidation, so the strip surface does not oxidate excessively. Strong enough mechanical strength is needed to keep the scale from spalling of flaking off, for the uncovered area would oxidate even deeper. For descaling in the pickling phase a low enough adherence is needed in order to produce a clean surface. Achieving these wanted properties reduce the production costs directly by lowering production losses and producing a high quality product on the first try. It also affects the customer perception as they receive the high quality material they have ordered on time.

Wagner's theory of oxidation is often used while discussing the growth of an oxide film or layer on a metallic surface due to thermal oxidation. Berthod (2005) presents Wagner's theory in the form found in Equation (1) and its integrated form found in Equation (2).

$$\frac{dm}{dt} = \frac{k}{m} \tag{1}$$

Here dm is the change in mass, dt is the change in time, k is the reaction rate constant and m is mass.

$$m = \sqrt{2 \cdot k} \cdot t^{\frac{1}{2}} \tag{2}$$

Again, m is mass and k is the reaction rate constant as above, and t is time.

The oxidation rate is controlled by ionic transport across the film happening due to the combined effects of electric fields and concentration gradients. In most cases the diffusive properties of the oxide control the rate constant in parabolic growth kinetics presented by Xu et al. (2012) in Equation (3).

$$\frac{dL}{dt} \propto \frac{1}{L} \tag{3}$$

where L is the thickness of the oxide film. According to Wagner's theory, self-diffusion of ions across the oxide film is the slowest of the relevant processes and is therefore the rate limiting process.

However, the relation between diffusion constants and growth rate have not been properly confirmed experimentally, thus often leading to stronger oxidation than expected. According to Atkinson (1988), even with fast diffusion along grain boundaries, the oxidation is too slow to account for the measured oxidation growth rates. Also, impurities have a significant influence on short circuit transport, for one of their important beneficial roles is blocking short circuit diffusion. Wagner's theory has led to the creation of other, sometimes more advanced or more specific models e.g. the Mott-Cabrera, Walters and Zegers-van Duijinhoven models.

The oxidation of metal is a chemical reaction, and it will take place in appropriate conditions (temperature, partial pressures of gases) in the presence of gasous oxygen. For oxidation to occur, the reaction must produce a reduction in the free energy, ΔG^0. To

calculate the free energy of an oxidizing reaction, we need a formula. An example of a metal oxidazing reaction is presented in Equation (4):

$$\left(\frac{2x}{y}\right) M + O_2 \rightarrow \left(\frac{2}{y}\right) M_x O_y \tag{4}$$

where M is a metal, O is oxygen and x and y are integers. Knowing the formula for the oxidazing reaction, the free energy can be calculated utilizing Equation (5):

$$\Delta G^0 = -\mathrm{RT} \ln \left(\frac{a_{M_x O_y}^{\frac{2}{y}}}{a_M^{\frac{2x}{y}} \cdot p(O_2)} \right) \tag{5}$$

Where ΔG^0 is the free energy, R is the universal gas constant, T is the temperature, ln is the natural logarithm, a is the acticity of metal or oxide and p is the partial pressure of oxygen.

A conventional graphic way of predicting the stability of an oxide in the prevailing conditions is through the use of an Ellingham diagram. For ease of studying, different variations have been created with different amounts of elements and their oxidizing reactions.

3. ENERGY SOURCES IN FURNACE PROCESSES

The annealing of stainless steels in a furnace requires tremendous amounts of energy due to high temperatures. According to North American Stainless (2010a), best corrosion resistance for austenitic stainless steels e.g. AISI 304 is achieved with annealing temperatures higher than 1037 °C. For ferritic stainless steels e.g. AISI 441 appropriate annealing temperatures range between 760 °C and 830 °C according to North American Stainless (2010c). For a long time, liquefied petroleum gas (LPG) has been used as the primary fuel in all furnace processes in steel production. Liquefied petroleum gas is a by-product of petrochemical industries, and it consists of propane and butane. In recent years, other ways of bringing energy into the process have gained popularity. These new methods include burning of LNG (which consists mainly of CH_4), burning of hydrogen and electric induction. (US patent US4713154A)

Hydrogen is considered a very clean alternative compared to carbon containing gases, for the main burning product is water vapour. The big problem with production of hydrogen is the energy consumption. Hydrogen is produced from water using electrolysis, which requires tremendous amounts of energy. If the use of hydrogen as fuel in furnace processes is to make any sense, it would have to be produced in a zero emission manner. Water can be found almost anywhere in the world, but the energy would have to be created in an eco-friendly way, such as wind, hydro or nuclear power. The source of power would also have to be stable, meaning enough power should be available at all times. As some areas lack consistent strong winds and water streams, nuclear power must be considered as an option. This also has its radioactive disadvantages. Therefore, hydrogen is considered as a possible fuel of the future.

Electric induction is another intriguing way of annealing steels, for it affects annealing of steels in many ways, i.e. the growth of surface scales and grains may differ strongly from other technologies. There aren't many industrial scale induction furnaces as of today, and its main challenge is also the stable source of energy. The source of energy faces the exact same challenges as the production of hydrogen. Because of this, electric induction is also considered a possible technology of the future. Electric induction may also be combined with other annealing methods, creating a hybrid technology.

The most viable way of reducing emissions as of today is to switch from burning liquid propane or butane to LNG. The infrastructure already exists, which makes the conversion inexpensive. The main difference is the burners inside furnace, for they will need to be exchanged in almost every case. Compared to other available technologies, switching to LNG is an inexpensive option, but a temporary one. It makes sense for companies to wait for the development of cleaner fuels, infrastructure etc.

When methane is burned in optimal stoichiometric conditions, it reacts with oxygen forming CO_2 and H_2O according to Equation (6).

$$CH_4\ (g) + 2\ O_2\ (g) \rightarrow CO_2\ (g) + 2\ H_2O\ (g) \quad (6)$$

In reality, methane is burned with air, which consists of nitrogen, oxygen and many other components of lower quantities. Therefore, CO_2 is not the only environmentally hazardous by-product of methane combustion. Additional by-products include CO, NO_x and others. The formation of these by-products can be prevented e.g. by process optimization, filtration of product gases and by using more highly refined fuels and other materials. Particularly the formation of NO_x gases can be reduced by optimizing combustion taking place in high temperature processes, e.g. by providing enough oxygen or optimizing the temperature of the flame.

The exhaust gases are filtered, and some parts may be recovered for different purposes, e.g. CO may be used as a reducing agent in reduction processes, as a fuel in high temperature processes or to produce chemicals, such as ethanol.

Previous studies have compiled some of the effects of swirling intensity on the combustion of air-methane mixtures. Higher swirling intensity causes the mixing rate air-methane mixture to increase. According to information compiled by Hosseini et al., (2020), combustion may be enhanced by increasing the swirling rate of the inlet airflow. This results in lower formation of NO_x and soot to some extent, decrease in exhaust temperatures and increase in flame temperature. It was also noted that when the swirling number was increased, the flame started to approach the burner inlet. The affects of the velocities of air and fuel and addition of hydrogen have been studied by Patel & Shah (2018). Higher swirling caused by higher air and fuel velocities caused the flame to be shorter, wider and more stable than those with lower velocities. They found out that hydrogen would decrease the length and increase the temperature of the flame, but in the

non-swirling case, it would increase the formation of NO_x. It was noted by (Hosseini et al., 2020), that it is crucial to determine the correct swirling number when creating a mathematical model for combustion flows. The results of their study compiled that increasing the swirling number would lead to a uniform temperature and heat flux distributions throughout the furnace, increase in the heat exchange area of the flame, increase in the residence time of products in the furnace which leads to lower heat losses and also creation of internal and external recirculation zones in the flow. As predicted before, it would also reduce the creation of hazardous NO_x pollutants.

3.1 Effect of fuel on atmosphere

Airaksinen (2019) has compiled some of the effects of atmosphere on scale growth. The atmosphere inside an annealing furnace affects the characteristics of the formed scale layer: thickness, morphology and composition. These characteristics in return affect the pickling phase, which takes place after annealing. The effects seen in the pickling phase are the loss of metal and picklability. The oxidizing atmosphere is a result of combustion of fuels. The properties of the formed atmosphere are dependant on such factors as fuel used, oxidizing agent, e.g. oxygen, CO_2 or water vapour and their ratios. Different fuels form different kinds of atmospheres, and the amount of oxygen present inside the furnace affects the oxidation as well. Annealing may also be conducted in a vacuum or in inert atmospheres with zero or very low quantities of oxygen, Using a vacuum or an inert atmosphere causes the oxidation to be very controllable or even non-existing. Inert atmospheres may be created using e.g. argon, helium or nitrogen, but using these atmospheres comes with high operational costs.

When it comes to pickling efficiency and morphology of the formed scale, the amount of oxygen and water vapour matters. With a high enough oxygen content (min. 2 - 3 %) the pickling efficiency of the scale is improved. With holding times shorter than 30 minutes, the amount of water vapour in the atmosphere does not effect the scale growth significantly due to the similarity of oxidation mechanisms. The composition of the formed scales are also similar. With longer holding times the difference is greater. In an atmosphere with less water vapour the oxidation is not as strong and it is more linear than

in an atmosphere with higher water vapour content. With higher water vapour contents the oxidation starts off slow and switches over to breakaway-oxidation in later stages. In conclusion, water vapour causes faster oxidation, and higher amounts of water vapour amplify this effect.

When using LNG as a fuel a sufficient amount of oxygen is needed. If the air/CH_4-ratio is ≤ 9.53, the initially formed oxide layer does not protects the metal from oxidizing further. This is due to a too great oxidation speed, which forms an oxide layer consisting of iron oxide. The oxide layer consists of two separate parts, the upper one consisting of wüstite and the lower one consisting of iron spinel. With higher amounts of oxygen the formation of the initial layer is slower, and the formed layer is a protective chromium oxide film. However, with high enough holding times this protective layer is destroyed, and iron oxide starts to form, promoting further and faster oxidation.

It is also possible to use an atmosphere which causes zero to none chemical reactions on the surface of the metal. Such atmospheres are described with the term ”inert.” Using a vacuum is also possible. In a vacuum there are only small amounts of gases which are stuck to the surface of the metal causing very little chemical reactions. Scale formed while using an inert atmosphere of nitrogen consists of two layers, the upper one being iron oxide and the lower one being iron and chromium spinel ($(Fe,Cr)_3O_4$). Oxidation in a vacuum may occur due to residual oxygen on the surface of the steel. Annealing in 600 °C with a holding time of one hour forms a scale with two layers, the higher one being rich with iron and the lower one being rich with chromium. When using the same temperature and holding time in a regular air atmosphere with atmospheric pressure the formed scale consists of four differing layers of oxide. Much alike with vacuum annealing, the highest layer is rich with iron and the lowest layer is rich with chromium.

4. MODELLING OF OXIDATION KINETICS AND ARRHENIUS EQUATIONS

According to Martin (2007), in industrial scale appliances, different operating parameters, e.g. temperature, annealing time and partial pressures of gases, are limited to a very restricted range. These parameters can be used as variables when mathematically modelling processes, e.g. when creating and optimizing a scale growth model for line annealing. One way of developing these models is to change the operating parameters and studying and applying the results, leading to more optimized process operation. Complicated models used in Online and automatic applications require sophisticated calculations, which control processes with speeds unattainable by humans via manual calculations and applications. Qualities such as the thickness of oxide layers bring their own twist into the creation of models. A model may work when predicting the formation of a thick oxide layer, but is impractical in predicting the formation of a thinner layer. A model may be adjusted e.g. by adding terms into the equations.

Arrhenius equation is used to describe the relation between the rate of reaction and temperature for many chemical and physical reactions. A common way of presenting the equation is as follows:

$$k = A \cdot e^{-\frac{E_a}{R \cdot T}} \tag{7}$$

where k is the kinetic reaction rate, A is the rate constant, e is Euler's number, E_a is the activation energy, R is the universal gas constant and T is temperature. The equation can be utilized in modelling e.g. temperature variation of diffusion coefficients and creep rates. The equation can be modified into more useful forms, e.g. by taking the logarithm of both sides of the equation:

$$\ln(k) = \ln(A) - \frac{E_a}{R \cdot T} \tag{8}$$

Oxidation in metals occurs when oxygen in the prevalent atmosphere reacts with the exposed metal. First the reaction forms an oxide layer on the surface of the metal with the thickness of one atom. After this, the oxide starts to nucleate into dislocations and grain boundaries. The oxygen needed for this is provided through diffusion through the already

formed oxide layer. The growth of these oxide particles causes them to eventually merge into bigger particles, forming a somewhat uniform oxide layer.

Different oxidation kinetics models have been compiled by (Martin, 2007). Some simple models are used to relate kinetic data to possible underlying processes. Most models predict oxidation behaviour leading to a prediction of oxidation velocity, often marked $\frac{dL}{dt}$, as a function of thickness, L. The simplest models simply only look at $\frac{dL}{dt}$ vs. L. It is common for these simple models to make assumptions in order to simplify the operation, e.g., as assuming the chemical potential of oxygen as a constant. For this, these models lack accuracy in real world appliances, but they can guide actions into the right direction. One convenient guide for comparing oxidation velocity to thickness was created by Stoneham and Tasker in 1987. The guide is a dimensionless logarithmic derivative of the oxidation velocity in relation to thickness:

$$g = \frac{-d[\log\left(\frac{dL}{dt}\right)]}{d[\log L]} \tag{9}$$

The Mott-Cabrera model is explained by (Ermoline & Dreizin, 2011). This model describes the tunneling of electrons from a metal surface. through a thin oxide layer to the oxide/gas surface. The model can be written in the following form:

$$\frac{dL}{dt} = \Omega_{ox}\, nv \exp\left(-\frac{W}{kT}\right) \exp\left(\frac{qaE}{kT}\right) \tag{10}$$

where L is the growth rate of the oxide thickness, Ω_{ox} is the volume of the formed oxide per diffusing ion, n is the number of ions in unit area in the position to jump over the rate-limiting energy barrier W, v is the ionic attempt frequency of the jump, a is the distance between the maximum and adjacent minimum of the energy barrier, and E is the electrostatic field in the oxide film formed due to Matt potential ϕ_M. E is determined by equation (6):

$$E = -\frac{\phi M}{L} \tag{11}$$

This electrostatic field, E, can aid the injection step of the mobile species, which is presumed to be a limiting factor in the formaton of the oxide. The term ”Mott-Carbera mechanism” is often used to describe any deviation from diffusion reaction models, which is inaccurate. The model covers a precise physical mechanism, and thus is not universal.

Whereas the Mott-Cabrera is applicable to thin oxide layers, the Wagner model found below is used with thicker oxide layers. The border of a thin film is determined by (Xu et al., 2012) to be at 20 nm. They have also determined the border of a thick film to be at 1 μm.

Ionic transport models suggest that oxidation may be suppressed by a stopping field, which is formed due to a large enough difference in potential. In such cases, charged species, e.g. O^{2-}, must be involved in transportation of electrons from the metallic surface. Some models, e.g. the Walters and Zegers-van Duijnhoven model, recognize the build-up of an electric field within the formed oxide. These electric fields bias the diffusive jumps of the moving ions. Wolters' model makes two assumptions: a layer of fixed charge, Q_f, is concentrated at the distance of X_Q from the metal/oxide interface.

5. RESEARCH METHODS

5.1 Materials

In this research, the scaling of three different stainless steels, AISI 304, AISI 309 and AISI 441 in three different atmospheres with three different annealing temperatures were studied. Metalcor.de has described some of the main properties of all three steel grades studied here.

AISI 304 is considered to be the standard austenitic chromium-nickel stainless steel. It has a high corrosion resistance and easy formability. Its main users are chemical and petrochemical industries, oil industry and foodstuff industry as a hygienic material.

AISI 309 is a heat resistant austenitic chromium-nickel stainless steel. It is resistant to scaling up to 1000 °C, but it has low resistance to sulphuric acids. It is mainly used in furnace and apparatus engineering.

AISI 441 is a ferritic chromium stainless steel. Its specialty is good resistance to stress corrosion cracking. Its main use is in the automotive industry as exhaust pipes and shells for catalytic converters.

The samples were cut to appropriate sizes, approximately 28 mm · 20 mm using a Struers Secotom-10 cutter pictured in **Figure 2**. The blade used was a Struers 30A15 aluminium oxide cut-off wheel. Holes were drilled into the samples using a column drilling machine. Prior to annealing experiments, the samples were cleaned individually from grease and other surface contaminants using acetone and ethanol. They were also rinsed with deionized water and dried with paper towels before insertion into the furnace.

Figure 2. Struers Secotom-10 cutter.

5.2 Experiments

The research was performed using a Thermogravimetric analysis-furnace, also known as a TGA-furnace. The TGA-furnace was purpose built at the University of Oulu. The furnace is a vertical tube with the wanted temperature concentrated onto a small area. Gases are fed into the furnace from the bottom, and they exit from the top into a vent. The gases are electrically preheated, and water vapour is supplied by heating water pumped to a pre-heater by a peristaltic pump. The atmosphere inside the furnace is created and altered using gas streams fed through computer-controlled mass flow controllers. The mass of the sample is measured in real time using a scale fixed directly above the furnace. The temperature of the furnace is measured and adjusted constantly using a thermocouple. The TGA-furnace is pictured in **Figure 3.**, and a schematic picture of the furnace is found in **Figure 4.** The main focus was on the change of the samples' mass as a result of scale formation as a function of time.

Figure 3. TGA-furnace.

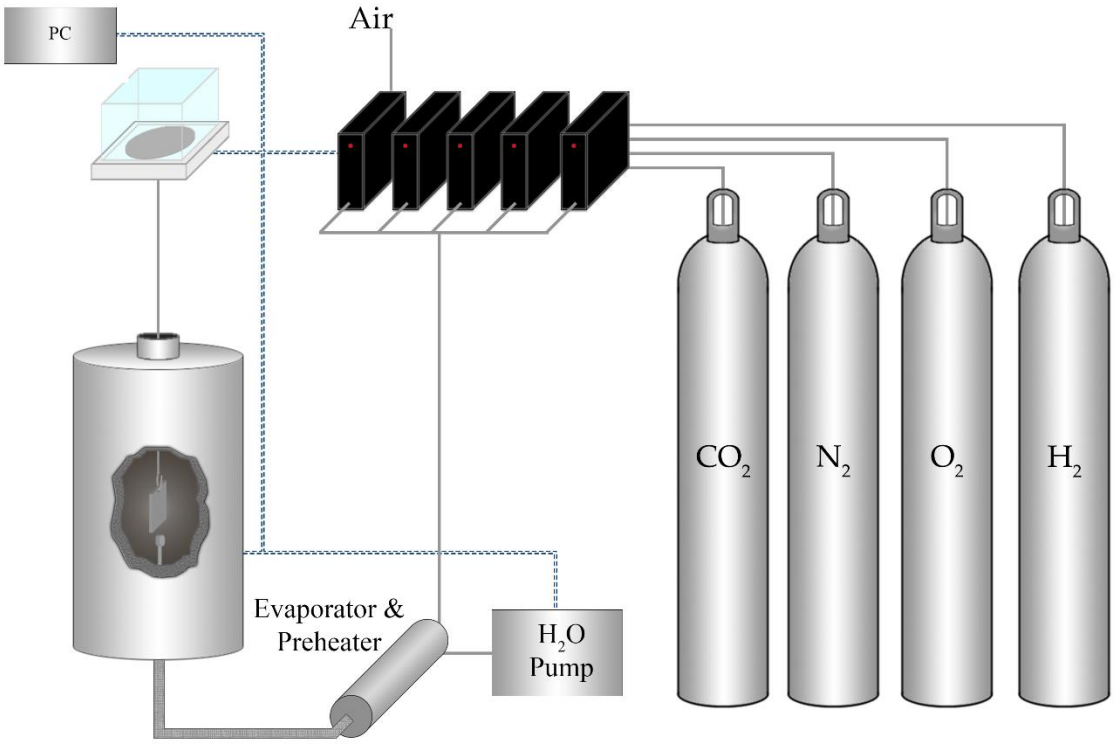

Figure 4. A schematic view of the TGA-furnace system.

The samples were hung from a platinum wire, and a short Al_2O_3 tube was placed on the wire to prevent contact between the samples and the platinum wire. A contact between the sample and the wire could have resulted in an unwanted chemical reaction. Platinum wire and Al_2O_3 were used, as they would not react to the atmospheres inside the furnace. An example of a sample hanging from a platinum wire is pictured in **Figure 5.** The samples were placed inside the furnace by hand using protective gloves and safety goggles. Inserting the sample inside the furnace decreased the furnace's temperature, and there was a waiting period when the temperature rose back up to the wanted level. During this time nitrogen was injected into the furnace to create an inert atmosphere to prevent the sample from oxidizing before the start of the experiment. After the correct temperature was reached, the experiment was started.

Figure 5. An uncleaned ferritic sample hanging from a platinum wire with Al_2O_3 tubes preventing contact between the sample and the wire.

Each experiment lasted 15 minutes, after which the samples were cooled in room temperature and weighed. The highest temperature experiment for each steel grade and atmosphere were repeated to validate the results. In addition, some steel grades required several repeated experiments due to poor repeatability. The used temperatures for the austenitic steels were 1200, 1225 and 1250 °C. The temperatures used for the ferritic steels were lower than for the austenitic steels as per in industrial applications, 950, 1000 and 1050 °C. The annealing time for all steels was 15 minutes, excluding the experiments conducted on AISI 304 samples which were to be used for studying the effect of annealing time on scale growth. Three different synthetic atmospheres were created in the TGA-furnace to simulate the atmospheres which would be created by burning methane using air or oxygen and burning hydrogen using oxygen The three atmospheres used were CH_4 Air, CH_4 Oxyfuel and H_2 Oxyfuel. CH_4 was burned both with air and pure oxygen, and H_2 was burned with oxygen. The composition of each atmosphere is presented in **Table 1.** with respective flow rates.

Table 1. TGA-oven atmosphere compositions and flow rates of each gas.

	% of flow			Flow rate (l/min)		
	CH_4 Air	CH_4 Oxy	H_2 Oxy	CH_4 Air	CH_4 Oxy	H_2 Oxy
Air	15.33	0	0	0.3066	0	0
H2O	16.1	54.521	90	0.322	1.09042	1.8
N2	60.57	0	0	1.2114	0	0
CO2	8	32.261	0	0.16	0.64522	0
O2	0	3.218	10	0	0.06436	0.2
Total	100	100	100	2	2	2

Each experiment with their respective sample IDs, steel grades, temperatures. annealing times, atmospheres and sample surface areas are presented in the research matrix in **Table 2.** The mass change of samples D1-D3 was not measured, thus there was no need to calculate their surface areas.

Table 2. The research matrix.

ID	Steel Grade	Temperature (°C)	Time (s)	Atmosphere	Area (mm^2)
A1.1	AISI 304	1200	900	CH_4 Air	1384.9
A1.2	AISI 304	1225	900	CH_4 Air	1430.6
A1.3	AISI 304	1250	900	CH_4 Air	1344.5
A1.3.5	AISI 304	1250	900	CH_4 Air	1389.3
A2.1	AISI 304	1200	900	CH_4 Oxyfuel	1366.3
A2.2	AISI 304	1225	900	CH_4 Oxyfuel	1377.9
A2.3	AISI 304	1250	900	CH_4 Oxyfuel	1377.9
A2.3.5	AISI 304	1250	900	CH_4 Oxyfuel	1366.2
A3.1	AISI 304	1200	900	H_2 Oxyfuel	1322.4
A3.2	AISI 304	1225	900	H_2 Oxyfuel	1286.6
A3.3	AISI 304	1250	900	H_2 Oxyfuel	1221.7
A3.3.5	AISI 304	1250	900	H_2 Oxyfuel	1287.7
B1.1	AISI 309	1200	900	CH_4 Air	1229.1
B1.2	AISI 309	1225	900	CH_4 Air	1506.4
B1.3	AISI 309	1250	900	CH_4 Air	1451.7
B1.3.5	AISI 309	1250	900	CH_4 Air	1198.9
B2.1	AISI 309	1200	900	CH_4 Oxyfuel	1299.6
B2.2	AISI 309	1225	900	CH_4 Oxyfuel	1196.6
B2.3	AISI 309	1250	900	CH_4 Oxyfuel	1314.8
B2.3.5	AISI 309	1250	900	CH_4 Oxyfuel	1239.1
B3.1	AISI 309	1200	900	H_2 Oxyfuel	1415.3
B3.2	AISI 309	1225	900	H_2 Oxyfuel	1328.2
B3.3	AISI 309	1250	900	H_2 Oxyfuel	1290.0
B3.3.5	AISI 309	1250	900	H_2 Oxyfuel	1398.3
C1.1	AISI 441	950	900	CH_4 Air	1391.3
C1.2	AISI 441	1000	900	CH_4 Air	1388.6
C1.3	AISI 441	1050	900	CH_4 Air	1277.8
C1.3.5	AISI 441	1050	900	CH_4 Air	1280.4
C2.1	AISI 441	950	900	CH_4 Oxyfuel	1255.5
C2.2	AISI 441	1000	900	CH_4 Oxyfuel	1280.0
C2.3	AISI 441	1050	900	CH_4 Oxyfuel	1335.3

C2.3.5	AISI 441	1050	900	CH_4 Oxyfuel	1293.7
C3.1	AISI 441	950	900	H_2 Oxyfuel	1205.5
C3.2	AISI 441	1000	900	H_2 Oxyfuel	1276.7
C3.3	AISI 441	1050	900	H_2 Oxyfuel	1325.1
C3.3.5	AISI 441	1050	900	H2 Oxyfuel	1440.2
D1	AISI 304	1250	60	CH_4 Air	
D2	AISI 304	1250	300	CH_4 Air	
D3	AISI 304	1250	600	CH_4 Air	
E1	AISI 304	1250	900	CH_4 Oxyfuel	1397.5
E2	AISI 304	1250	900	H_2 Oxyfuel	1378.3
E4	AISI 304	1250	900	H_2 Oxyfuel	1386.1
F1	AISI 309	1250	900	CH_4 Air	1401.5
F2	AISI 309	1250	900	H_2 Oxyfuel	1412.1
F3	AISI 309	1250	900	CH_4 Air	1372.1
F4	AISI 309	1250	900	H_2 Oxyfuel	1394.6
F5	AISI 309	1250	900	CH_4 Air	1377.0
F6	AISI 309	1250	900	H_2 Oxyfuel	1213.5
F7	AISI 309	1200	900	CH_4 Air	1413.8
F8	AISI 309	1200	900	H_2 Oxyfuel	1323.5
F9	AISI 309	1225	900	CH_4 Air	1372.9
F10	AISI 309	1225	900	H_2 Oxyfuel	1221.4

5.3 FESEM inspection

After the experiments were finished, the samples were removed instantly and placed inside an insulated vessel for even cooling in room temperature. After the samples had cooled down, they were weighed once more. Selected samples were epoxied, cross sectioned and polished for FESEM (Field Emission Scanning Electron Microscope) inspection. The surfaces of polished samples were coated with a thin layer of graphite to improve electric conductivity, thus aiding the FESEM inspection.

The samples were inspected with a FESEM located at the Centre For Material Analysis at the University of Oulu. The FESEM used was a Zeiss ULTRA plus FESEM equipped with Energy-Dispersive X-ray Spectroscopy (EDS) and an Electro Backscatter Diffraction camera (EBSD). This microscope is capable of a resolution of 1 nm with a 15 kV electron acceleration voltage, and the EDS is capable of detecting elements from uranium to carbon.

6. RESEARCH RESULTS

This chapter addresses the results of the TGA-experiments and the FESEM-analysis. The results of the TGA-experiments are presented as graphs comparing the scale growth in area normalized mass increase as a function of time. Both the effect of temperature in each atmosphere as well as the atmosphere in each temperature are presented. The one-, five- and 10-minute experiment results regarding the effect of annealing time on AISI 304 in CH_4 Air atmospheres and are also presented. The graphs show the growth of scale per surface area in grams per square millimetre (g/mm^2) on the y-axis and time in seconds on the x-axis. The total time for the atmospheric and temperature experiments were 15 minutes, and for the stopping experiments one, five, ten and 15 minutes.

6.1 AISI 304

The effects of annealing temperature and atmosphere on the scale growth on AISI 304 stainless steel are presented in **Figures 6 – 12.** The effects of temperature and atmosphere are presented separately, and the total mass gain (scale formation) per surface area for each experiment are presented in **Table 3.** at the end of this chapter.

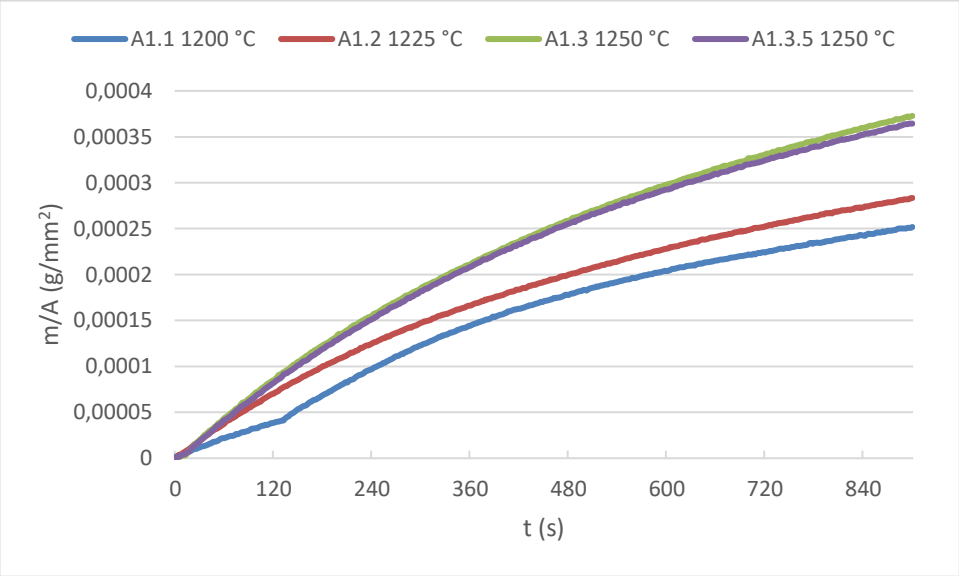

Figure 6. The effect of temperature on scale growth in the CH_4 Air atmosphere on AISI 304. A1.3.5 is a repeated experiment.

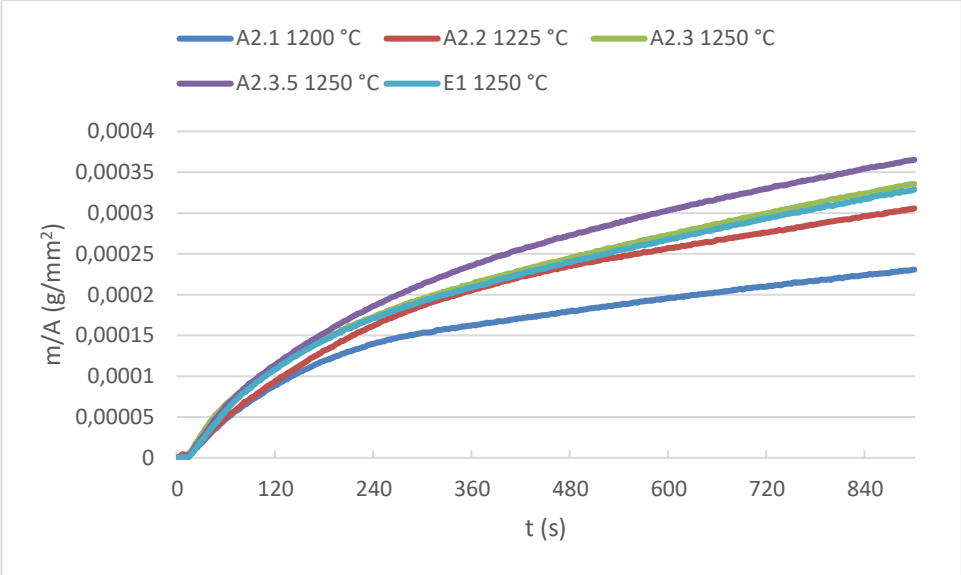

Figure 7. The effect of temperature on scale growth in the CH_4 Oxyfuel atmosphere on AISI 304. A2.3.5 and E1 are repeated experiments.

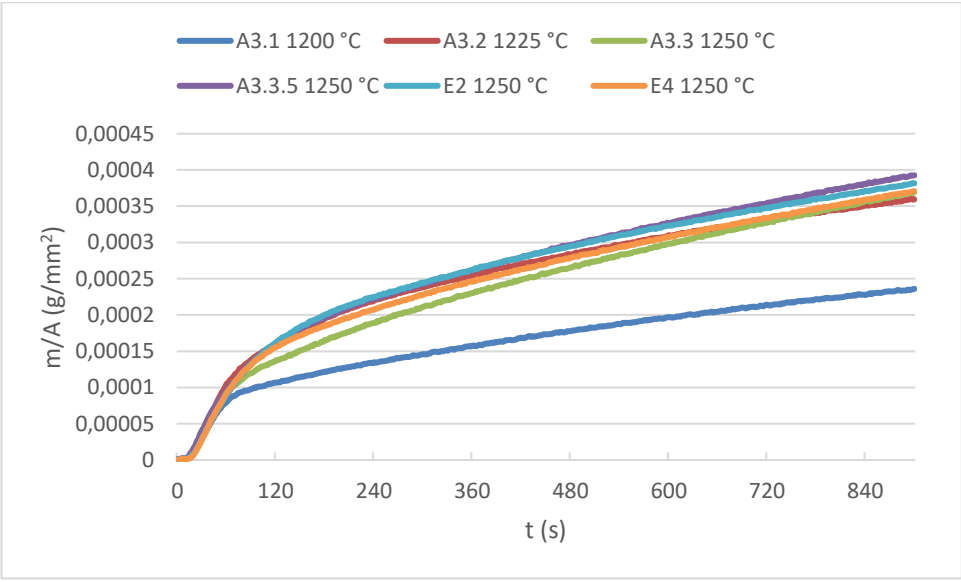

Figure 8. The effect of temperature on scale growth in the H_2 Oxyfuel atmosphere on AISI 304. A3.3.5, E2 and E4 are repeated experiments.

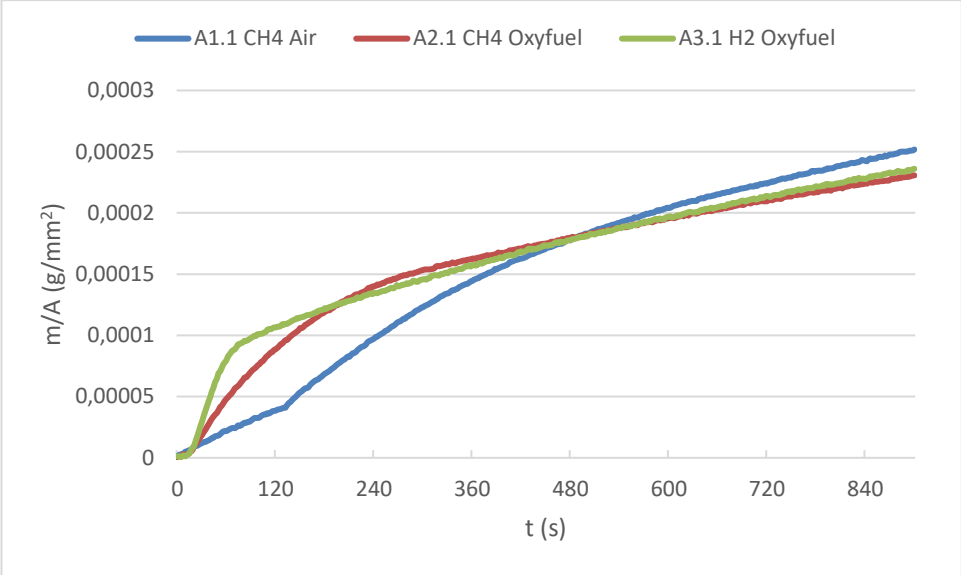

Figure 9. The effect of atmosphere on scale growth at 1200 °C on AISI 304.

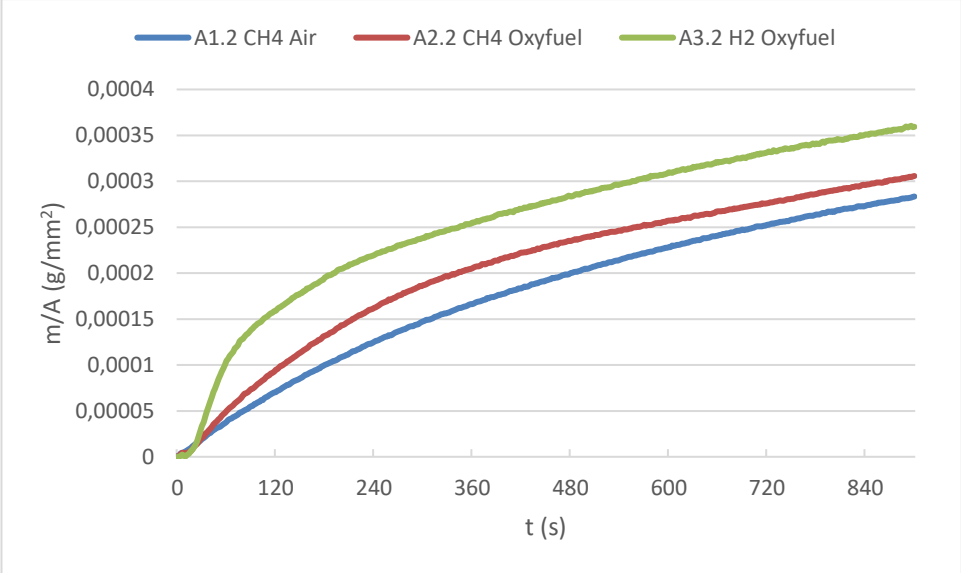

Figure 10. The effect of atmosphere on scale growth at 1225 °C on AISI 304.

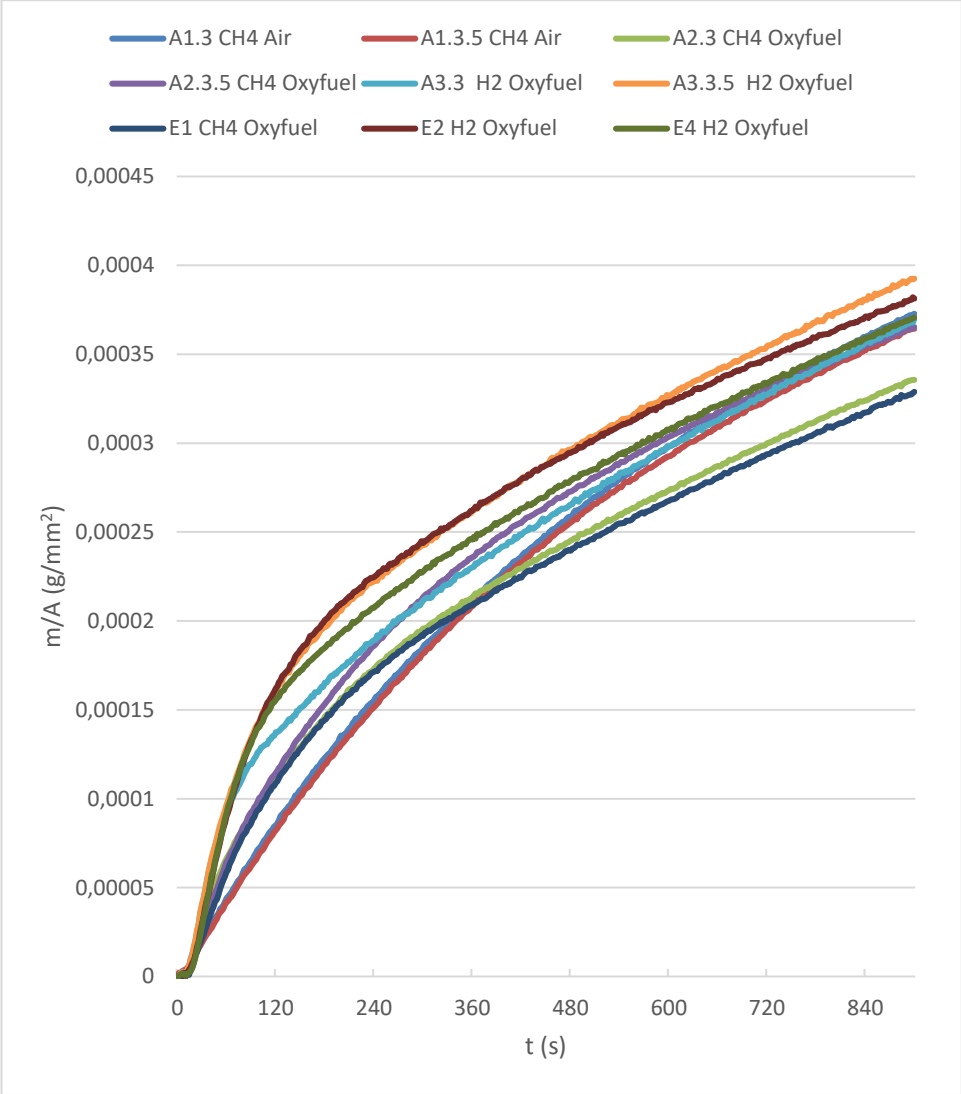

Figure 11. The effect of atmosphere on scale growth at 1250 °C on AISI 304. A1.3.5, A2.3.5, A3.3.5, E1, E2 and E4 are repeated experiments.

For clarity, most of the lines from **Figure 11.** are trimmed, leaving one for each atmosphere. The results are presented in **Figure 12.**

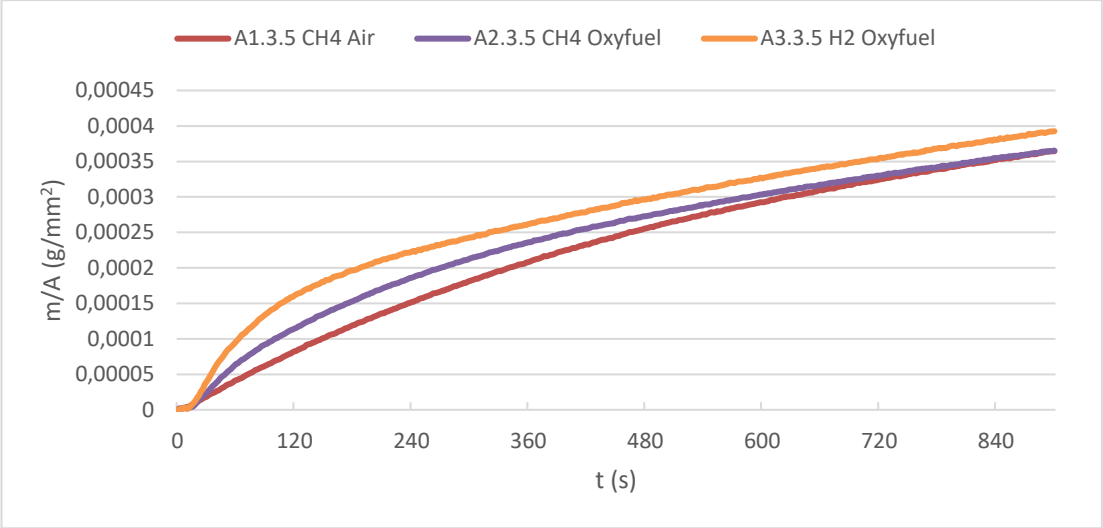

Figure 12. The effect of atmosphere on scale growth at 1225 °C, three experiments, on AISI 304. All three experiments are repeated experiments.

The final oxide mass per surface area at the end of the experiments for every AISI 304 experiment is depicted in **Table 3.** The results are organized first by atmospheres, then by temperatures.

Table 3. The final oxide mass per surface area for AISI 304 experiments.

ID	Steel Grade	Temperature (°C)	Time (s)	Atmosphere	Scale growth (g/mm²)
A1.1	AISI 304	1200	900	CH_4 Air	2.52E-04
A1.2	AISI 304	1225	900	CH_4 Air	2.83E-04
A1.3	AISI 304	1250	900	CH_4 Air	3.73E-04
A1.3.5	AISI 304	1250	900	CH_4 Air	3.64E-04
A2.1	AISI 304	1200	900	CH_4 Oxyfuel	2.31E-04
A2.2	AISI 304	1225	900	CH_4 Oxyfuel	3.06E-04
A2.3	AISI 304	1250	900	CH_4 Oxyfuel	3.36E-04
A2.3.5	AISI 304	1250	900	CH_4 Oxyfuel	3.65E-04
E1	AISI 304	1250	900	CH_4 Oxyfuel	3.29E-04
A3.1	AISI 304	1200	900	H_2 Oxyfuel	2.36E-04
A3.2	AISI 304	1225	900	H_2 Oxyfuel	3.59E-04
A3.3	AISI 304	1250	900	H_2 Oxyfuel	3.70E-04
A3.3.5	AISI 304	1250	900	H_2 Oxyfuel	3.93E-04
E2	AISI 304	1250	900	H_2 Oxyfuel	3.81E-04
E4	AISI 304	1250	900	H_2 Oxyfuel	3.71E-04

6.2 AISI 309

The effects of annealing temperature and atmosphere on the scale growth on AISI 309 stainless steel are presented in **Figures 13 – 23.** The effects of temperature and atmosphere are presented separately, and the total mass gain (scale formation) per surface area for each experiment are presented in **Table 4.** at the end of this chapter.

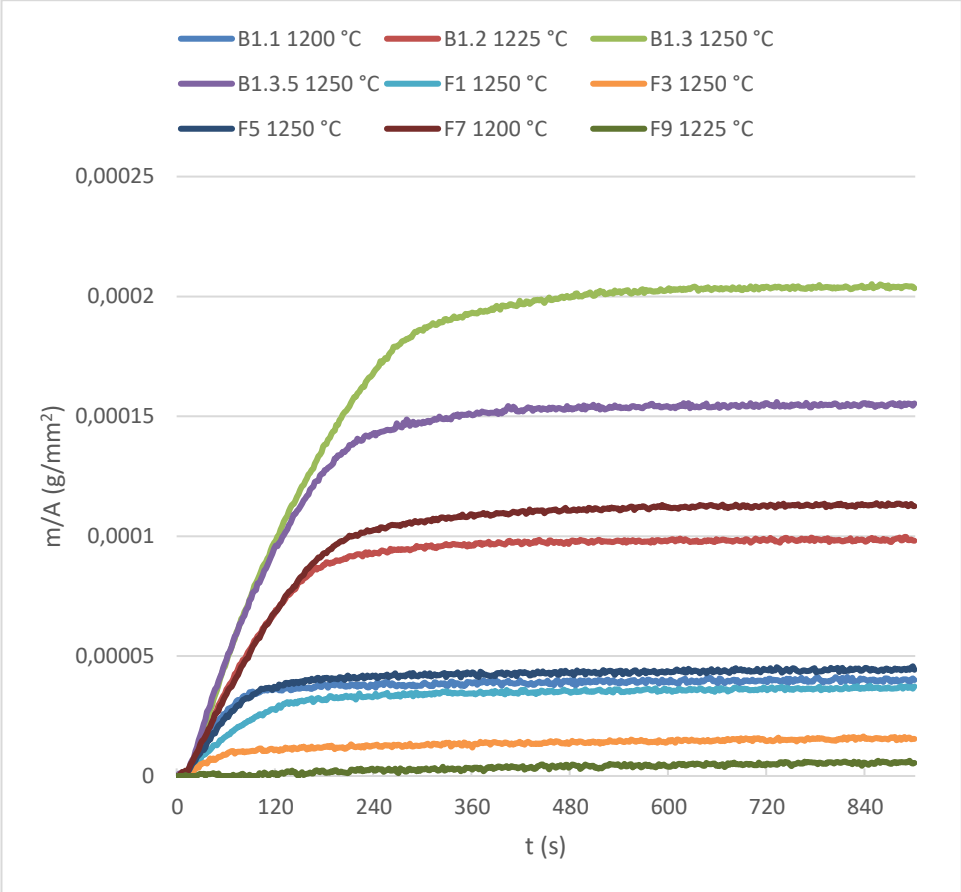

Figure 13. The effect of temperature on scale growth in the CH_4 Air atmosphere on AISI 309. B1.3.5 and experiments labeled Fx are all repeated experiment.

Again, all but the four initial experiments are trimmed for clarity. The results are presented in **Figure 14.**

For clarity and comparison, the experiment results are split into two. The initial experiments labeled Bx are presented in **Figure 14.**, and later experiments labeled Fx are presented in **Figure 15.**

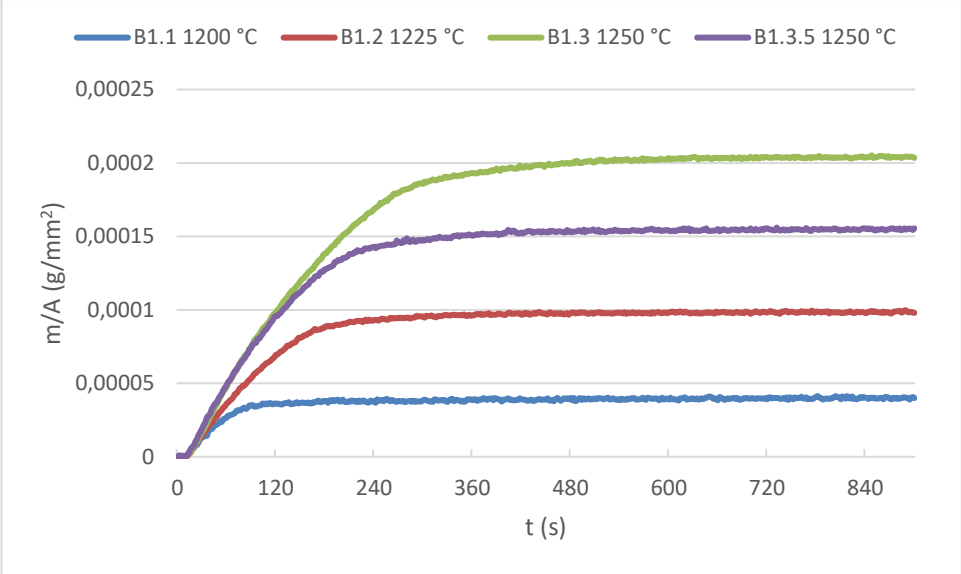

Figure 14. The effect of temperature on scale growth in the CH_4 Air atmosphere on AISI 309. Initial experiments, B1.3.5 is a repeated experiment.

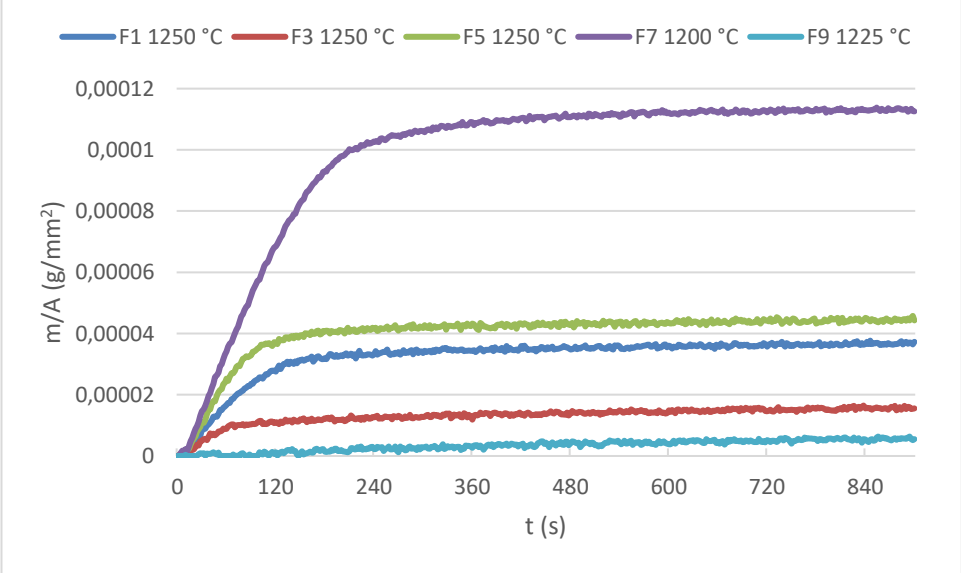

Figure 15. The effect of temperature on scale growth in the CH_4 Air atmosphere on AISI 309. Repeated experiments performed after initial experiments.

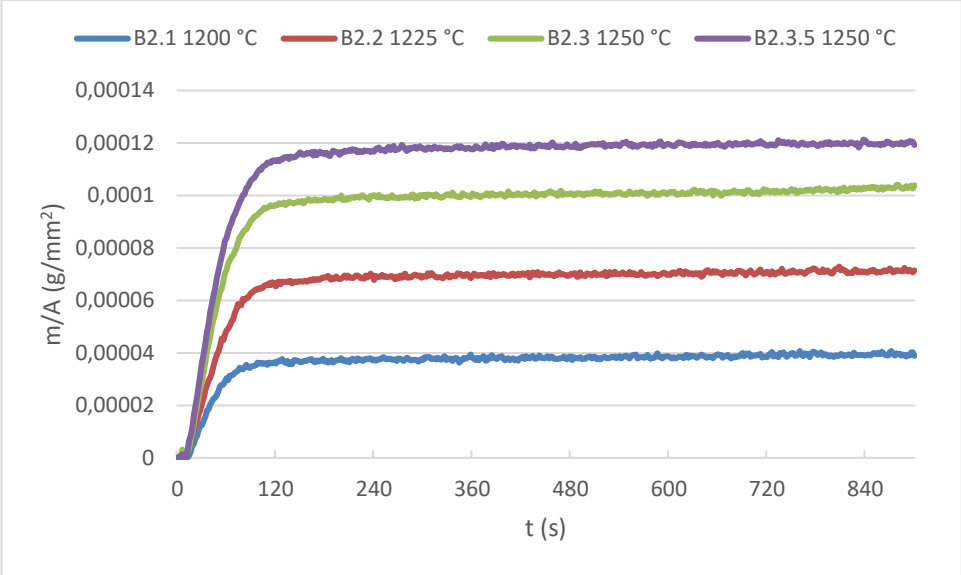

Figure 16. The effect of temperature on scale growth in the CH_4 Oxyfuel atmosphere on AISI 309. B2.3.5 is a repeated experiment.

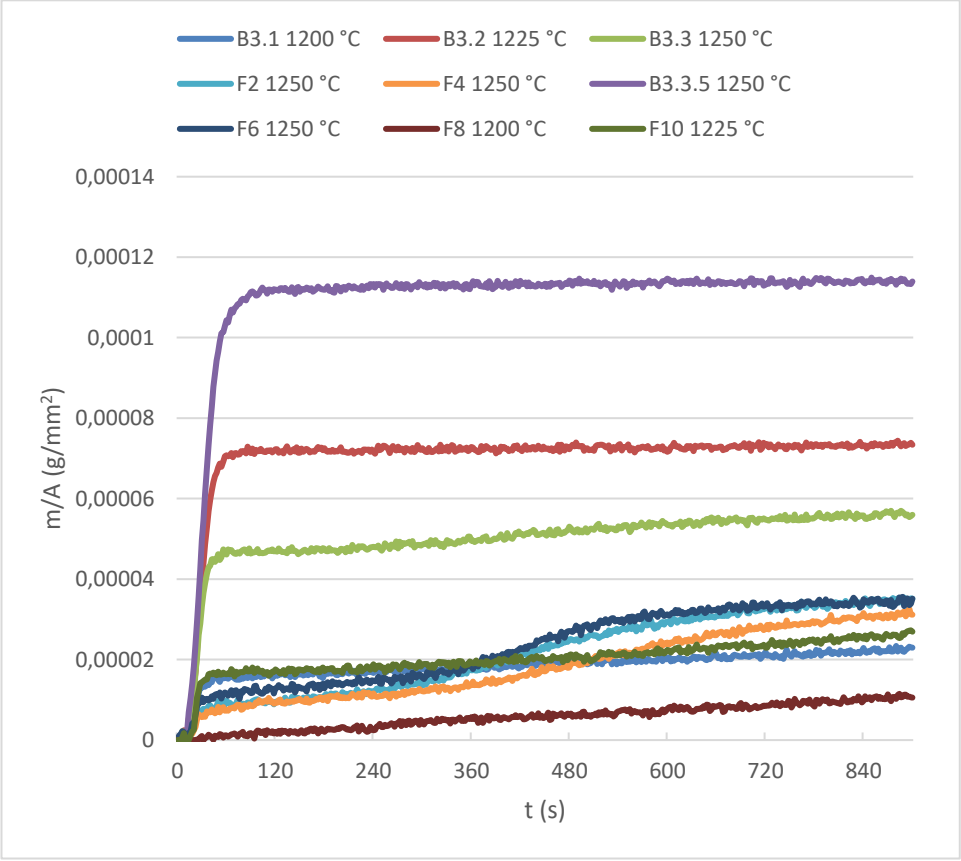

Figure 17. The effect of temperature on scale growth in the H_2 Oxyfuel atmosphere on AISI 309.

Once again, due to poor repeatability and high number of experiments, the experiments are split into initial and later experiments. The results are presented in **Figures 18.** and **19.**

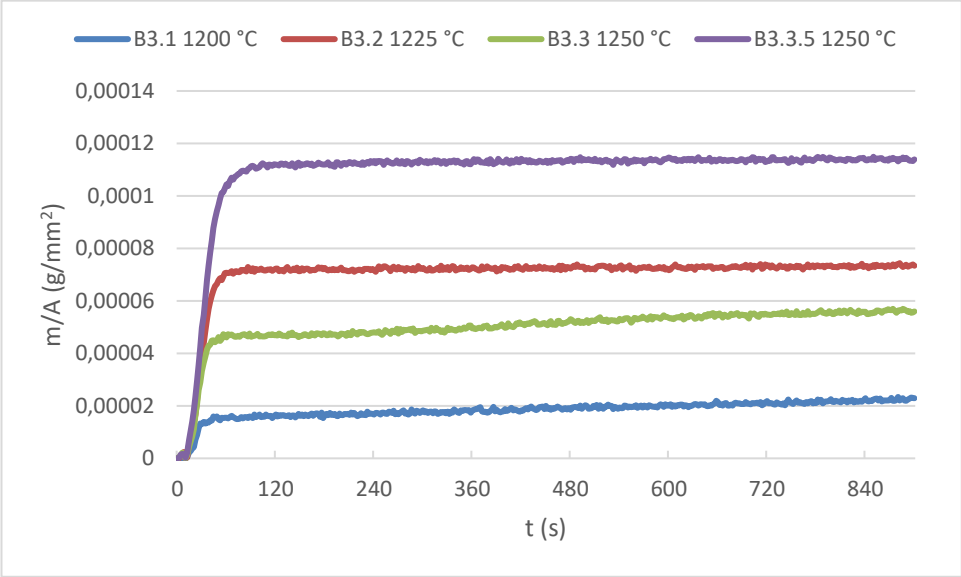

Figure 18. The effect of temperature on scale growth in the H_2 Oxyfuel atmosphere on AISI 309. The initial experiments.

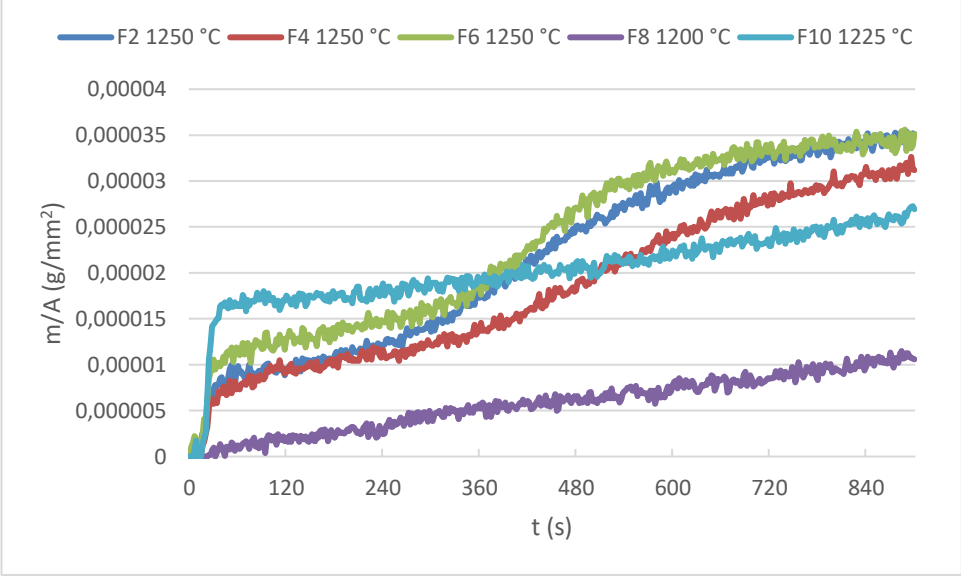

Figure 19. The effect of temperature on scale growth in the H_2 Oxyfuel atmosphere on AISI 309. The later repeated experiments.

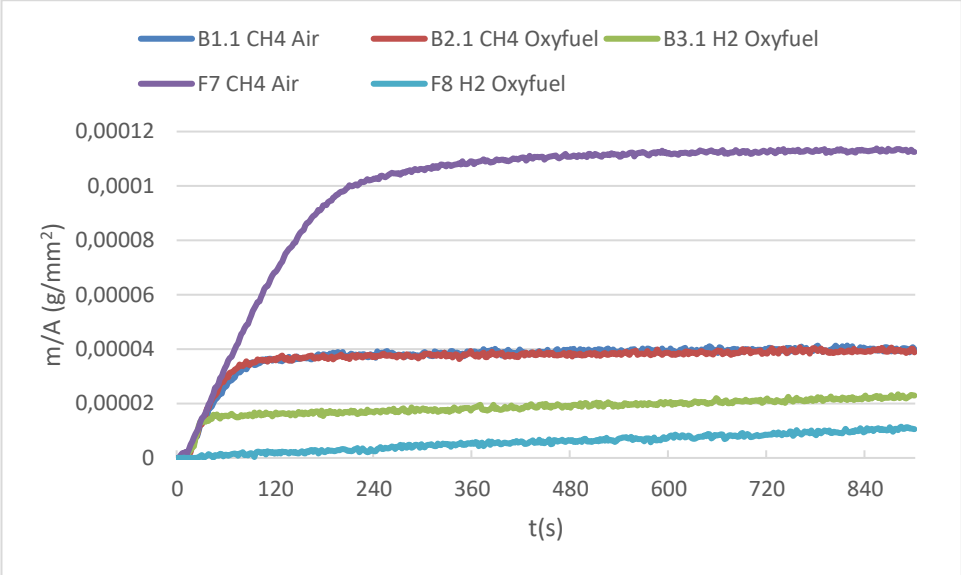

Figure 20. The effect of atmosphere on scale growth at 1200 °C on AISI 309. F7 and F8 are repeated experiments.

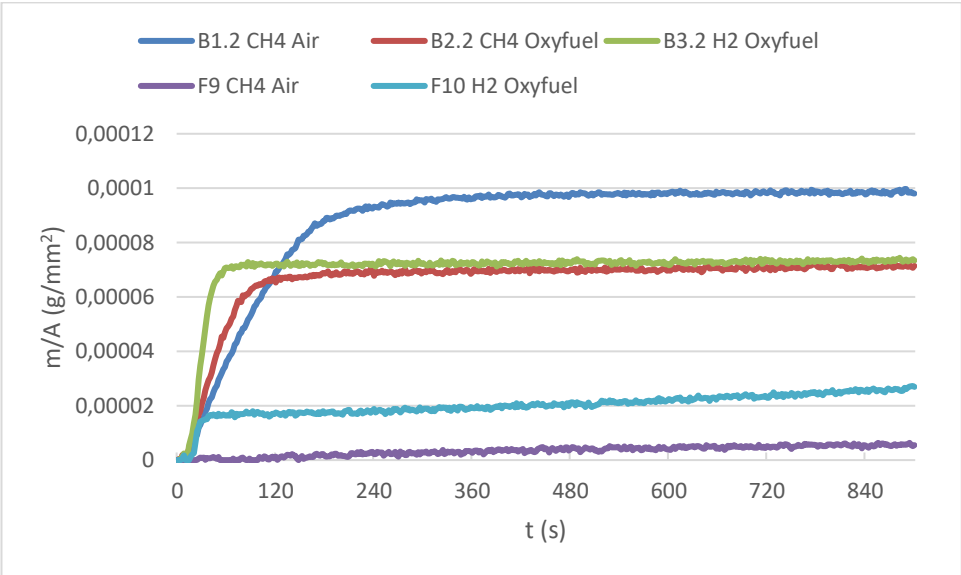

Figure 21. The effect of atmosphere on scale growth at 1225 °C on AISI 309. F9 and F10 are repeated experiments.

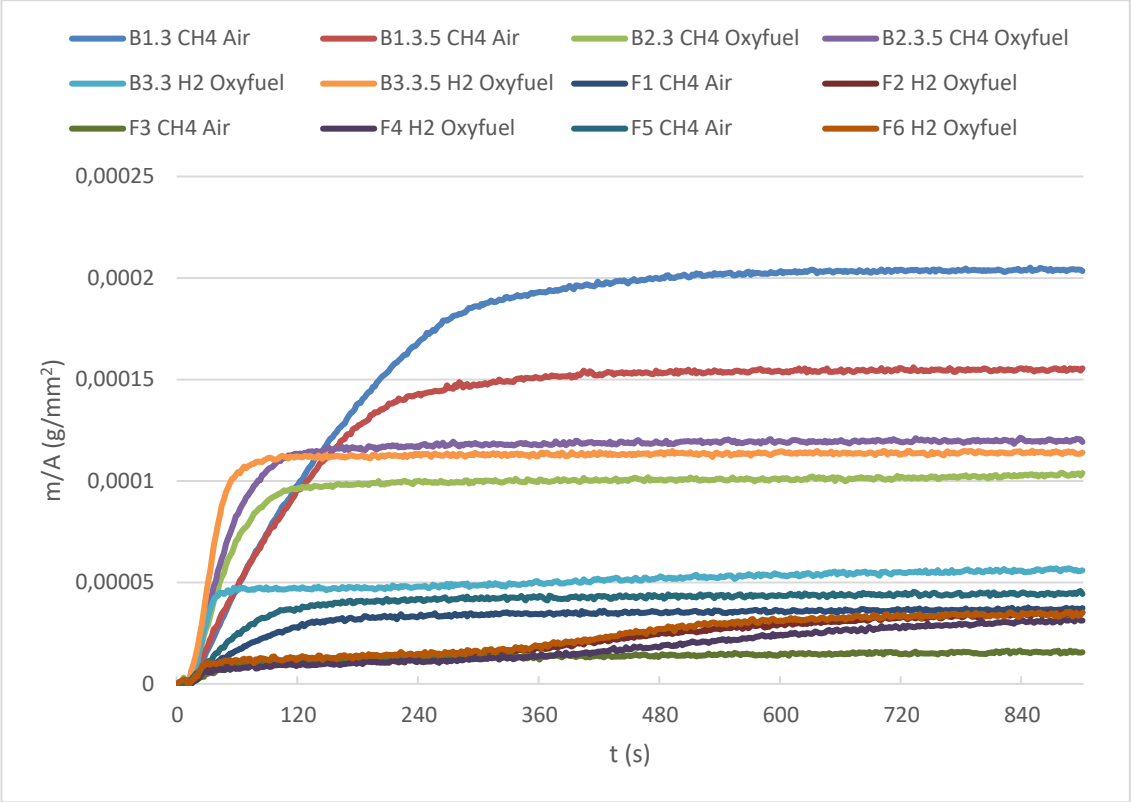

Figure 22. The effect of atmosphere on scale growth at 1250 °C on AISI 309.

Once again, all but three experiments were trimmed for clarity, and the results are presented in **Figure 23.**

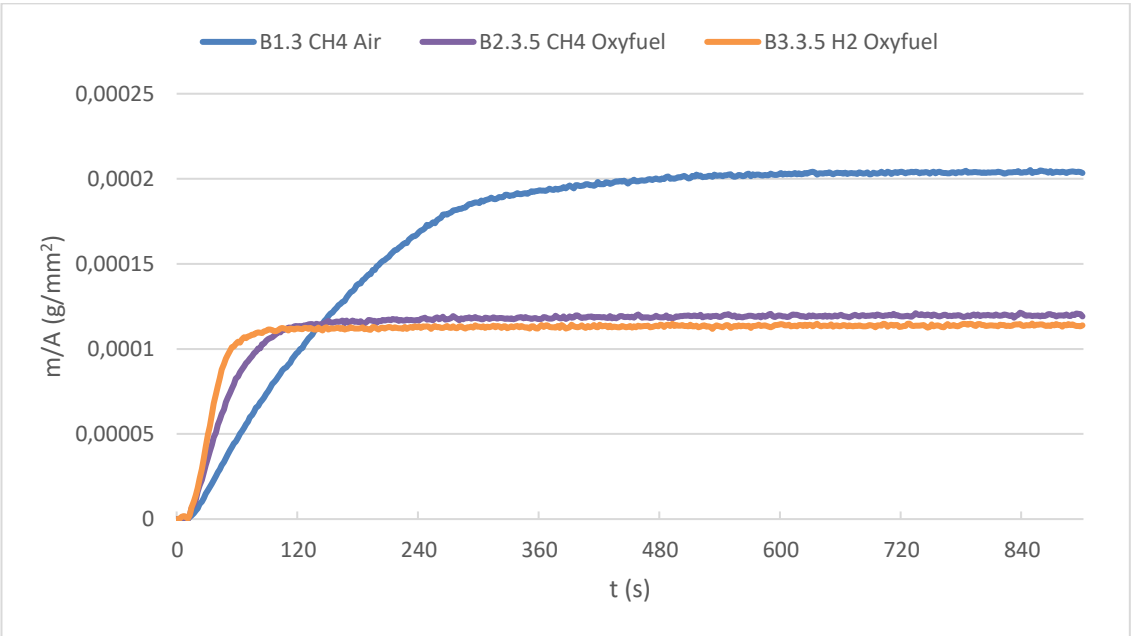

Figure 23. The effect of atmosphere on scale growth at 1250 °C on AISI 309. Three experiments, B2.3.5 and B3.3.5 are repeated experiments.

The final oxide mass per surface area at the end of the experiments for every AISI 309 experiment is depicted in **Table 4.** The results are organized first by atmospheres, then by temperatures.

Table 4. The final oxide mass per surface area for AISI 309 experiments.

ID	Steel Grade	Temperature (°C)	Time (s)	Atmosphere	Scale growth (g/mm^2)
B1.1	AISI 309	1200	900	CH_4 Air	4.00E-05
F7	AISI 309	1200	900	CH_4 Air	1.13E-04
B1.2	AISI 309	1225	900	CH_4 Air	9.81E-05
F9	AISI 309	1225	900	CH_4 Air	5.46E-06
B1.3	AISI 309	1250	900	CH_4 Air	2.03E-04
B1.3.5	AISI 309	1250	900	CH_4 Air	1.55E-04
F1	AISI 309	1250	900	CH_4 Air	3.73E-05
F3	AISI 309	1250	900	CH_4 Air	1.55E-05
F5	AISI 309	1250	900	CH_4 Air	4.43E-05
B2.1	AISI 309	1200	900	CH_4 Oxyfuel	3.89E-05
B2.2	AISI 309	1225	900	CH_4 Oxyfuel	7.14E-05
B2.3	AISI 309	1250	900	CH_4 Oxyfuel	1.04E-04
B2.3.5	AISI 309	1250	900	CH_4 Oxyfuel	1.19E-04
B3.1	AISI 309	1200	900	H_2 Oxyfuel	2.30E-05
F8	AISI 309	1200	900	H_2 Oxyfuel	1.06E-05
B3.2	AISI 309	1225	900	H_2 Oxyfuel	7.34E-05
F10	AISI 309	1225	900	H_2 Oxyfuel	2.69E-05
B3.3	AISI 309	1250	900	H_2 Oxyfuel	5.60E-05
B3.3.5	AISI 309	1250	900	H_2 Oxyfuel	1.14E-04
F2	AISI 309	1250	900	H_2 Oxyfuel	3.51E-05
F4	AISI 309	1250	900	H_2 Oxyfuel	3.12E-05
F6	AISI 309	1250	900	H_2 Oxyfuel	3.51E-05

6.3 AISI 441

The effects of annealing temperature and atmosphere on the scale growth on AISI 441 stainless steel are presented in **Figures 24 – 29.** The effects of temperature and atmosphere are presented separately, and the total mass gain (scale formation) per surface area for each experiment are presented in **Table 5.** at the end of this chapter. Due to high distortion in the measurement data of the experiments conducted in the CH_4 Air atmosphere, all AISI 441 results are presented as the average of 50 measurement points (100 seconds). For coherence, this is done on the two other atmospheres also. In addition, the graphs for the CH_4 Oxyfuel and H_2 Oxyfuel were practically identical regardless of the usage of original measurement points or the average of every 50 measurements points.

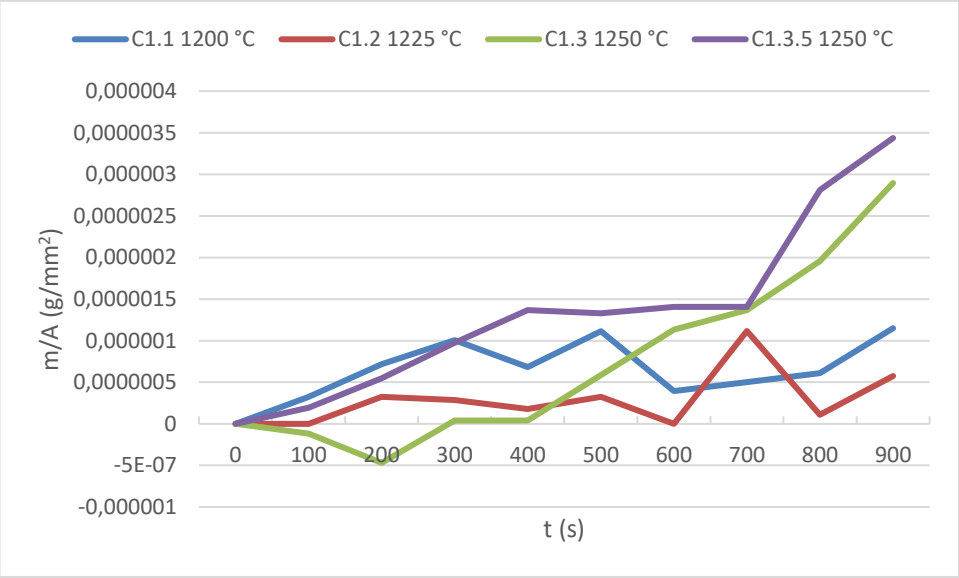

Figure 24. The effect of temperature on scale growth in the CH_4 Air atmosphere on AISI 441 using the average of every 50 measurement points. C1.3.5 is a repeated experiment.

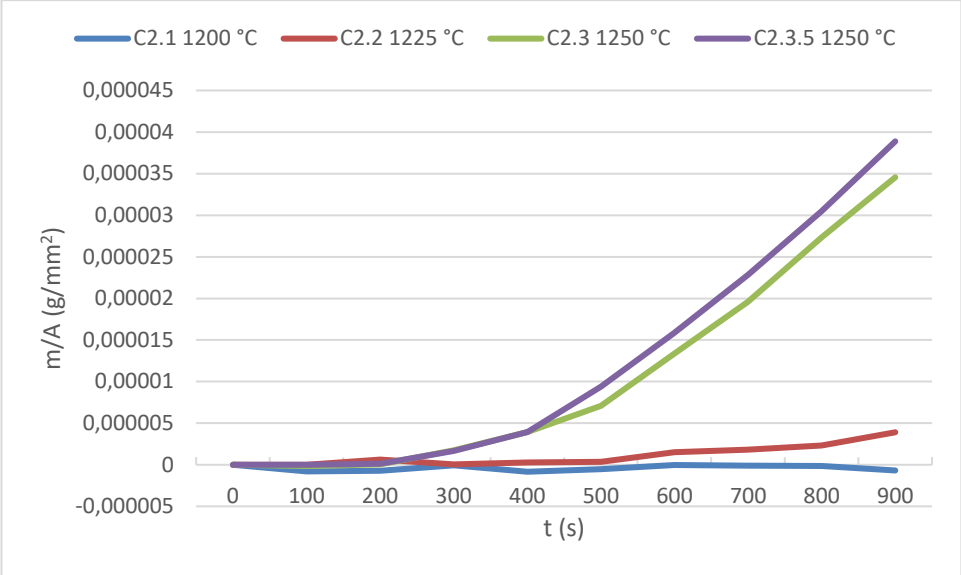

Figure 25. The effect of temperature on scale growth in the CH_4 Oxyfuel atmosphere on AISI 441 using the average of every 50 measurement points. C2.3.5 is a repeated experiment.

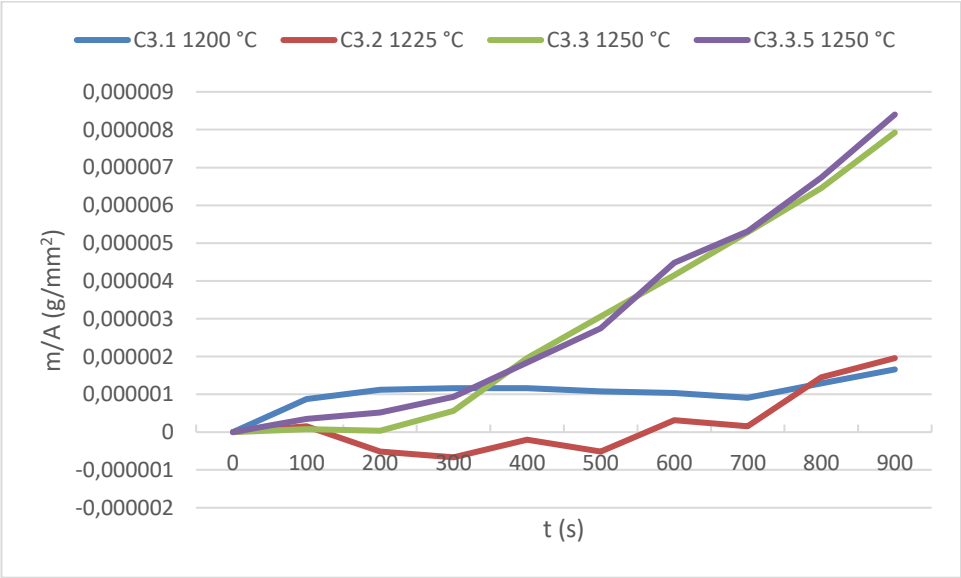

Figure 26. The effect of temperature on scale growth in the H_2 Oxyfuel atmosphere on AISI 441 using the average of every 50 measurement points. C3.3.5 is a repeated experiment.

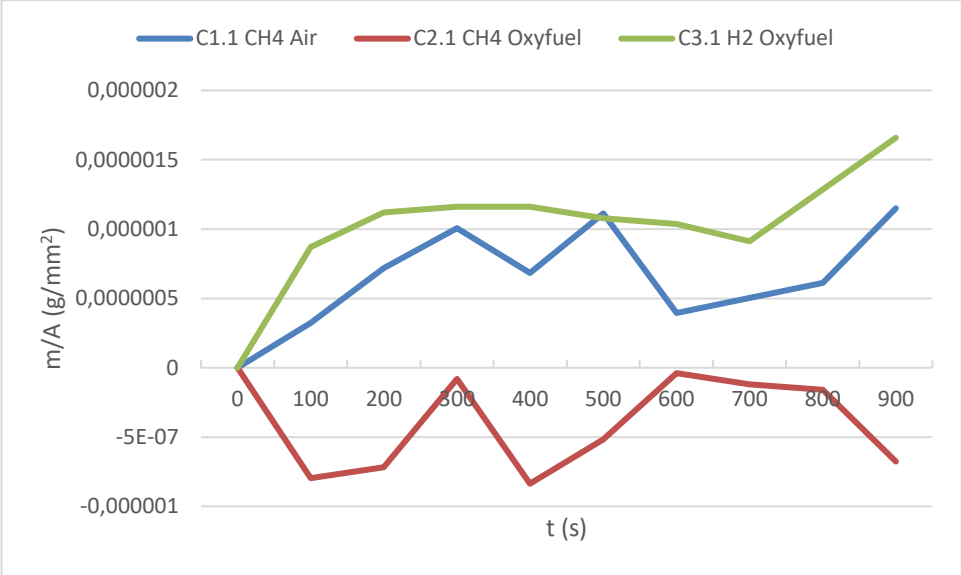

Figure 27. The effect of atmosphere on scale growth at 950 °C on AISI 441 using the average of every 50 measurement points.

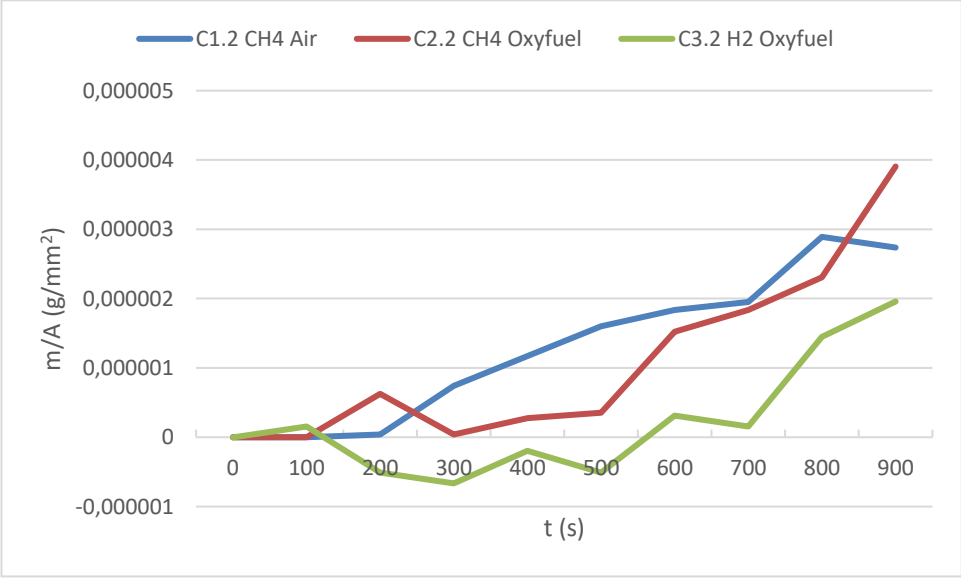

Figure 28. The effect of atmosphere on scale growth at 1000 °C on AISI 441 using the average of every 50 measurement points.

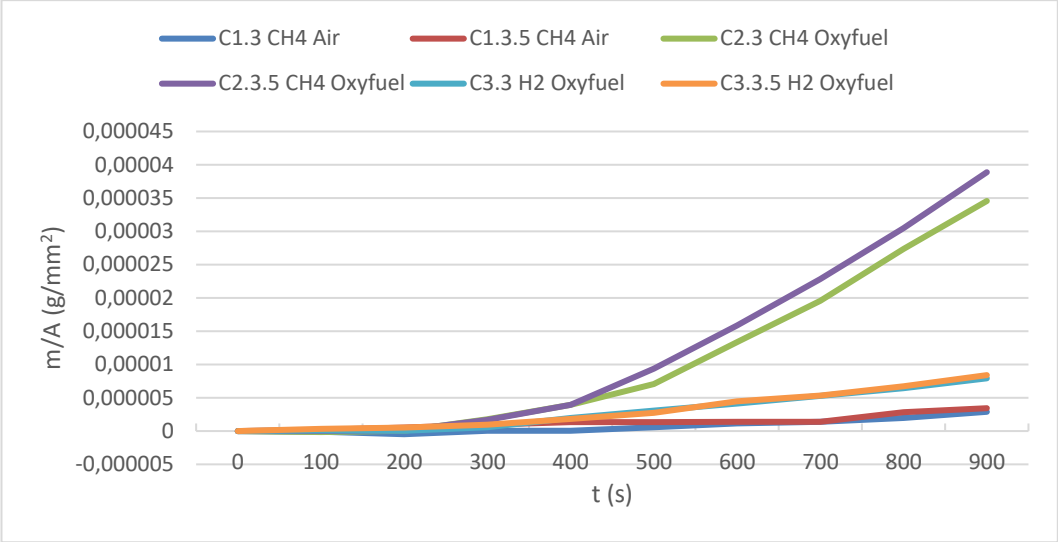

Figure 29. The effect of atmosphere on scale growth at 1050 °C on AISI 441 using the average of every 50 measurement points. C1.3.5, C2.3.5 and C3.3.5 are repeated experiments.

The final oxide mass per surface area at the end of the experiments for every AISI 441 experiment is depicted in **Table 5.** The results are organized first by atmospheres, then by temperatures.

Table 5. The final oxide mass per surface area for AISI 441 experiments.

ID	Steel Grade	Temperature (°C)	Time (s)	Atmosphere	Scale growth (g/mm²)
C1.1	AISI 441	950	900	CH_4 Air	1.37E-06
C1.2	AISI 441	1000	900	CH_4 Air	1.15E-06
C1.3	AISI 441	1050	900	CH_4 Air	3.13E-06
C1.3.5	AISI 441	1050	900	CH_4 Air	3.67E-06
C2.1	AISI 441	950	900	CH_4 Oxyfuel	7.97E-07
C2.2	AISI 441	1000	900	CH_4 Oxyfuel	4.22E-06
C2.3	AISI 441	1050	900	CH_4 Oxyfuel	3.82E-05
C2.3.5	AISI 441	1050	900	CH_4 Oxyfuel	4.27E-05
C3.1	AISI 441	950	900	H_2 Oxyfuel	1.82E-06
C3.2	AISI 441	1000	900	H_2 Oxyfuel	2.27E-06
C3.3	AISI 441	1050	900	H_2 Oxyfuel	8.91E-06
C3.3.5	AISI 441	1050	900	H_2 Oxyfuel	9.37E-06

6.4 FESEM inspection

The difference of CH_4 Air and H_2 Oxyfuel atmospheres as well as the effect of temperature on the scale growth on AISI 304 were studied.

Three variables were of interest when planning the FESEM-inspection: how would the atmosphere, temperature and annealing time affect the scale growth. Two atmospheres, CH_4 Air and H_2 Oxyfuel, were used in order to assess the effects to oxide scale formation when comparing a technology of tomorrow to one in industry scale use today. All three temperatures used in the experiments were also studied, as well as four different annealing times; 1, 5, 10 and 15 minutes. The results are presented and discussed here.

Images were taken from the metal/oxide interface. The top part of each images contains the formed oxide, whereas the bottom part is the non-oxidized metal. The intermediate part is metal that has started to oxidate, but is not completely transformed. The former metal surface can be seen clearly in most images. The temperature rises from the left side of the image to the right as follows: 1200 °C, 1225 °C, 1250 °C.

In addition, the distribution of iron, chromium, oxygen, silicon and nickel were studied.

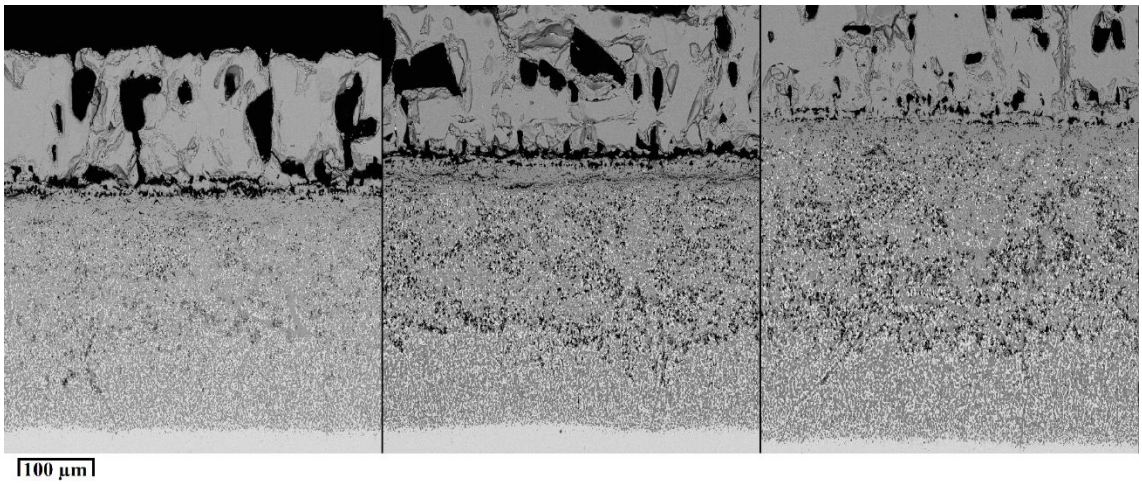

Figure 30. The effect of temperature on scale growth on AISI 304 in CH_4 Air atmosphere, from left to right: 1200 °C, 1225 °C and 1250 °C.

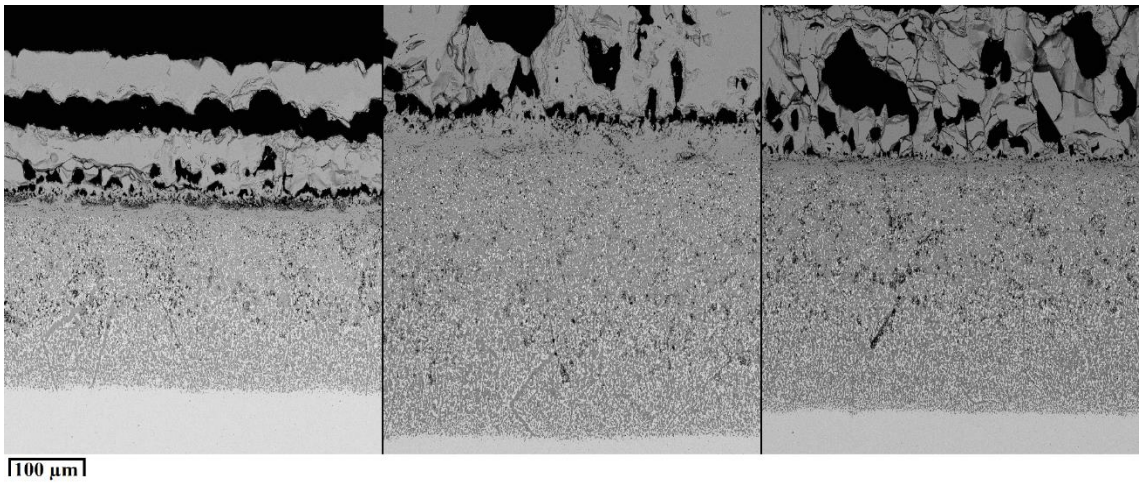

Figure 31. The effect of temperature on scale growth on AISI 304 in H_2 Oxyfuel atmosphere, from left to right: 1200 °C, 1225 °C and 1250 °C.

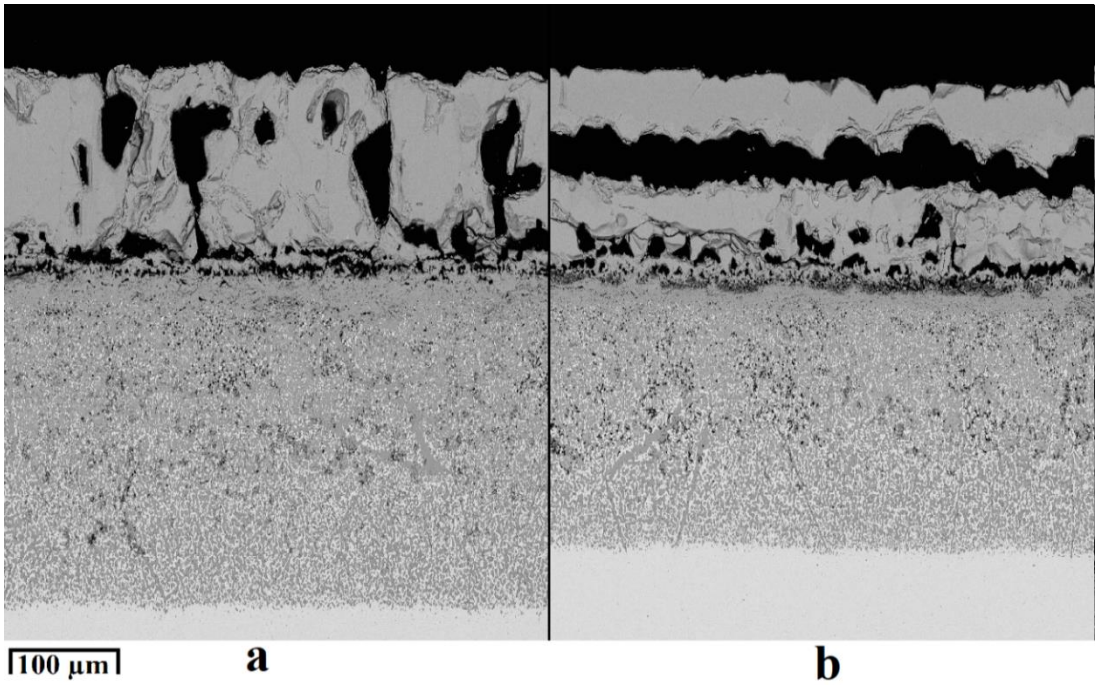

Figure 32. Effect of atmosphere on scale growth on AISI 304 at 1200 °C, atmospheres CH_4 Air (a) and H_2 Oxyfuel (b).

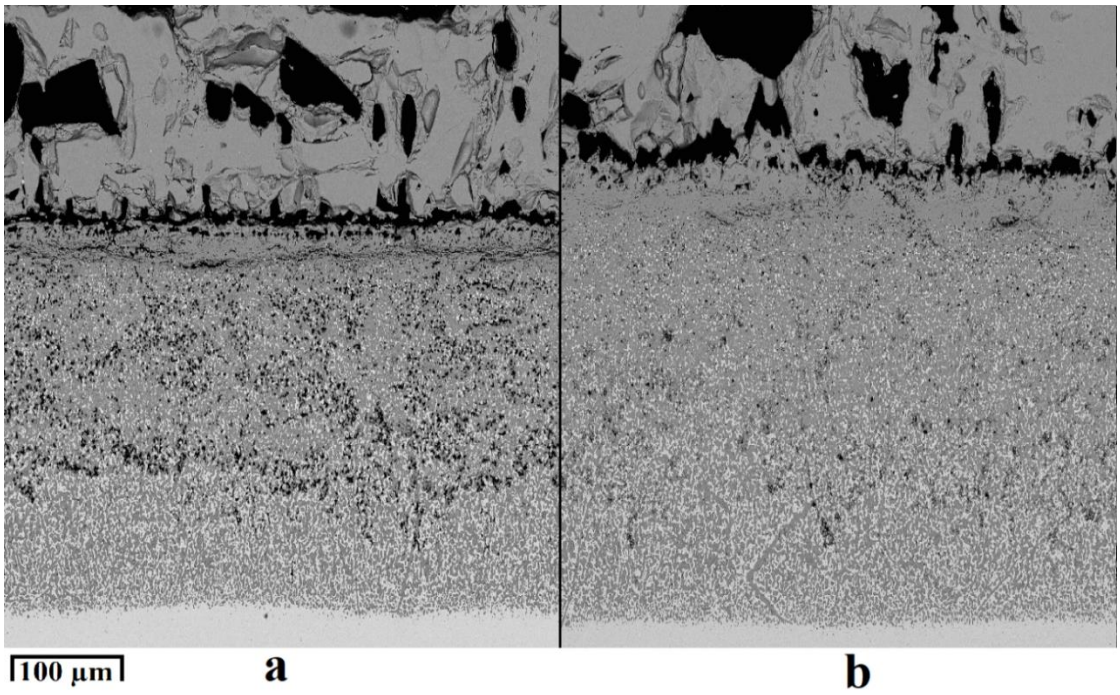

Figure 33. Effect of atmosphere on scale growth on AISI 304 at 1225 °C, atmospheres CH_4 Air (a) and H_2 Oxyfuel (b).

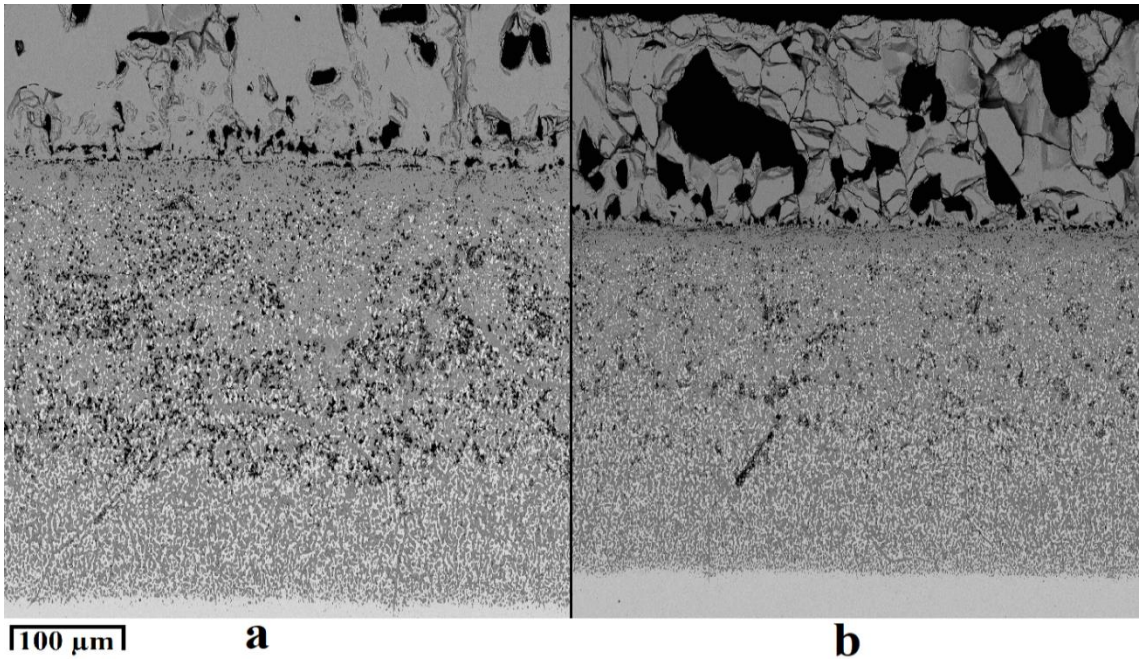

Figure 34. Effect of atmosphere on scale growth on AISI 304 at 1250 °C, atmospheres CH_4 Air (a) and H_2 Oxyfuel (b).

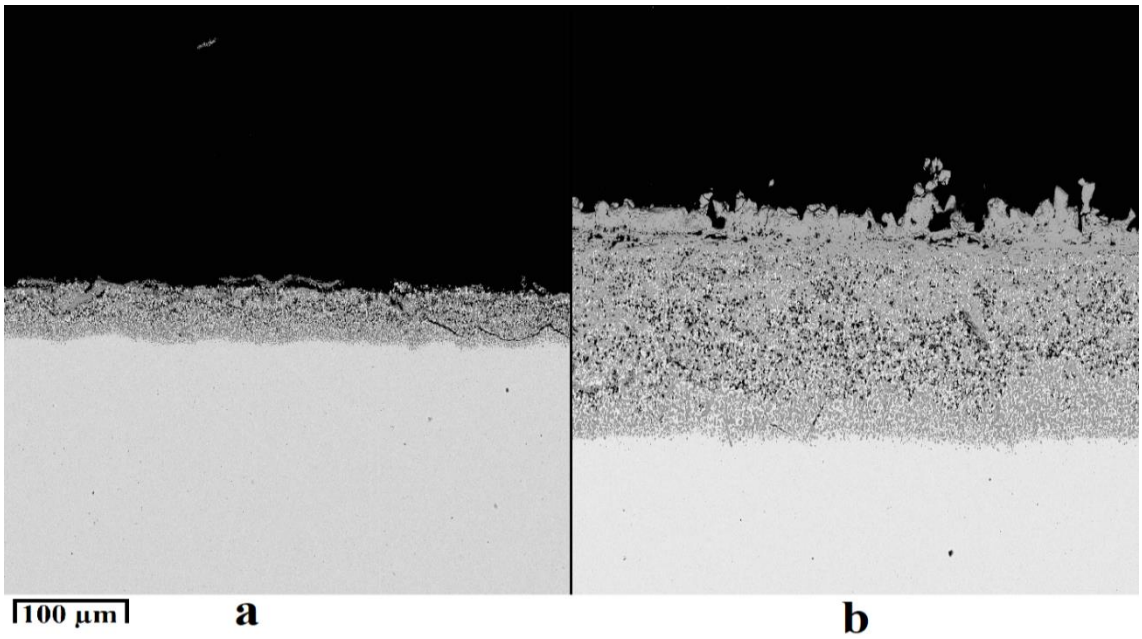

Figure 35. AISI 304 annealed for 1 (a) and 5 (b) minutes in the CH_4 Air atmosphere at 1250 °C.

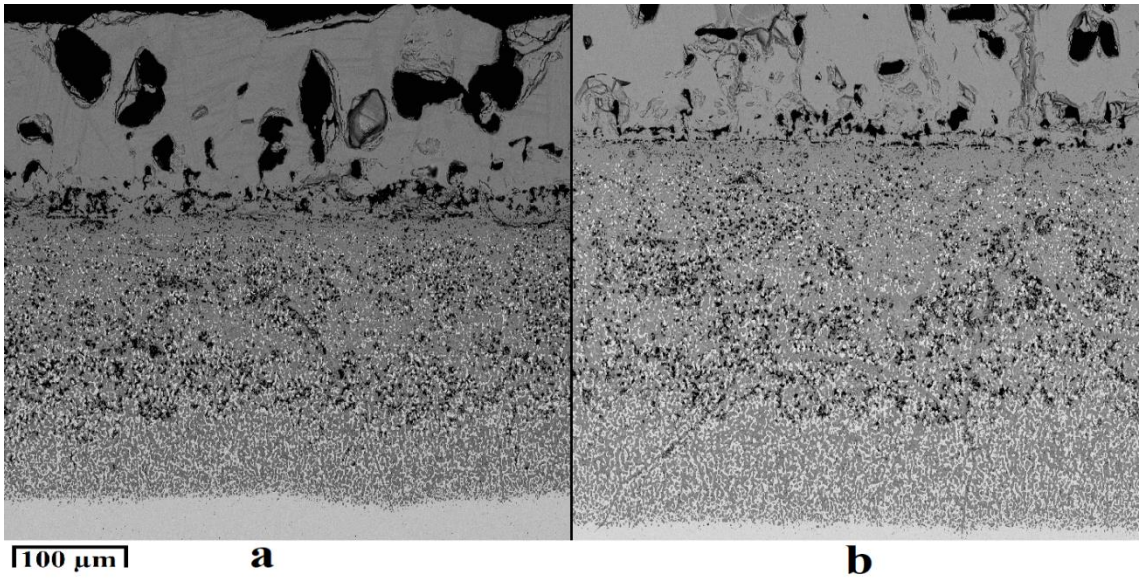

Figure 36. AISI 304 annealed for 10 (a) and 15 (b) minutes in the CH_4 Air atmosphere at 1250 °C.

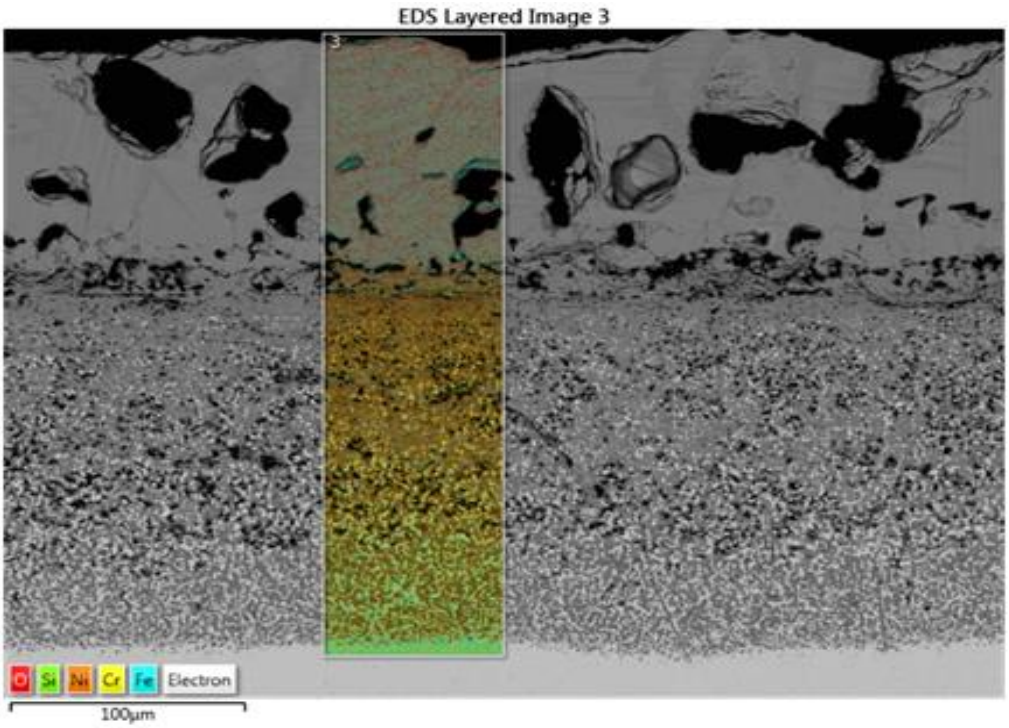

Figure 37. Elemental distribution in sample D3 presented in Figure 38.

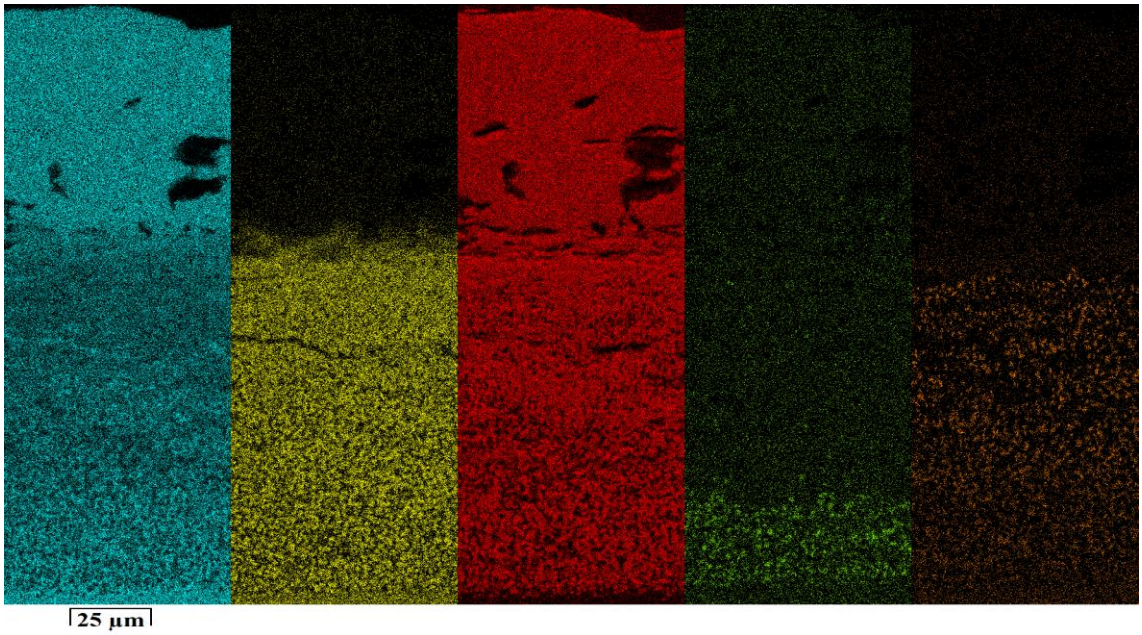

Figure 38. The distribution of elements in AISI 304 annealed at 1250 °C for 10 minutes in the CH_4 Air atmosphere. Elements from left to right: iron, chromium, oxygen, silicon and nickel.

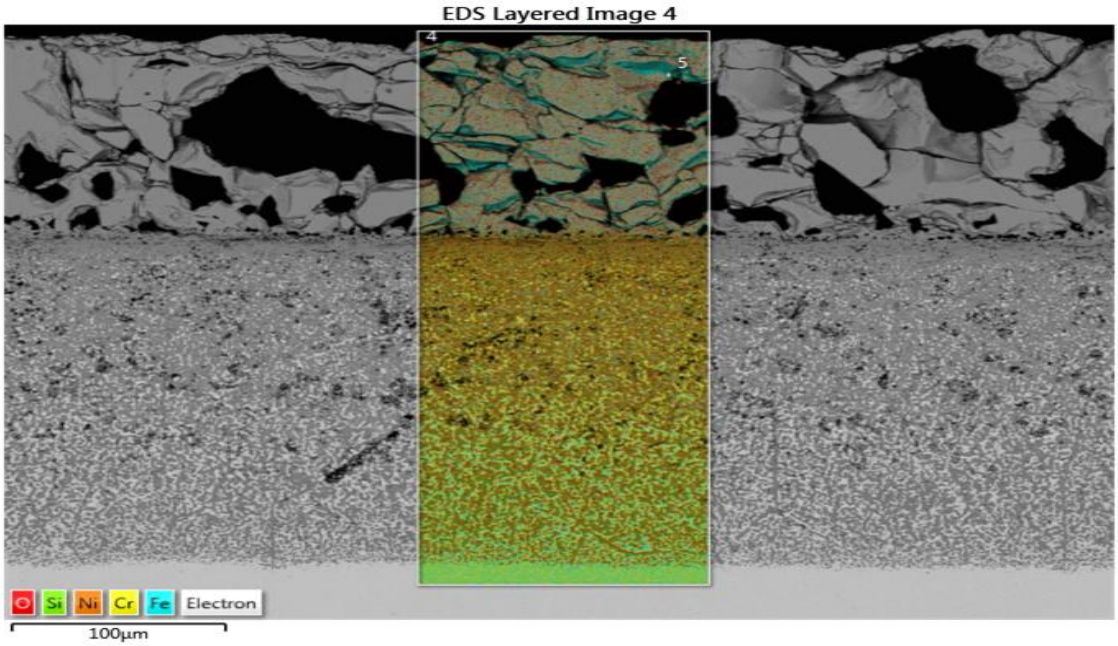

Figure 39. Elemental distribution in sample A3.3 presented in Figure 40.

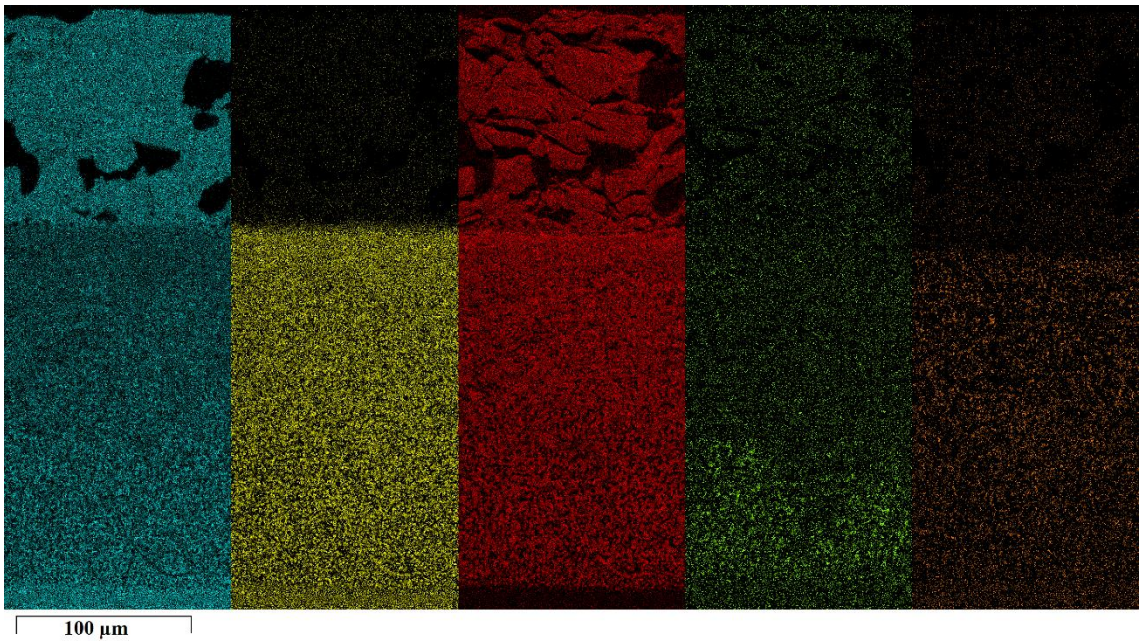

Figure 40. The distribution of elements in AISI 304 annealed at 1250 °C for 15 minutes in the CH_4 Air atmosphere. Elements from left to right: iron, chromium, oxygen, silicon and nickel.

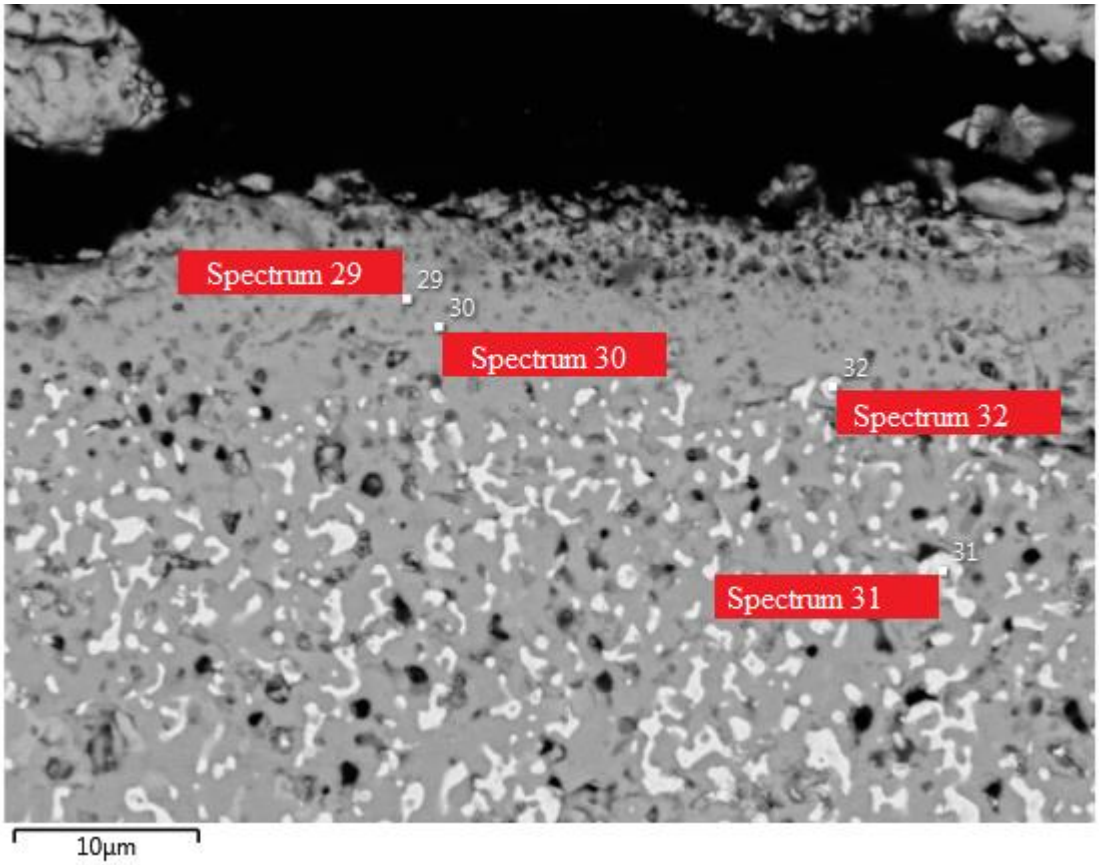

Figure 41. EDS point analysis locations studied in sample A3.1.

Table 6. Chemical compositions of spectrums found in Figure 41, in wt.-%.

Spectrum Label	Spectrum 29	Spectrum 30	Spectrum 31	Spectrum 32
O	24.98	22.63	4.32	10.15
Si	0.46	0.31	0	0
Cr	33.05	24.22	7.58	12.46
Fe	39.09	48.51	43.17	32.94
Ni	1.6	1.69	53.01	57.65
Total	99.18	97.35	108.08	113.19

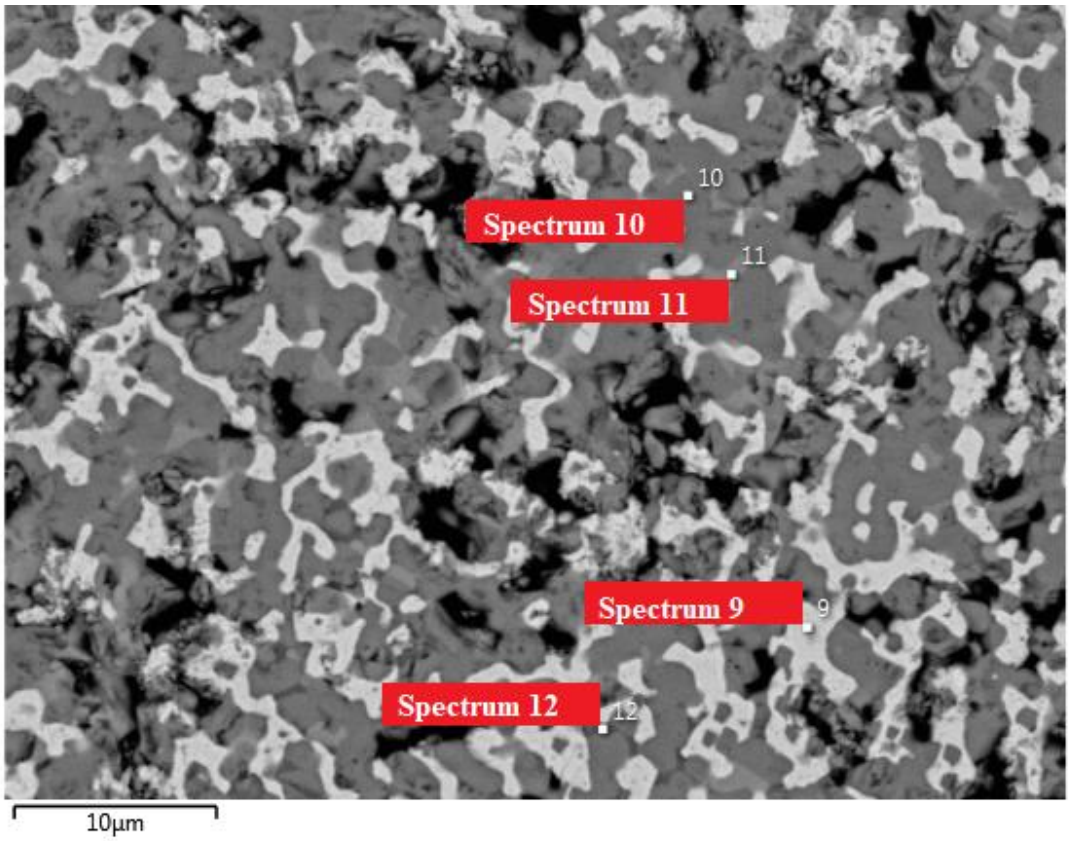

Figure 42. EDS point analysis locations studied in sample D3.

Table 7. Chemical compositions of spectrums found in Figure 42, in wt.-%.

Spectrum Label	Spectrum 9	Spectrum 10	Spectrum 11	Spectrum 12
O	0	23.6	20.66	10.54
Si	0	0.23	0.23	3.48
Cr	5.51	44.79	17.38	5.97
Mn	0	1.85	1.32	1.19
Fe	69.98	29.02	62.87	65.69
Ni	30.68	0	0	19.76
Total	106.17	99.49	102.46	106.64

7. MODELS AND ACTIVATION ENERGIES

The growth in mass per surface area were fitted into models which utilize exponents of the thermogravimetric test results. These models were Parabolic (α^2), Cubic (α^3) and Quadratic (α^4) laws, as well as the exponent 1.7 ($\alpha^{1.7}$), which was iterated using the Solver tool of Microsoft Excel. Some other models, which were initially promising, but were found to work in a less functional manner, were the Anti-Ginstling-Brounstein equation, the Anti-Jander equation and the Avrami-Erofeev equation. Some other models, e.g. Prout-Tomkins equation, Valensi equation and exponential law were deemed to fail early on into the fitting of models.

In order to calculate activation energies and frequency factors, the measured data was raised to the power of the equivalent model, e.g. to the power of two (α^2) with the Parabolic model. Graphs were within each stainless steel grade and atmosphere, containing each annealing temperature and model. The graphs are presented in odd numbered figures between **Figures 43. – 59. and Figure 60.** In order to calculate the activation energies and frequency factors, Arrhenius plots were also drawn for every case described above. The Arrhenius plots are presented in even numbered figures between **Figures 44. – 58.** and **Figure 61.** The calculated activation energies and frequency factors are presented in **Tables 8. – 15.**, and are compiled in **Table 16.** for additional convenience.

It should be noted, that Parabolic and Quadratic Arrhenius plots could not be drawn for AISI 441 annealed in the CH_4 Oxyfuel atmosphere, and the same goes for every model with AISI 441 annealed in the H_2 Oxyfuel Atmosphere. This is due to their slope values being negative. This is probably caused by high interference and/or measurement noise. A result for this could probably be found by increasing the number of experiments in these conditions, but they could not be performed in the time frame allocated for this thesis. If we use similar averages as used with describing the experiment results for AISI 441 (average of every 50 measurement points), Arrhenius plots could be drawn for the Parabolic, Cubic and Quadratic models with AISI 441 annealed in the H_2 Oxyfuel atmosphere. It should also be noted, that this fitting may or may not be applicable for real world model optimization.

After calculating the activation energies and frequency factors, reaction rate constants (k) could be calculated using the Arrhenius equation. The reaction rate constants are presented in **Tables 17. – 19.** The reaction rate constants for AISI 304 in each atmosphere are also presented as graphs in **Figures 62 – 64.** Graphs for AISI 309 and AISI 441 are not presented, for their interpretability was poor at lower temperatures, and in some cases throughout the temperature range.

The reaction rate constants can be utilized in calculating the predicted scale growth. When the experimental results are fitted into models, we can predict scale growth in temperatures which were not used in the experiments. As an example, the calculated reaction rate constants of every model are utilized to predict the scale growth of AISI 304 annealed at 1300 °C in the CH_4 Air atmosphere. The predicted results are presented below in **Figure 65.** The equations used to calculate the predicted scale growth are presented below in Equations (12) for the Parabolic model, (13) for the Cubic model, (14) for the Quadratic model and (15) for the 1.7-model. Time in seconds is depicted as ”t” in every equation.

$$\Delta m = (k_p \cdot t)^{\frac{1}{2}} \tag{12}$$

where k_p is the parabolic reaction rate constant.

$$\Delta m = (k_c \cdot t)^{\frac{1}{3}} \tag{13}$$

where k_c is the cubic reaction rate constant.

$$\Delta m = (k_q \cdot t)^{\frac{1}{4}} \tag{14}$$

where k_q is the quadratic reaction rate constant.

$$\Delta m = (k_{1.7} \cdot t)^{\frac{1}{1.7}} \tag{15}$$

where $k_{1.7}$ is the ”1.7” reaction rate constant.

Lastly, these equations are also utilized in comparing the measured thermogravimetric analysis results to the predicted scale growth results. Due to high variation within the results of the AISI 309 experiments, this comparison may not be accurate. Due to low scaling amounts, measurement noise and other possible interference the experimental results for AISI 441 are not comparable to the predicted scale growths. More feasible

results for AISI 309 and AISI 441 could be achieved through a higher number of experiments. The results for the AISI 304 experiments are fully comparable to the predicted results. The comparison between measured and predicted scale growth for AISI 304 and AISI 309 are presented in **Figures 66 – 83.** Averages for measured results are used, where available.

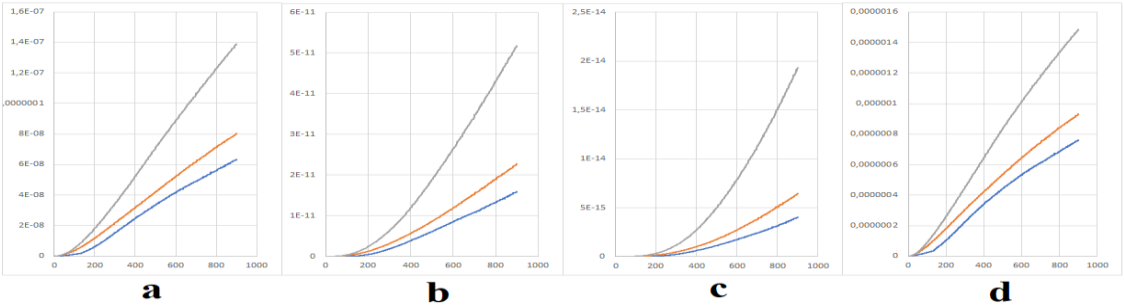

Figure 43. Different models for AISI 304 annealed in the CH_4 Air atmosphere: Parabola (a), Cubic (b), Quadratic (c) and 1.7 (d). Temperatures: 1200 °C (blue), 1225 °C (orange) and 1250 °C (gray).

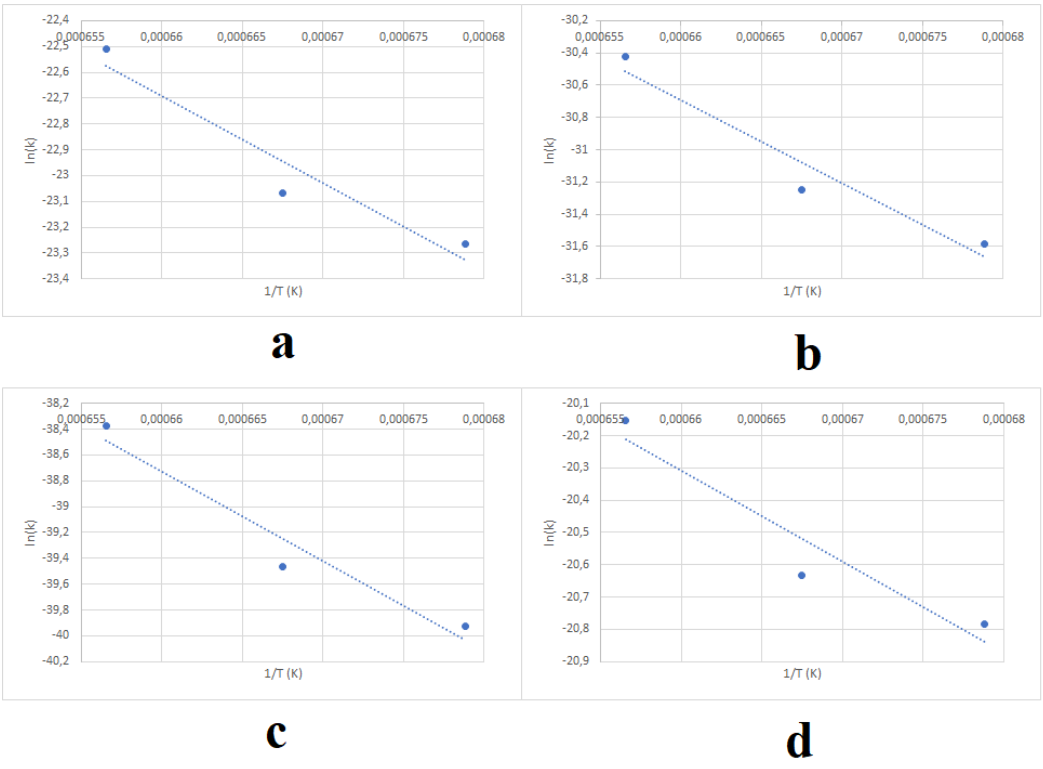

Figure 44. Arrhenius plots with trend lines for models for AISI 304 annealed in the CH_4 Air atmosphere: Parabola (a), Cubic (b), Quadratic (c) and 1.7 (d)

Table 8. Activation energies and frequency factors for models for AISI 304 annealed in the CH_4 Air atmosphere.

AISI 304 CH_4 Air		
	Activation energy (J/(K*mol))	Frequency factor
Parabolic	2.8E+05	6.5E-01
Cubic	4.3E+05	3.2E+01
Quadratic	5.8E+05	1.2E+03
1.7	2.3E+05	1.8E-01

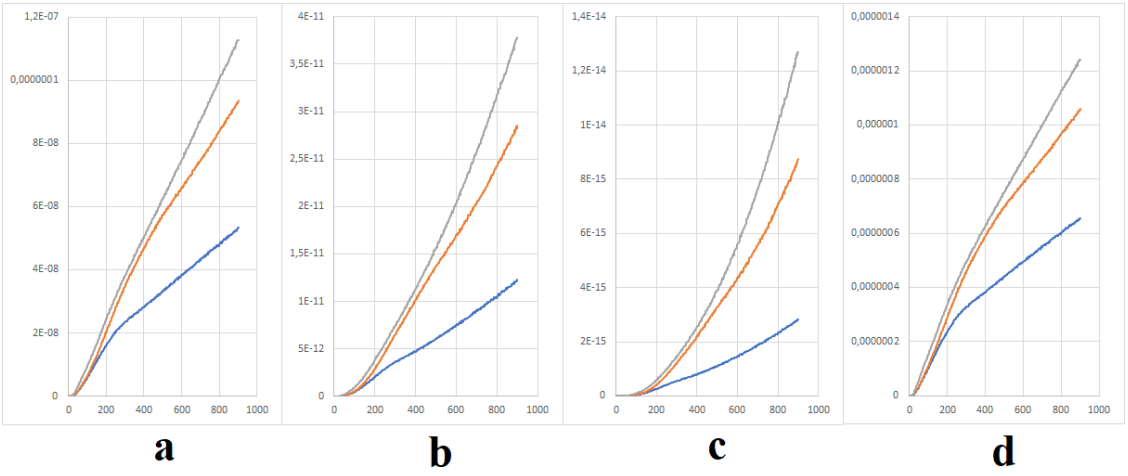

Figure 45. Different models for AISI 304 annealed in the CH_4 Oxyfuel atmosphere: Parabola (a), Cubic (b), Quadratic (c) and 1.7 (d). Temperatures: 1200 °C (blue), 1225 °C (orange) and 1250 °C (gray).

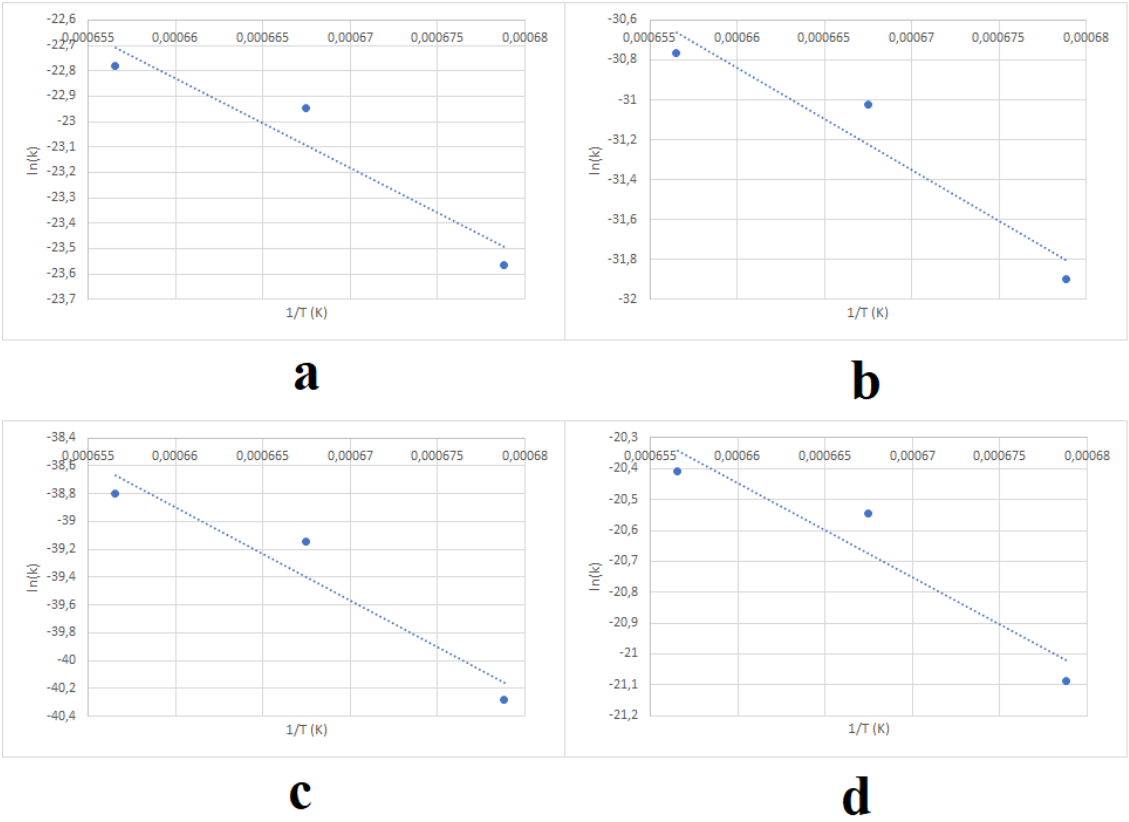

Figure 46. Arrhenius plots with trend lines for models for AISI 304 annealed in the CH_4 Oxyfuel atmosphere: Parabola (a), Cubic (b), Quadratic (c) and 1.7 (d).

Table 9. Activation energies and frequency factors for models for AISI 304 annealed in the CH_4 Oxyfuel atmosphere.

AISI 304 CH_4 Oxyfuel		
	Activation energy (J/(K*mol))	Frequency factor
Parabolic	2.9E+05	1.6E+00
Cubic	4.2E+05	1.6E+01
Quadratic	5.6E+05	1.8E+02
1.7	2.5E+05	7.9E-01

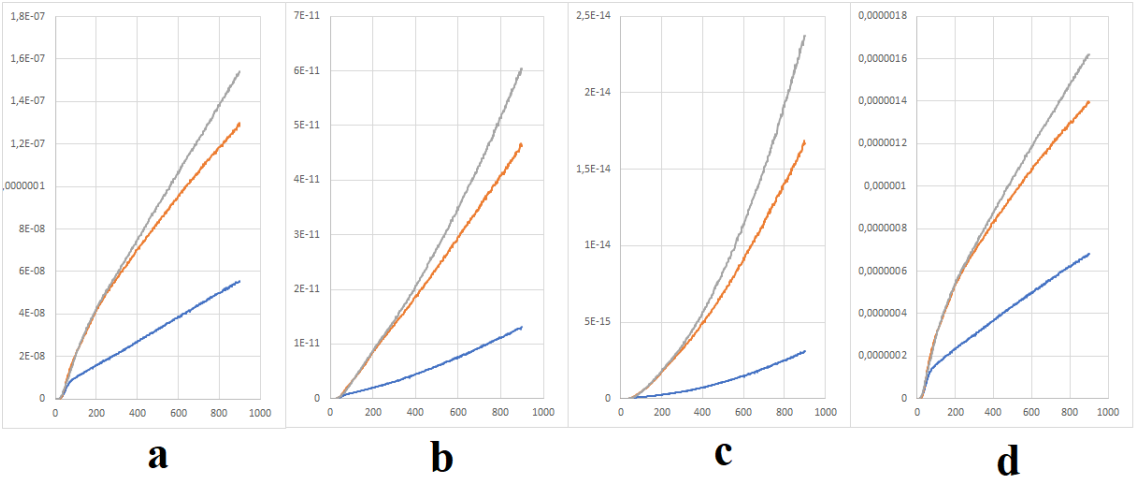

Figure 47. Different models for AISI 304 annealed in the H_2 Oxyfuel atmosphere: Parabola (a), Cubic (b), Quadratic (c) and 1.7 (d). Temperatures: 1200 °C (blue), 1225 °C (orange) and 1250 °C (gray).

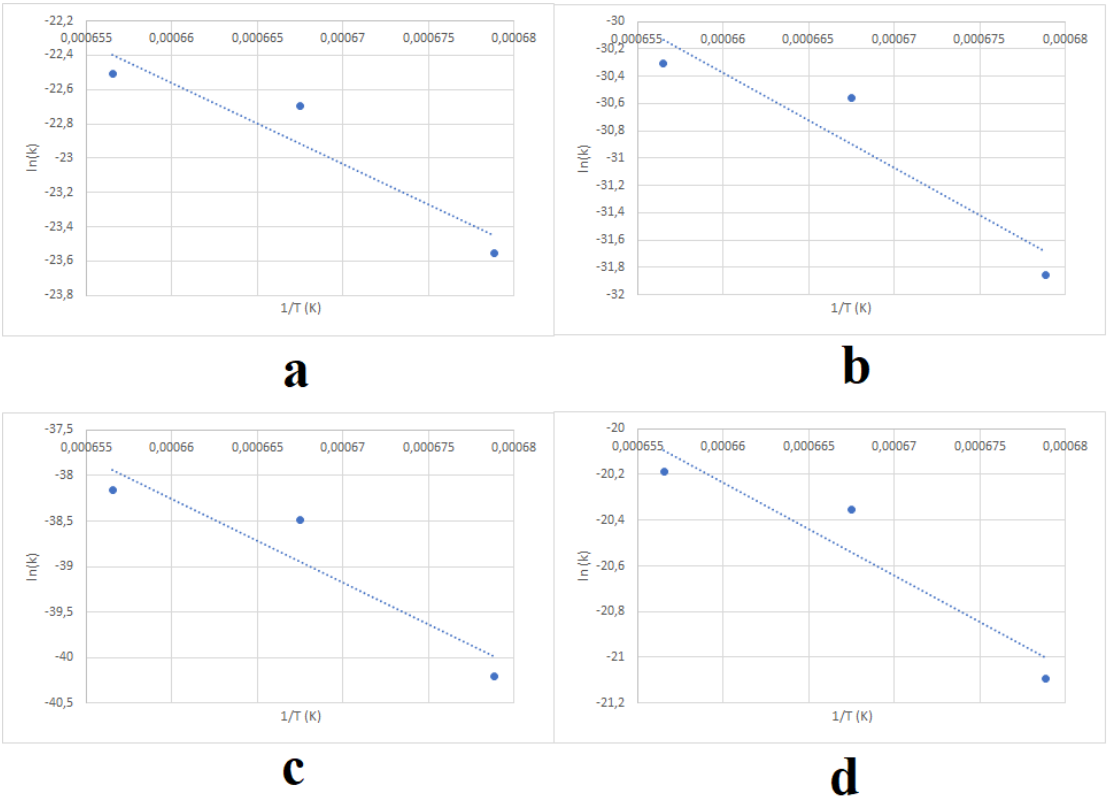

Figure 48. Arrhenius plots with trend lines for models for AISI 304 annealed in the H_2 Oxyfuel atmosphere: Parabola (a), Cubic (b), Quadratic (c) and 1.7 (d).

Table 10. Activation energies and frequency factors for models for AISI 304 annealed in the H_2 Oxyfuel atmosphere.

AISI 304 H_2 Oxyfuel		
	Activation energy (J/(K*mol))	Frequency factor
Parabolic	3.9E+05	5.7E+03
Cubic	5.8E+05	5.6E+06
Quadratic	7.7E+05	6.4E+09
1.7	3.4E+05	7.5E+02

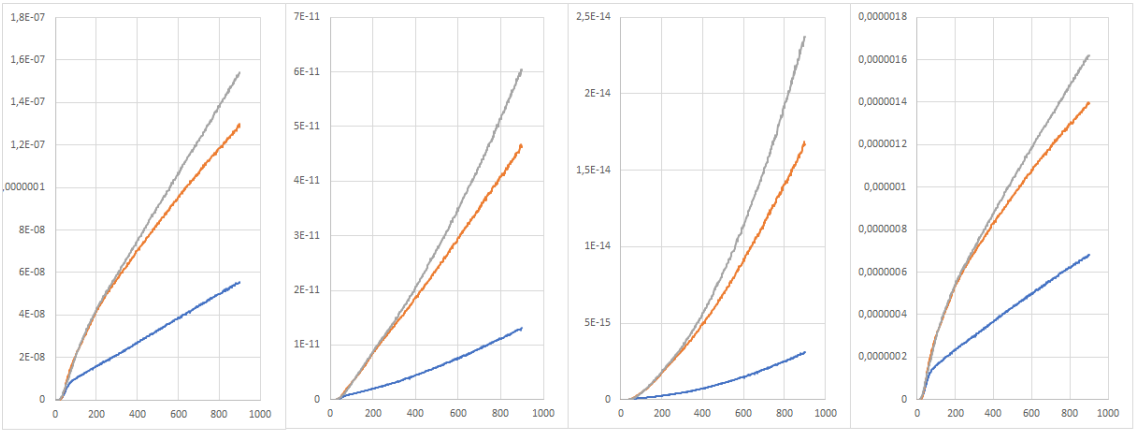

Figure 49. Different models for AISI 309 annealed in the CH_4 Air atmosphere: Parabola (a), Cubic (b), Quadratic (c) and 1.7 (d). Temperatures: 1200 °C (blue), 1225 °C (orange) and 1250 °C (gray).

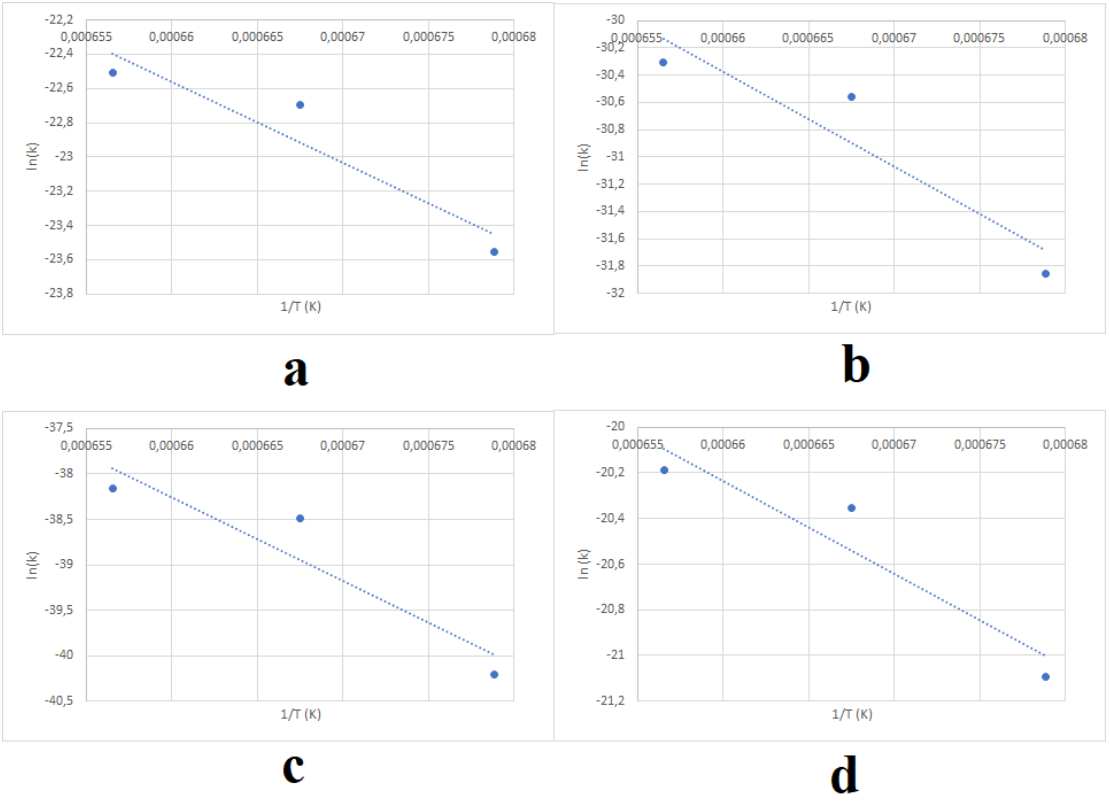

Figure 50. Arrhenius plots with trend lines for models for AISI 309 annealed in the CH_4 Air atmosphere: Parabola (a), Cubic (b), Quadratic (c) and 1.7 (d).

Table 11. Activation energies and frequency factors for models for AISI 309 annealed in the CH_4 Air atmosphere.

AISI 309 CH_4 Air		
	Avtication energy (J/(K*mol))	Frequency factor
Parabolic	1.2E+06	1.9E+30
Cubic	1.7E+06	2.1E+43
Quadratic	2.2E+06	2.6E+56
1.7	1.0E+06	4.3E-27

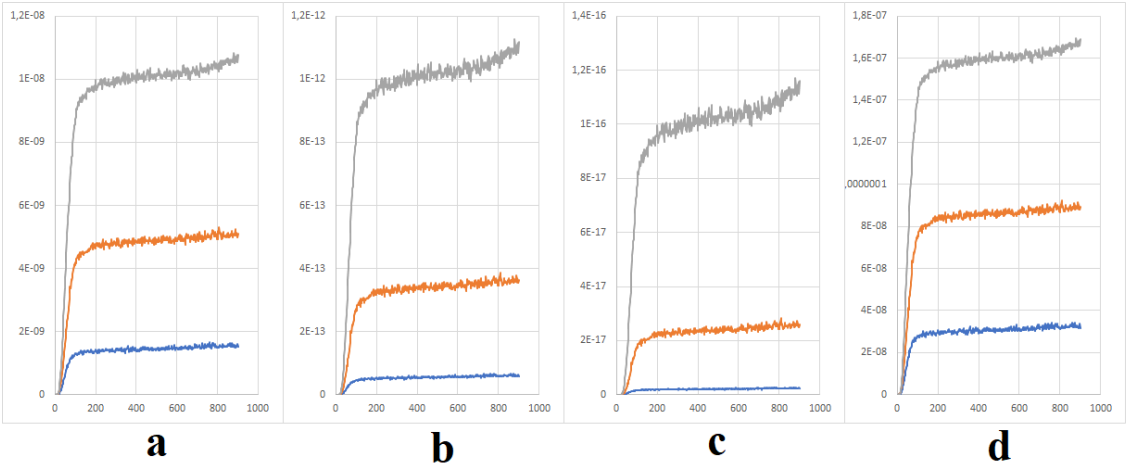

Figure 51. Different models for AISI 309 annealed in the CH_4 Oxyfuel atmosphere: Parabola (a), Cubic (b), Quadratic (c) and 1.7 (d). Temperatures: 1200 °C (blue), 1225 °C (orange) and 1250 °C (gray).

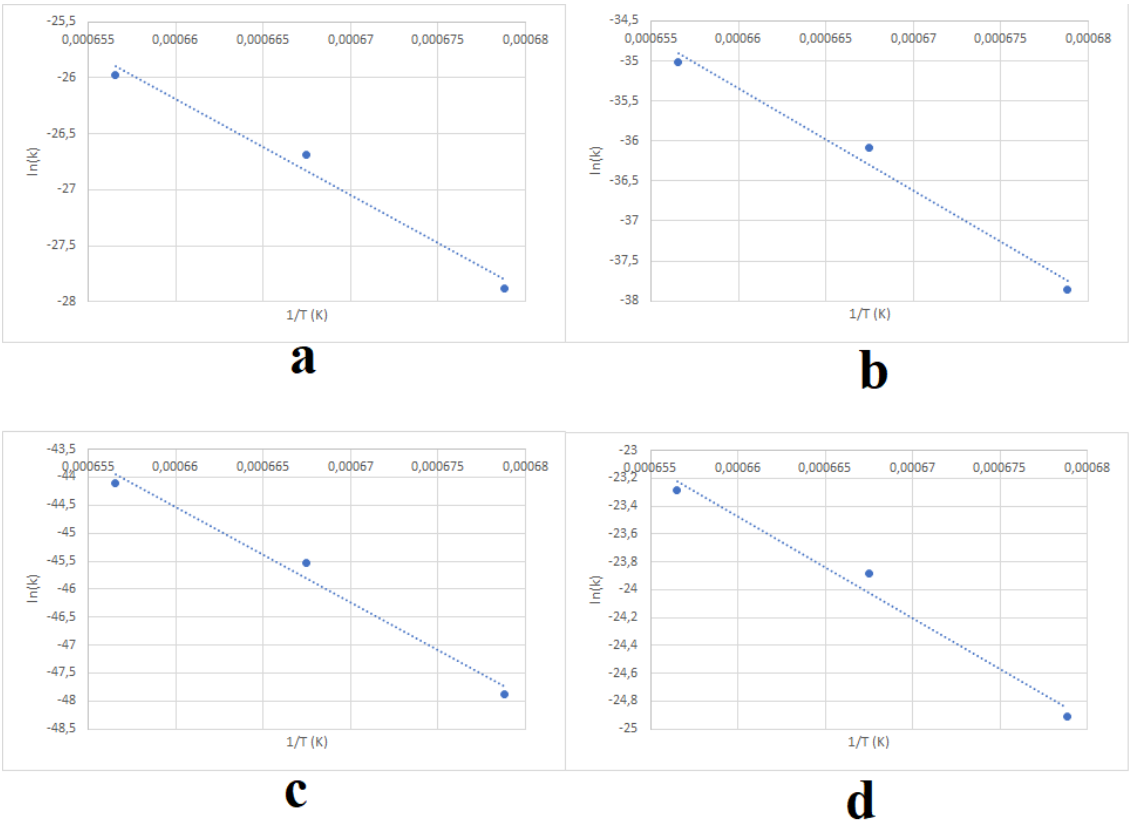

Figure 52. Arrhenius plots with trend lines for models for AISI 309 annealed in the CH_4 Oxyfuel atmosphere: Parabola (a), Cubic (b), Quadratic (c) and 1.7 (d).

Table 11. Activation energies and frequency factors for models for AISI 309 annealed in the CH_4 Oxyfuel atmosphere.

AISI 309 CH_4 Oxyfuel		
	Activation energy (J/(K*mol))	Frequency factor
Parabolic	7.1E+05	1.4E+13
Cubic	1.1E+06	1.7E+21
Quadratic	1.4E+06	2.1E+29
1.7	6.1E+05	5.1E+10

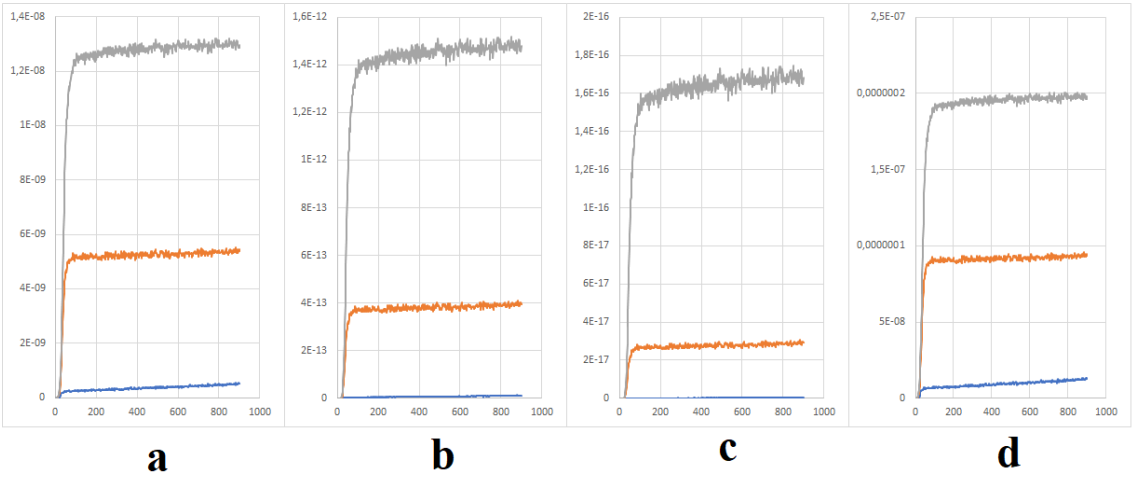

Figure 53. Different models for AISI 309 annealed in the H_2 Oxyfuel atmosphere: Parabola (a), Cubic (b), Quadratic (c) and 1.7 (d). Temperatures: 1200 °C (blue), 1225 °C (orange) and 1250 °C (gray).

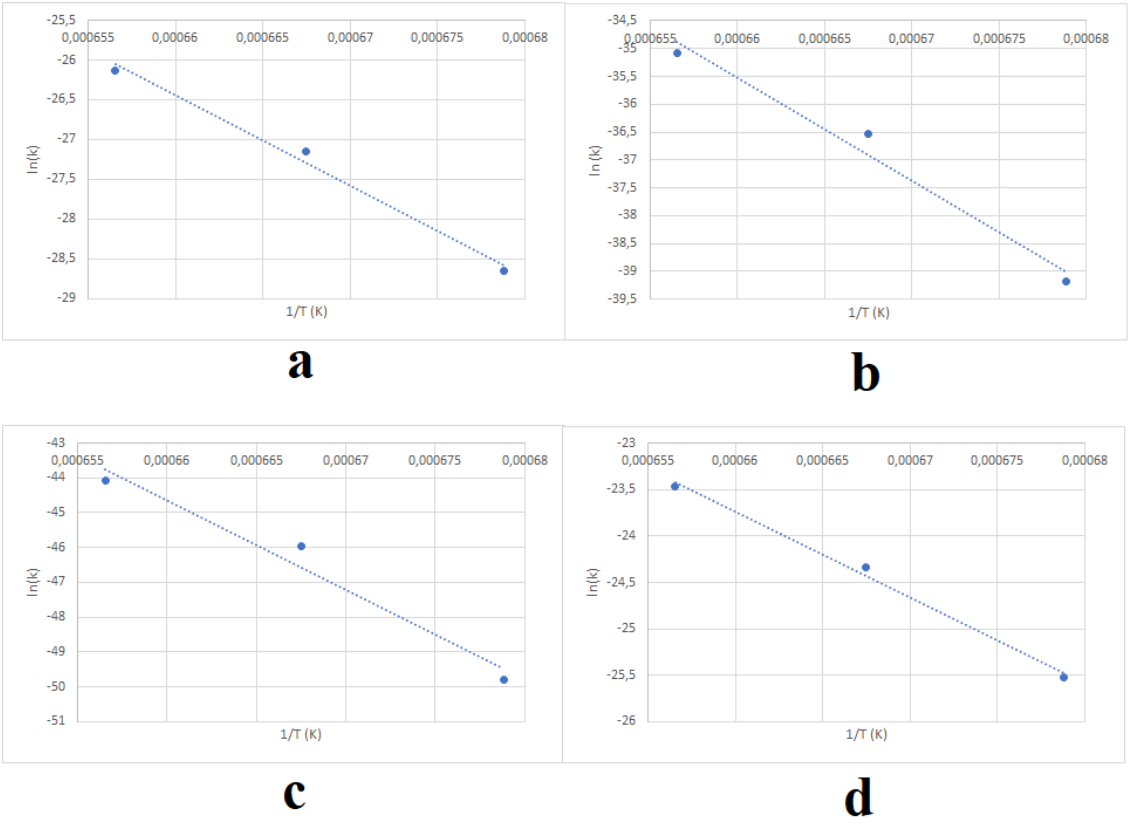

Figure 54. Arrhenius plots with trend lines for models for AISI 309 annealed in the H_2 Oxyfuel atmosphere: Parabola (a), Cubic (b), Quadratic (c) and 1.7 (d)

Table 12. Activation energies and frequency factors for models for AISI 309 annealed in the H_2 Oxyfuel atmosphere.

AISI 309 H_2 Oxyfuel		
	Activation energy (J/(K*mol))	Frequency factor
Parabolic	9.4E+05	9.8E+20
Cubic	1.5E+06	2.5E+37
Quadratic	2.1E+06	2.3E+54
1.7	7.7E+05	1.7E+16

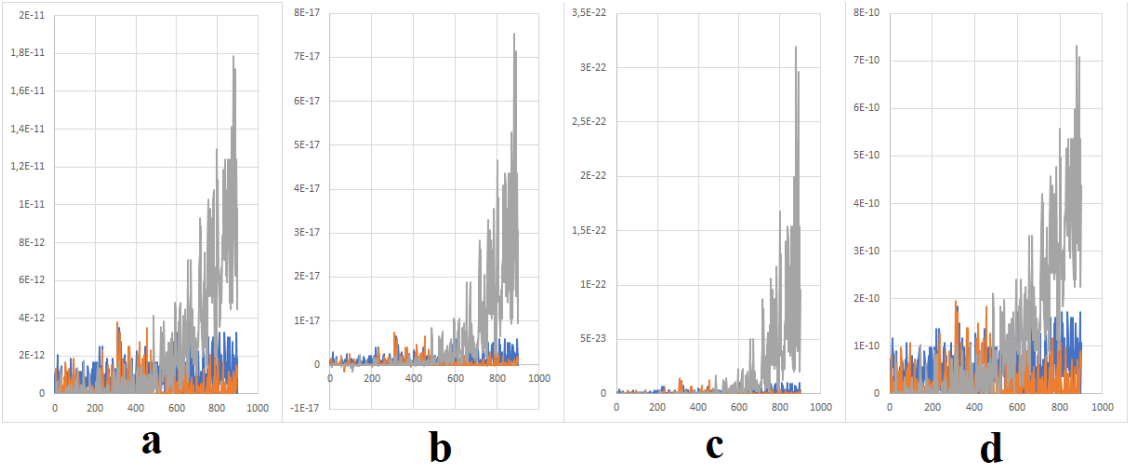

Figure 55. Different models for AISI 441 annealed in the CH_4 Air atmosphere: Parabola (a), Cubic (b), Quadratic (c) and 1.7 (d). Temperatures: 1200 °C (blue), 1225 °C (orange) and 1250 °C (gray).

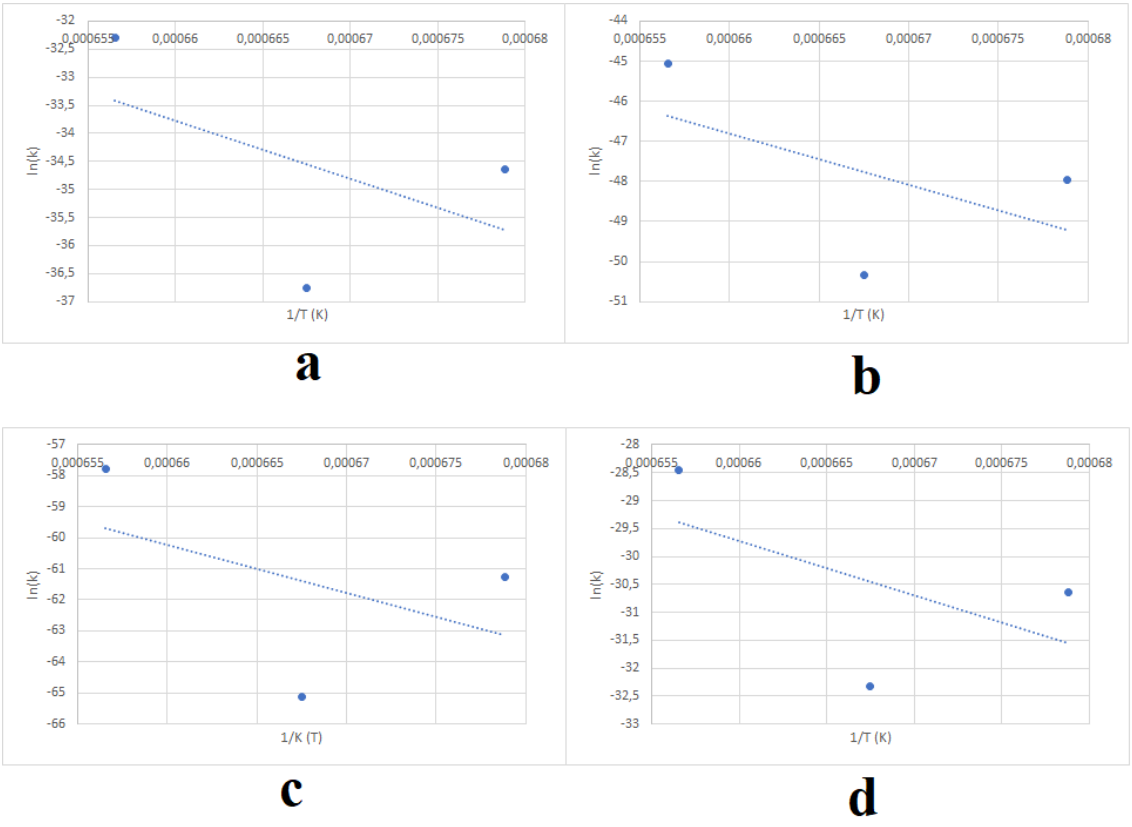

Figure 56. Arrhenius plots with trend lines for models for AISI 441 annealed in the CH_4 Air atmosphere: Parabola (a), Cubic (b), Quadratic (c) and 1.7 (d).

Table 13. Activation energies and frequency factors for models for AISI 441 annealed in the CH_4 Air atmosphere.

AISI 441 CH_4 Air		
	Activation energy (J/(K*mol))	Frequency factor
Parabolic	8.6E+05	1.1E+15
Cubic	1.1E+06	3.1E+16
Quadratic	1.3E+06	1.6E+18
1.7	8.1E+05	1.0E+15

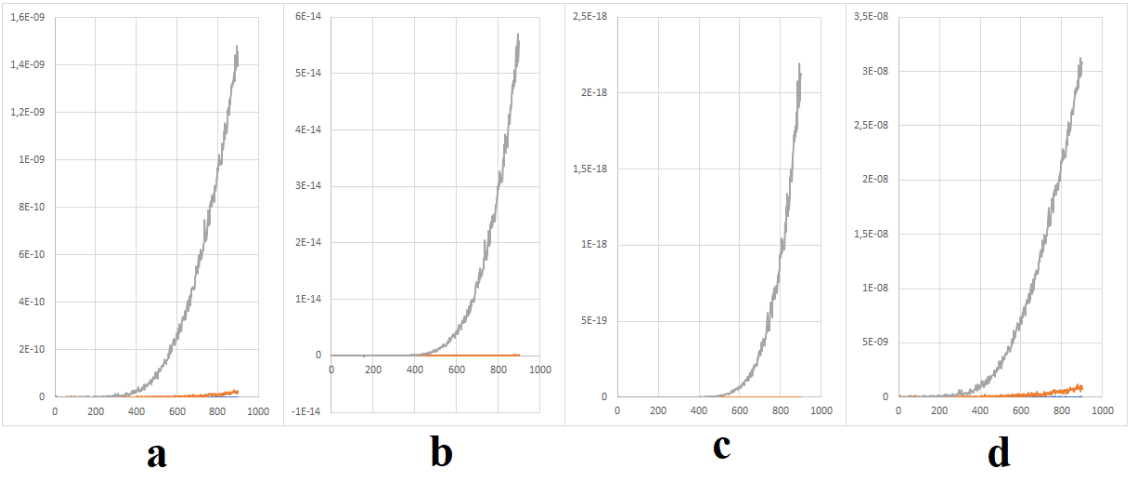

Figure 57. Different models for AISI 441 annealed in the CH_4 Oxyfuel atmosphere: Parabola (a), Cubic (b), Quadratic (c) and 1.7 (d). Temperatures: 1200 °C (blue), 1225 °C (orange) and 1250 °C (gray).

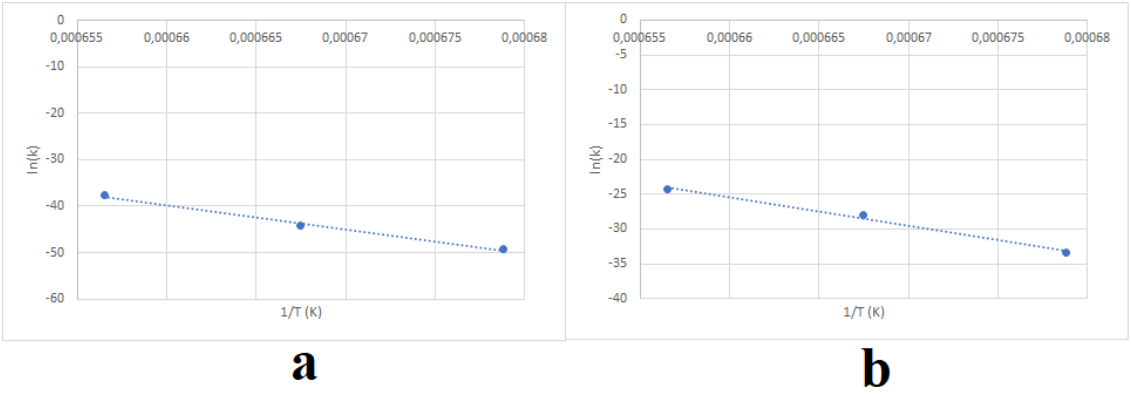

Figure 58. Arrhenius plots with trend lines for models for AISI 441 annealed in the CH_4 Oxyfuel atmosphere: Cubic (a) and 1.7 (b).

Table 14. Activation energies and frequency factors for models for AISI 441 annealed in the CH_4 Oxyfuel atmosphere.

AISI 441 CH_4 Oxyfuel		
	Activation energy (J/(K*mol))	Frequency factor
Cubic	4.3E+06	1.1E+131
1.7	3.4E+06	5.6E+106

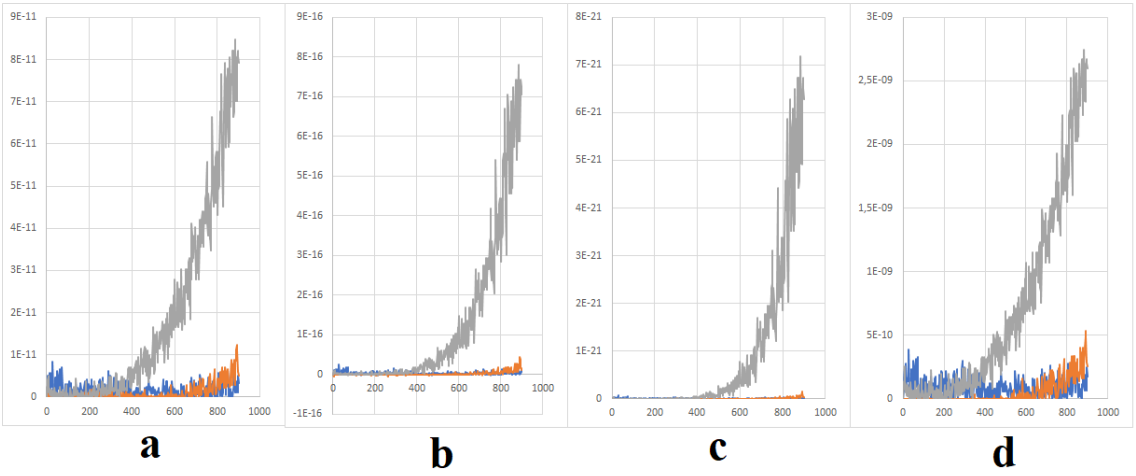

Figure 59. Different models for AISI 441 annealed in the H_2 Oxyfuel atmosphere: Parabola (a), Cubic (b), Quadratic (c) and 1.7 (d). Temperatures: 1200 °C (blue), 1225 °C (orange) and 1250 °C (gray).

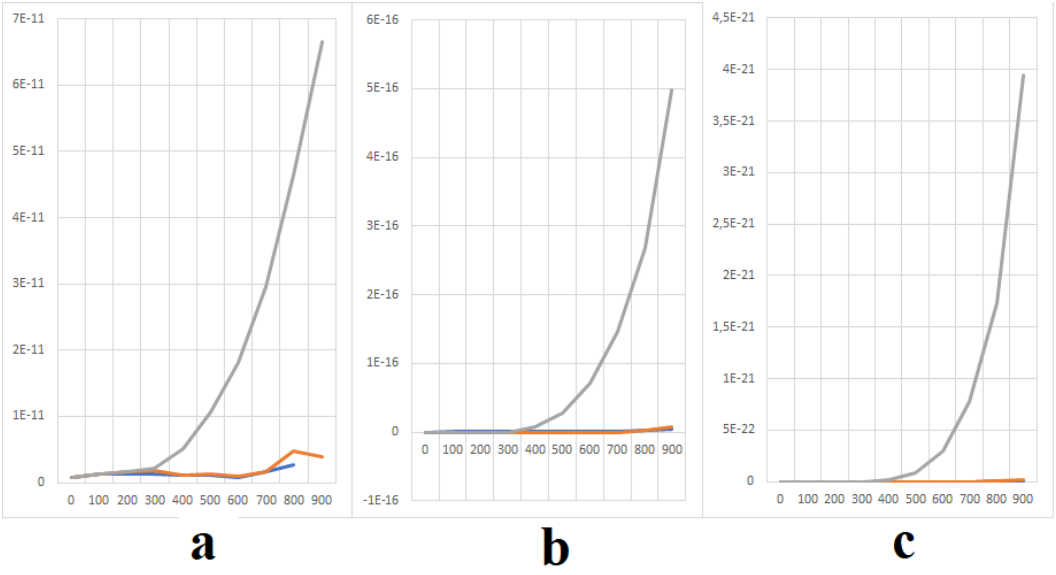

Figure 60. Different models for AISI 441 annealed in the H_2 Oxyfuel atmosphere with average of every 50 measurement points: Parabola (a), Cubic (b), Quadratic (c). Temperatures: 1200 °C (blue), 1225 °C (orange) and 1250 °C (gray).

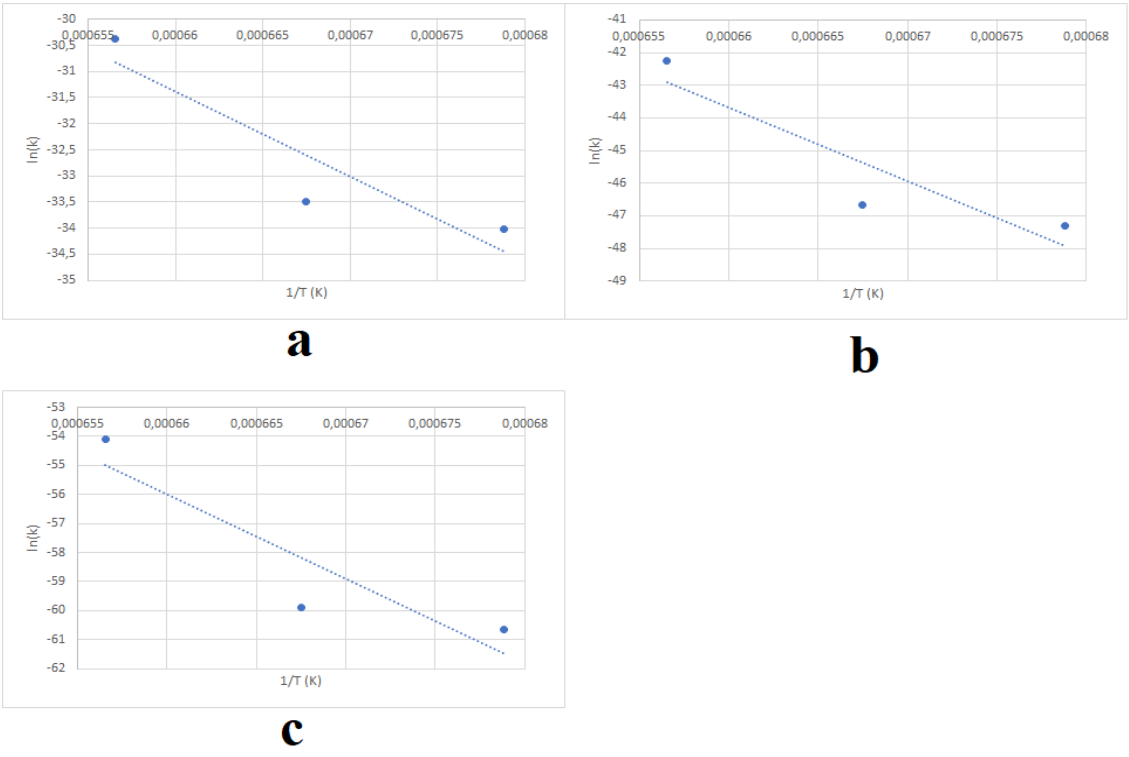

Figure 61. Arrhenius plots with trend lines for models for AISI 441 annealed in the H_2 Oxyfuel atmosphere with average of every 50 measurement points: Parabolic (a), Cubic (c) and Quadratic (c).

Table 15. Activation energies and frequency factors for models for AISI 441 annealed in the H_2 Oxyfuel atmosphere with average of every 50 measurement points.

AISI 441 H_2 Oxyfuel using averages		
	Activation energy (J/(K*mol))	Frequency factor
Parabolic	1.3E+06	7.3E+32
Cubic	1.9E+06	7.2E+45
Quadratic	2.4E+06	2.2E+59

Table 16. Compiled activation energies and frequancy factors.

AISI 304 CH_4 Air		
	Activation energy (J/(K*mol))	Frequency factor
Parabolic	2.8E+05	6.5E-01
Cubic	4.3E+05	3.2E+01
Quadratic	5.8E+05	1.2E+03
1.7	2.3E+05	1.8E-01
AISI 304 CH_4 Oxyfuel		
	Activation energy (J/(K*mol))	Frequency factor
Parabolic	2.9E+05	1.6E+00
Cubic	4.2E+05	1.6E+01
Quadratic	5.6E+05	1.8E+02
1.7	2.5E+05	7.9E-01
AISI 304 H_2 Oxyfuel		
	Activation energy (J/(K*mol))	Frequency factor
Parabolic	3.9E+05	5.7E+03
Cubic	5.8E+05	5.6E+06
Quadratic	7.7E+05	6.4E+09
1.7	3.4E+05	7.5E+02
AISI 309 CH_4 Air		
	Activation energy (J/(K*mol))	Frequency factor
Parabolic	1.2E+06	1.9E+30
Cubic	1.7E+06	2.1E+43
Quadratic	2.2E+06	2.6E+56
1.7	1.0E+06	4.3E-27
AISI 309 CH_4 Oxyfuel		

	Activation energy (J/(K*mol))	Frequency factor
Parabolic	7.1E+05	1.4E+13
Cubic	1.1E+06	1.7E+21
Quadratic	1.4E+06	2.1E+29
1.7	6.1E+05	5.1E+10
AISI 309 H_2 Oxyfuel		
	Activation energy (J/(K*mol))	Frequency factor
Parabolic	9.4E+05	9.8E+20
Cubic	1.5E+06	2.5E+37
Quadratic	2.1E+06	2.3E+54
1.7	7.7E+05	1.7E+16
AISI 441 CH_4 Air		
	Activation energy (J/(K*mol))	Frequency factor
Parabolic	8.6E+05	1.1E+15
Cubic	1.1E+06	3.1E+16
Quadratic	1.3E+06	1.6E+18
1.7	8.1E+05	1.0E+15
AISI 441 CH_4 Oxyfuel		
	Activation energy (J/(K*mol))	Frequency factor
Cubic	4.3E+06	1.1E+131
1.7	3.4E+06	5.6E+106
AISI 441 H_2 Oxyfuel using averages		
	Activation energy (J/(K*mol))	Frequency factor
Parabolic	1.3E+06	7.3E+32
Cubic	1.9E+06	7.2E+45
Quadratic	2.4E+06	2.2E+59

Table 17. Calculated reaction rate constants for every stainless steel grade, atmosphere and model between 1100 °C – 1300 °C for AISI 304.

	AISI 304 CH_4 Air			
	Parabolic	Cubic	Quadratic	1.7
1100 °C	1.4E-11	1.4E-15	1.3E-19	2.2E-10
1125 °C	2.2E-11	2.7E-15	3.3E-19	3.2E-10
1150 °C	3.3E-11	5.2E-15	7.9E-19	4.5E-10
1175 °C	5.0E-11	9.7E-15	1.8E-18	6.4E-10
1200 °C	7.4E-11	1.8E-14	4.1E-18	8.9E-10
1225 °C	1.1E-10	3.2E-14	9.0E-18	1.2E-09
1250 °C	1.6E-10	5.6E-14	1.9E-17	1.7E-09
1275 °C	2.2E-10	9.7E-14	4.0E-17	2.3E-09
1300 °C	3.2E-10	1.7E-13	8.2E-17	3.0E-09
	AISI 304 CH_4 Oxyfuel			
	Parabolic	Cubic	Quadratic	1.7
1100 °C	1.1E-11	1.2E-15	1.3E-19	1.6E-10
1125 °C	1.7E-11	2.4E-15	3.2E-19	2.4E-10
1150 °C	2.7E-11	4.6E-15	7.4E-19	3.6E-10
1175 °C	4.1E-11	8.5E-15	1.7E-18	5.2E-10
1200 °C	6.3E-11	1.5E-14	3.6E-18	7.4E-10
1225 °C	9.3E-11	2.8E-14	7.7E-18	1.0E-09
1250 °C	1.4E-10	4.8E-14	1.6E-17	1.5E-09
1275 °C	2.0E-10	8.3E-14	3.3E-17	2.0E-09
1300 °C	2.9E-10	1.4E-13	6.5E-17	2.8E-09
	AISI 304 H_2 Oxyfuel			
	Parabolic	Cubic	Quadratic	1.7
1100 °C	6.3E-12	5.6E-16	4.5E-20	1.0E-10
1125 °C	1.2E-11	1.4E-15	1.5E-19	1.7E-10
1150 °C	2.1E-11	3.3E-15	4.8E-19	2.9E-10
1175 °C	3.8E-11	7.7E-15	1.5E-18	4.7E-10
1200 °C	6.6E-11	1.7E-14	4.3E-18	7.6E-10
1225 °C	1.1E-10	3.8E-14	1.2E-17	1.2E-09
1250 °C	1.9E-10	8.2E-14	3.4E-17	1.9E-09
1275 °C	3.1E-10	1.7E-13	8.9E-17	2.9E-09
1300 °C	5.0E-10	3.5E-13	2.3E-16	4.4E-09

Table 18. Calculated reaction rate constants for every stainless steel grade, atmosphere and model between 1100 °C – 1300 °C for AISI 309.

	AISI 309 CH_4 Air			
	Parabolic	Cubic	Quadratic	1.7
1100 °C	8.9E-16	2.5E-21	6.4E-27	7.6E-67
1125 °C	5.8E-15	3.4E-20	1.9E-25	3.9E-66
1150 °C	3.5E-14	4.4E-19	5.1E-24	1.9E-65
1175 °C	2.0E-13	5.1E-18	1.2E-22	8.7E-65
1200 °C	1.1E-12	5.4E-17	2.6E-21	3.8E-64
1225 °C	5.4E-12	5.3E-16	5.0E-20	1.6E-63
1250 °C	2.6E-11	4.9E-15	8.8E-19	6.2E-63
1275 °C	1.2E-10	4.2E-14	1.4E-17	2.4E-62
1300 °C	5.2E-10	3.3E-13	2.0E-16	8.6E-62
	AISI 309 CH_4 Oxyfuel			
	Parabolic	Cubic	Quadratic	1.7
1100 °C	1.2E-14	7.4E-20	4.2E-25	4.4E-13
1125 °C	3.7E-14	3.9E-19	3.8E-24	1.1E-12
1150 °C	1.1E-13	1.9E-18	3.2E-23	2.8E-12
1175 °C	3.1E-13	9.1E-18	2.5E-22	6.9E-12
1200 °C	8.4E-13	4.0E-17	1.9E-21	1.6E-11
1225 °C	2.2E-12	1.7E-16	1.3E-20	3.7E-11
1250 °C	5.6E-12	7.0E-16	8.2E-20	8.2E-11
1275 °C	1.4E-11	2.7E-15	4.9E-19	1.8E-10
1300 °C	3.4E-11	1.0E-14	2.8E-18	3.8E-10
	AISI 309 H_2 Oxyfuel			
	Parabolic	Cubic	Quadratic	1.7
1100 °C	1.4E-15	1.3E-21	9.7E-28	8.8E-14
1125 °C	6.3E-15	1.4E-20	2.8E-26	2.9E-13
1150 °C	2.6E-14	1.4E-19	7.0E-25	9.4E-13
1175 °C	1.0E-13	1.3E-18	1.6E-23	2.9E-12
1200 °C	3.9E-13	1.2E-17	3.2E-22	8.6E-12
1225 °C	1.4E-12	9.4E-17	6.0E-21	2.5E-11
1250 °C	4.8E-12	7.1E-16	1.0E-19	6.8E-11
1275 °C	1.6E-11	5.0E-15	1.5E-18	1.8E-10
1300 °C	5.1E-11	3.3E-14	2.1E-17	4.7E-10

Table 19. Calculated reaction rate constants for every stainless steel grade, atmosphere and model between 1100 °C – 1300 °C for AISI 441.

	AISI 441 CH_4 Air			
	Parabolic	Cubic	Quadratic	1.7
1100 °C	1.8E-18	7.3E-25	1.8E-31	1.6E-16
1125 °C	7.0E-18	3.9E-24	1.4E-30	5.6E-16
1150 °C	2.6E-17	2.0E-23	9.6E-30	1.9E-15
1175 °C	9.1E-17	9.3E-23	6.3E-29	6.2E-15
1200 °C	3.1E-16	4.2E-22	3.8E-28	2.0E-14
1225 °C	9.9E-16	1.8E-21	2.2E-27	5.9E-14
1250 °C	3.1E-15	7.4E-21	1.2E-26	1.7E-13
1275 °C	9.2E-15	2.9E-20	6.2E-26	4.8E-13
1300 °C	2.7E-14	1.1E-19	3.1E-25	1.3E-12
	AISI 441 CH_4 Oxyfuel			
	Parabolic	Cubic	Quadratic	1.7
1100 °C		2.4E-33		1.1E-23
1125 °C		2.0E-30		2.2E-21
1150 °C		1.4E-27		3.9E-19
1175 °C		7.3E-25		5.6E-17
1200 °C		3.1E-22		6.9E-15
1225 °C		1.1E-19		7.1E-13
1250 °C		3.2E-17		6.4E-11
1275 °C		7.7E-15		4.9E-09
1300 °C		1.6E-12		3.3E-07
	AISI 441 H_2 Oxyfuel			
	Parabolic	Cubic	Quadratic	1.7
1100 °C	3.6E-19	2.1E-26	1.1E-33	
1125 °C	3.0E-18	4.0E-25	4.9E-32	
1150 °C	2.3E-17	6.9E-24	1.9E-30	
1175 °C	1.6E-16	1.1E-22	6.6E-29	
1200 °C	1.1E-15	1.5E-21	2.0E-27	
1225 °C	6.9E-15	2.0E-20	5.5E-26	
1250 °C	4.1E-14	2.3E-19	1.3E-24	
1275 °C	2.3E-13	2.6E-18	3.0E-23	
1300 °C	1.2E-12	2.6E-17	5.9E-22	

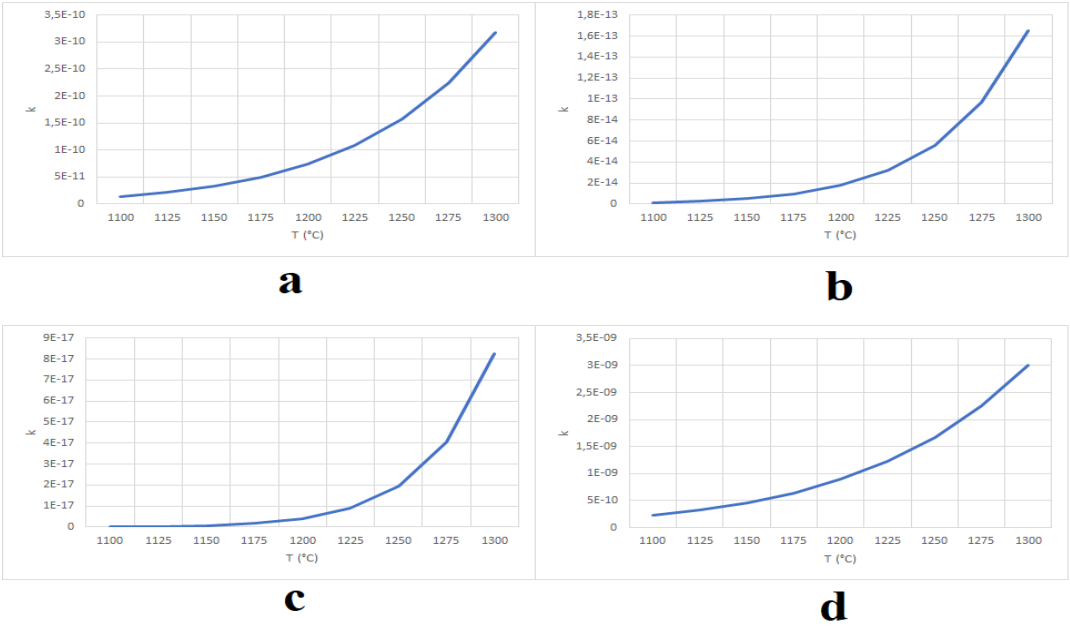

Figure 62. Reaction rate constants (k) in the CH_4 Air atmosphere between 1100 °C and 1300 °C using all four models: Parabolic (a), Cubic (b), Quadratic (c) and 1.7 (d).

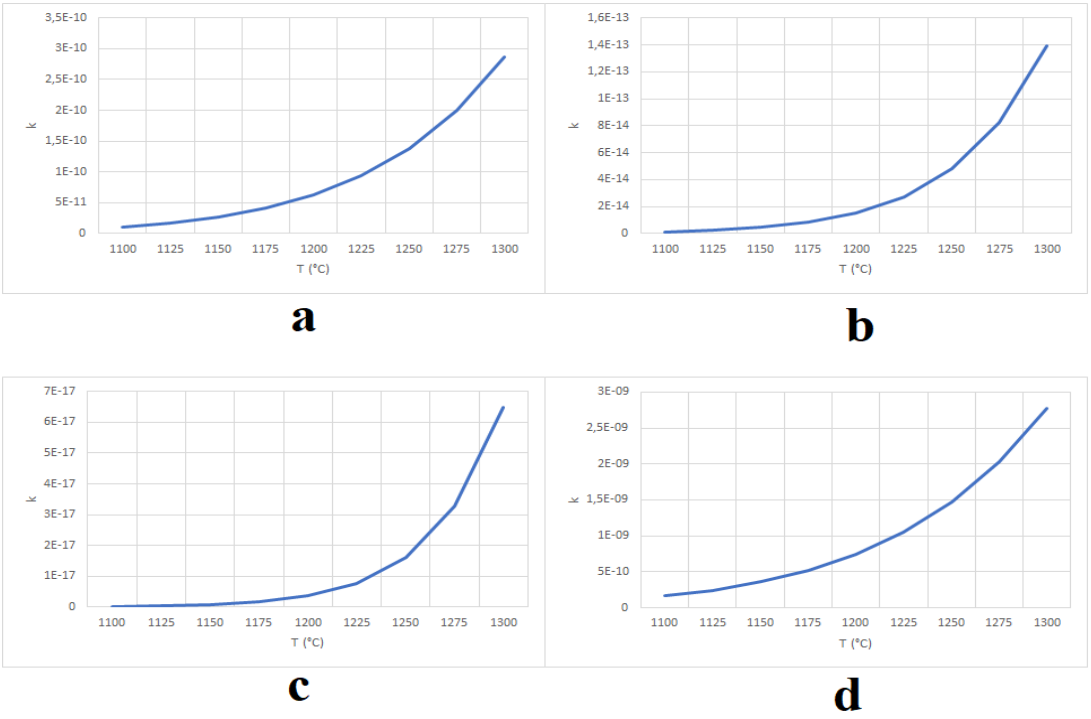

Figure 63. Reaction rate constants (k) in the CH_4 Oxyfuel atmosphere between 1100 °C and 1300 °C using all four models: Parabolic (a), Cubic (b), Quadratic (c) and 1.7 (d).

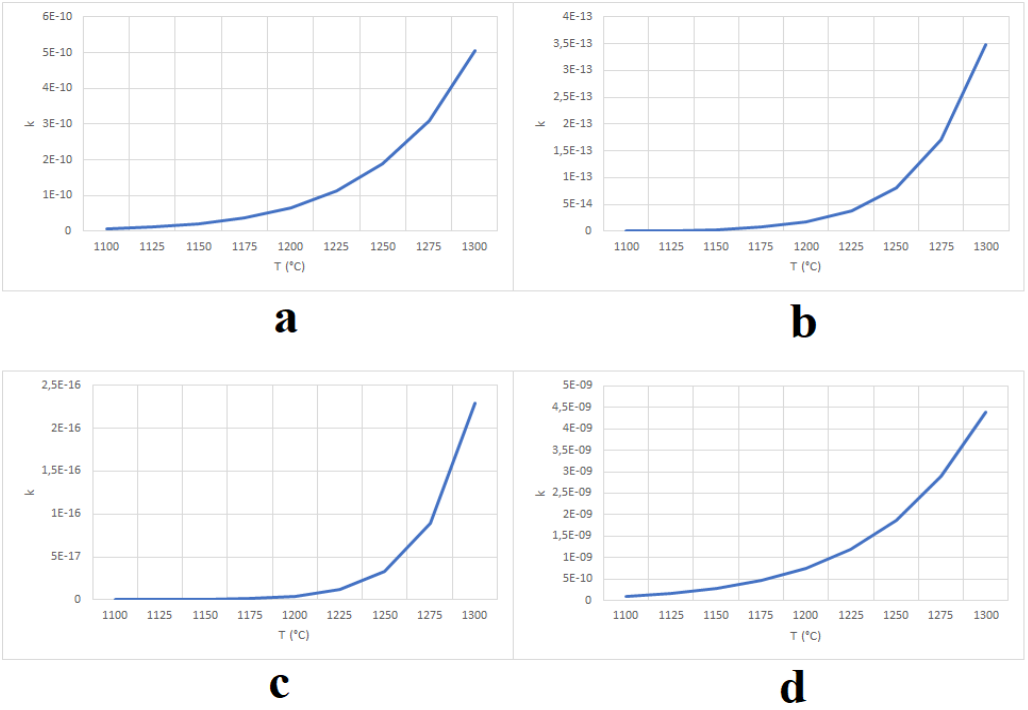

Figure 64. Reaction rate constants (k) in the H_2 Oxyfuel atmosphere between 1100 °C and 1300 °C using all four models: Parabolic (a), Cubic (b), Quadratic (c) and 1.7 (d).

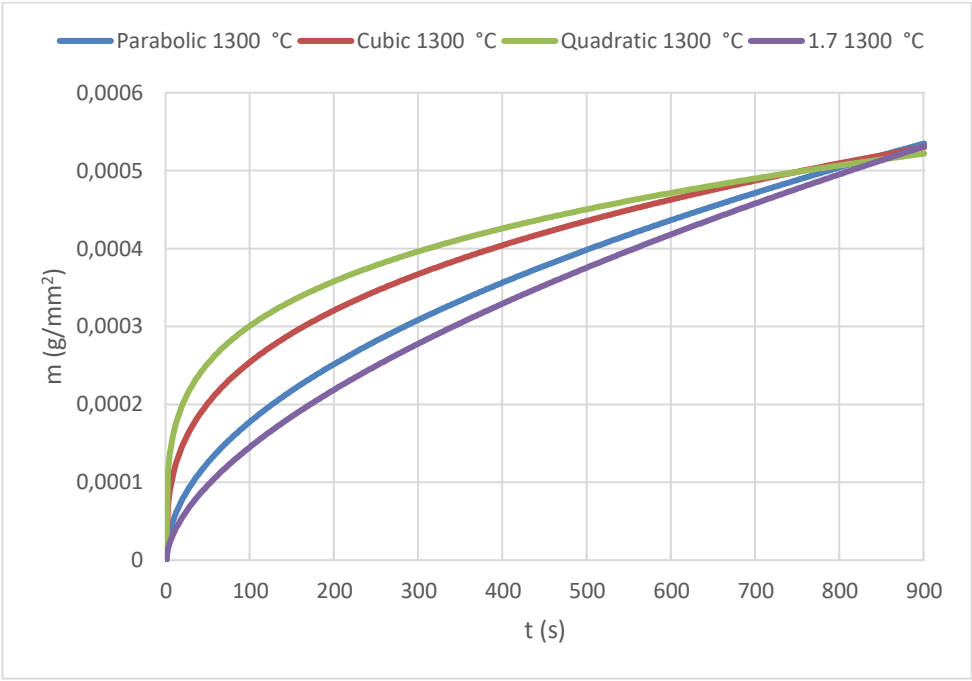

Figure 65. Predicted scale growth AISI 304 annealed for 15 minutes at 1300 °C in the CH_4 Air atmosphere.

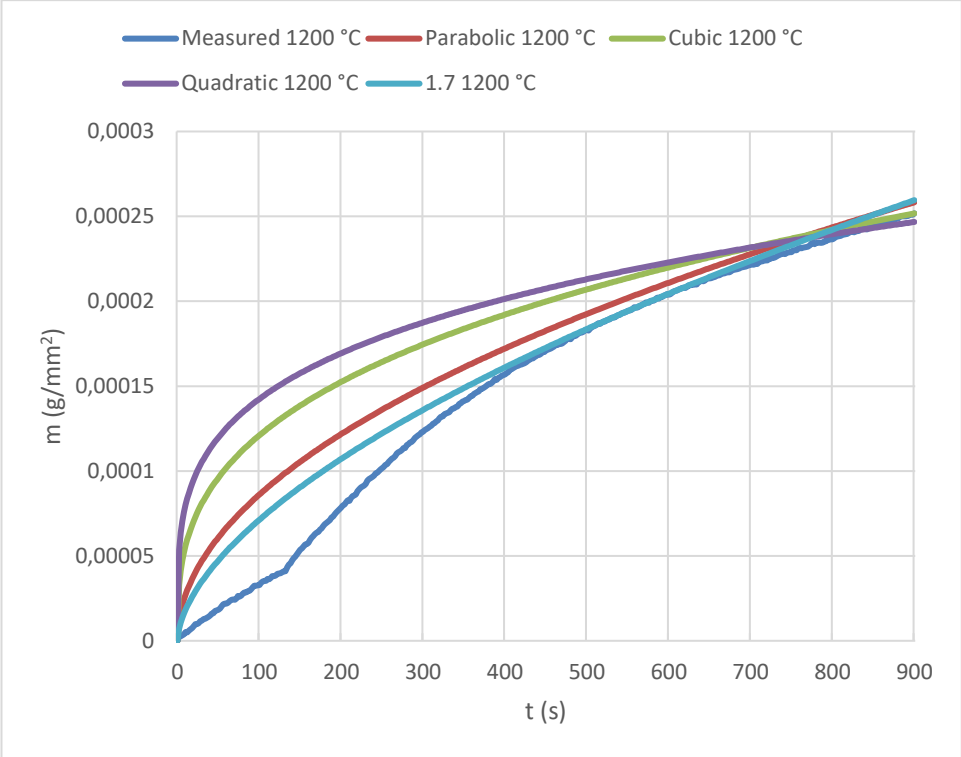

Figure 66. Comparison of measured and predicted scale growth calculated with all four models on AISI 304 at 1200 °C in the CH_4 Air atmosphere.

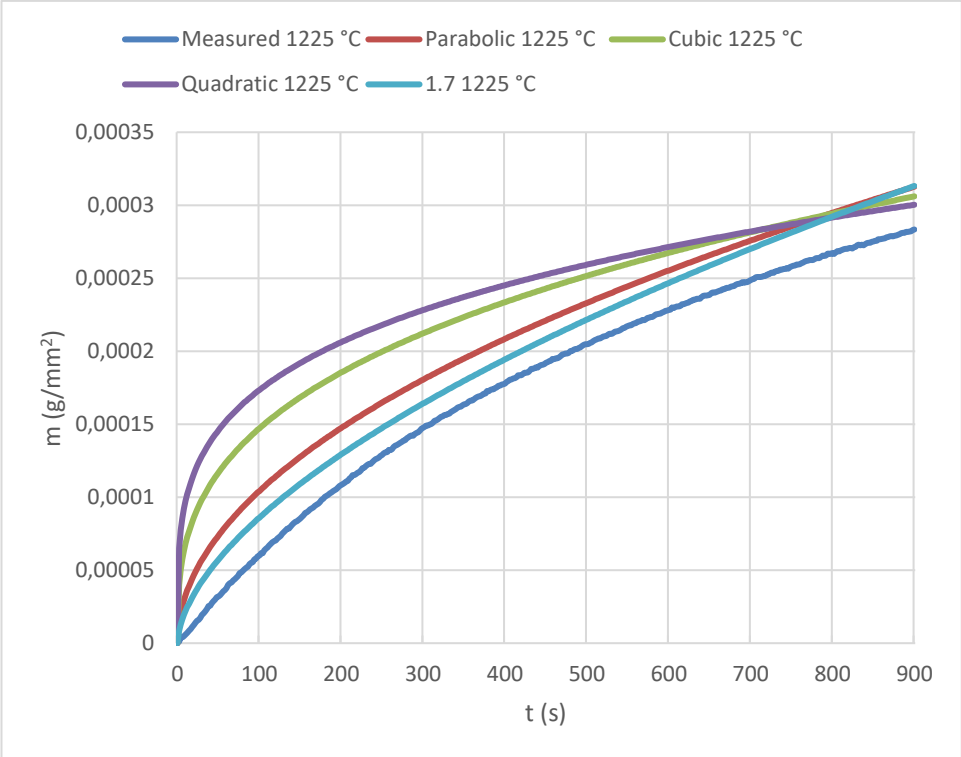

Figure 67. Comparison of measured and predicted scale growth calculated with all four models on AISI 304 at 1225 °C in the CH_4 Air atmosphere.

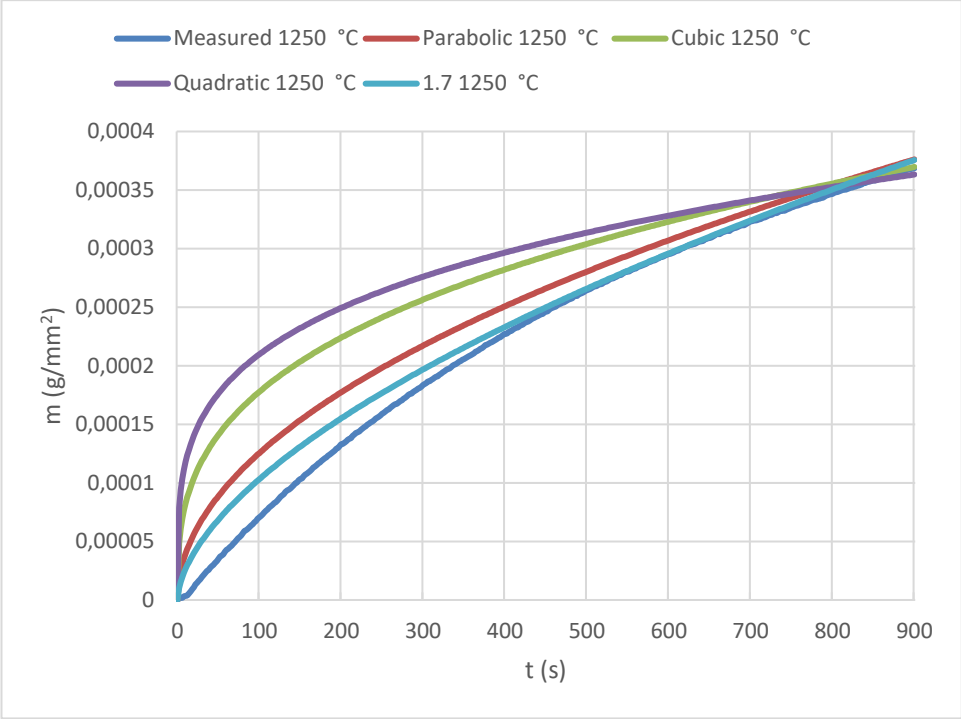

Figure 68. Comparison of measured and predicted scale growth calculated with all four models on AISI 304 at 1250 °C in the CH_4 Air atmosphere.

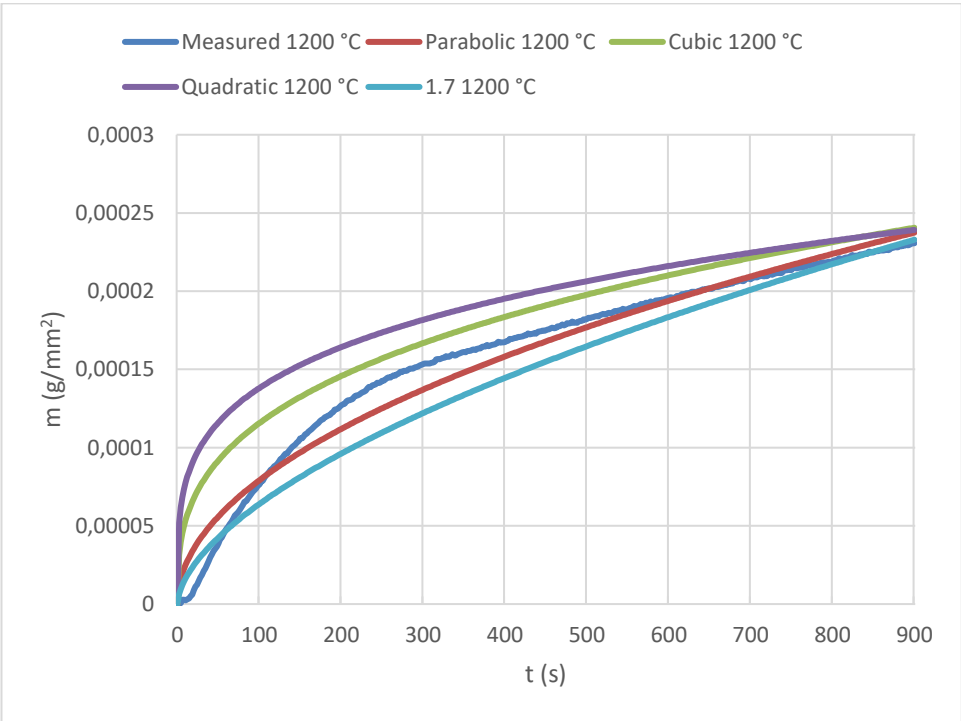

Figure 69. Comparison of measured and predicted scale growth calculated with all four models on AISI 304 at 1200 °C in the CH_4 Oxyfuel atmosphere.

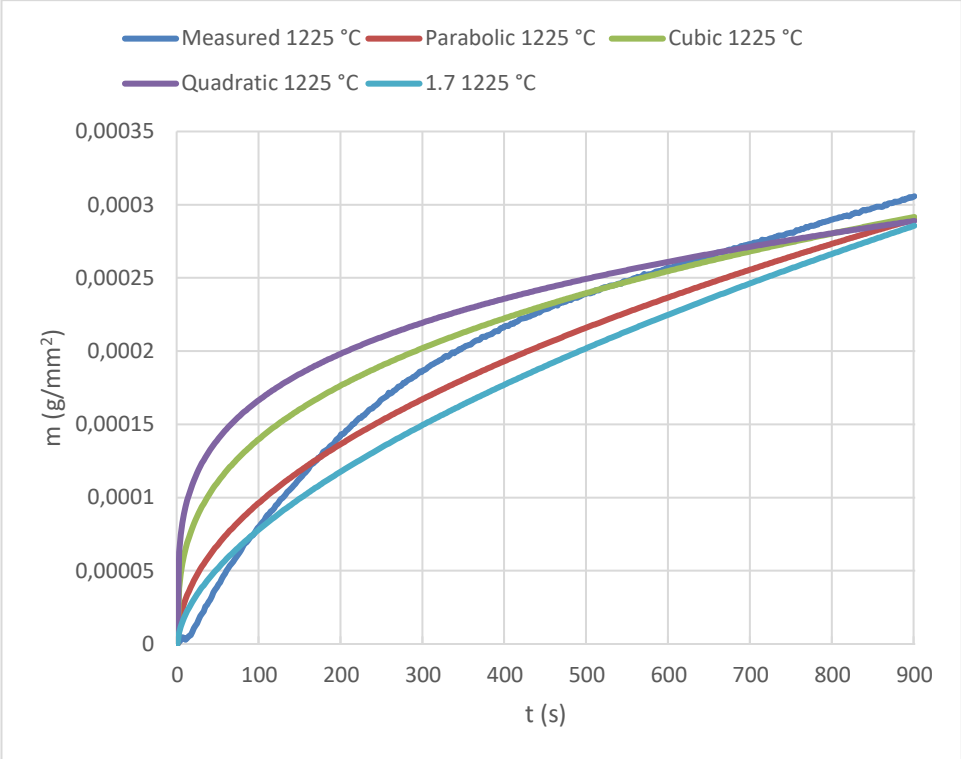

Figure 70. Comparison of measured and predicted scale growth calculated with all four models on AISI 304 at 1225 °C in the CH_4 Oxyfuel atmosphere.

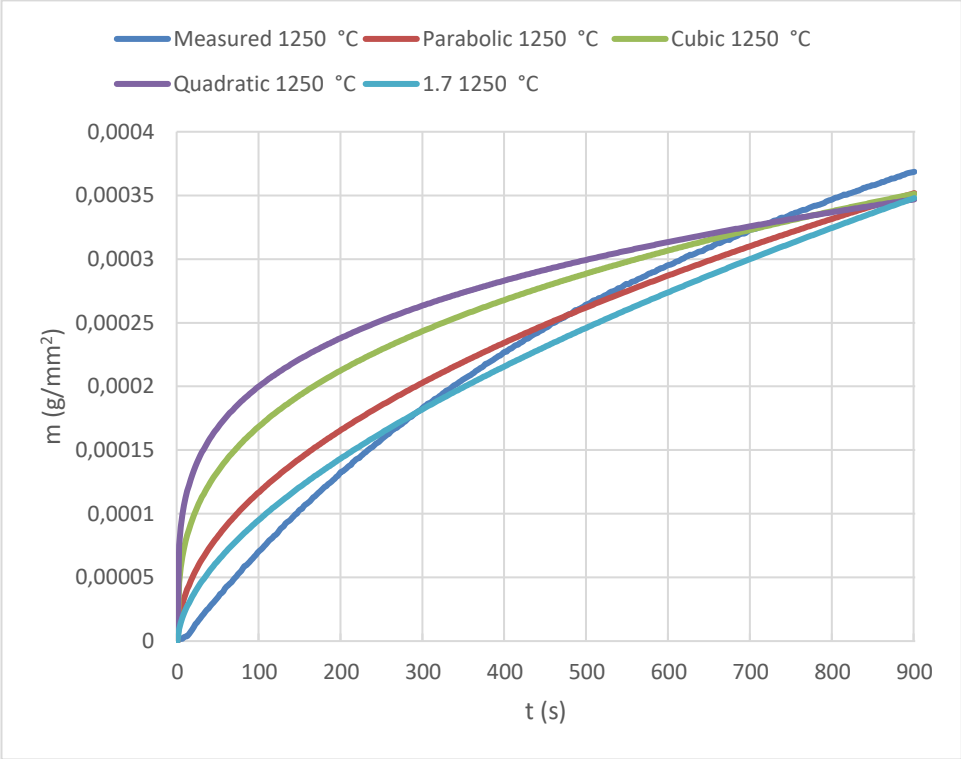

Figure 71. Comparison of measured and predicted scale growth calculated with all four models on AISI 304 at 1250 °C in the CH_4 Oxyfuel atmosphere.

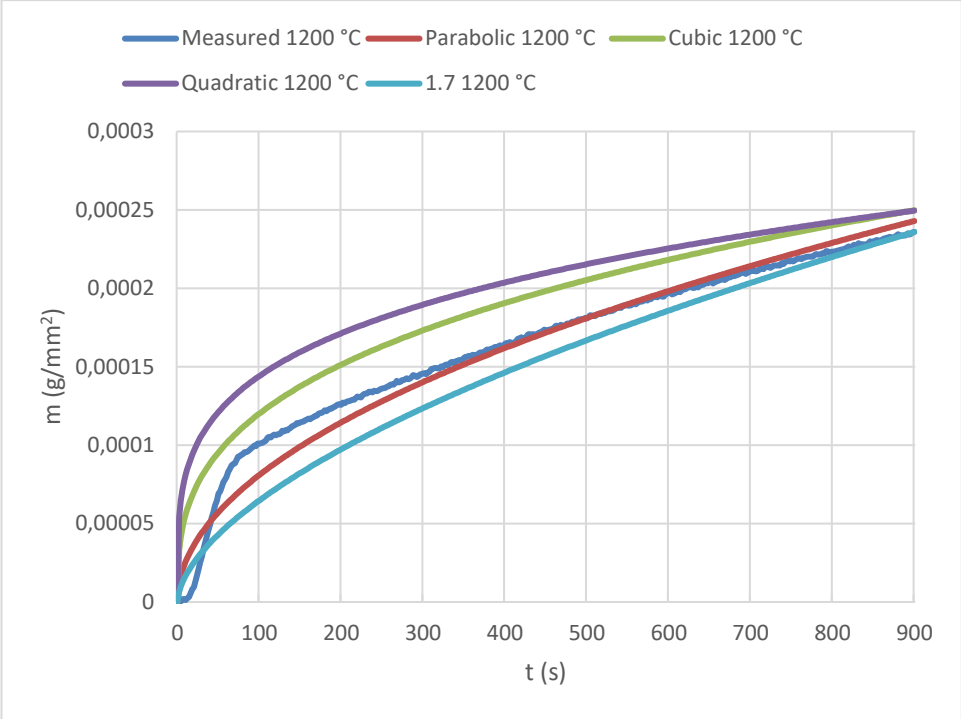

Figure 72. Comparison of measured and predicted scale growth calculated with all four models on AISI 304 at 1200 °C in the H_2 Oxyfuel atmosphere.

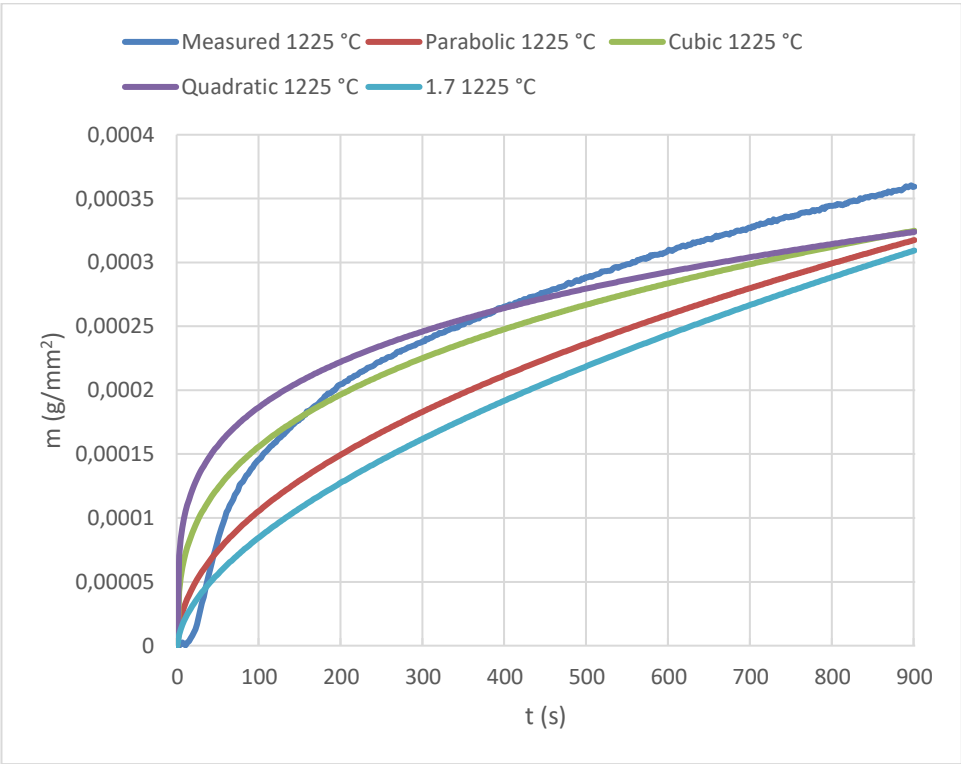

Figure 73. Comparison of measured and predicted scale growth calculated with all four models on AISI 304 at 1225 °C in the H_2 Oxyfuel atmosphere.

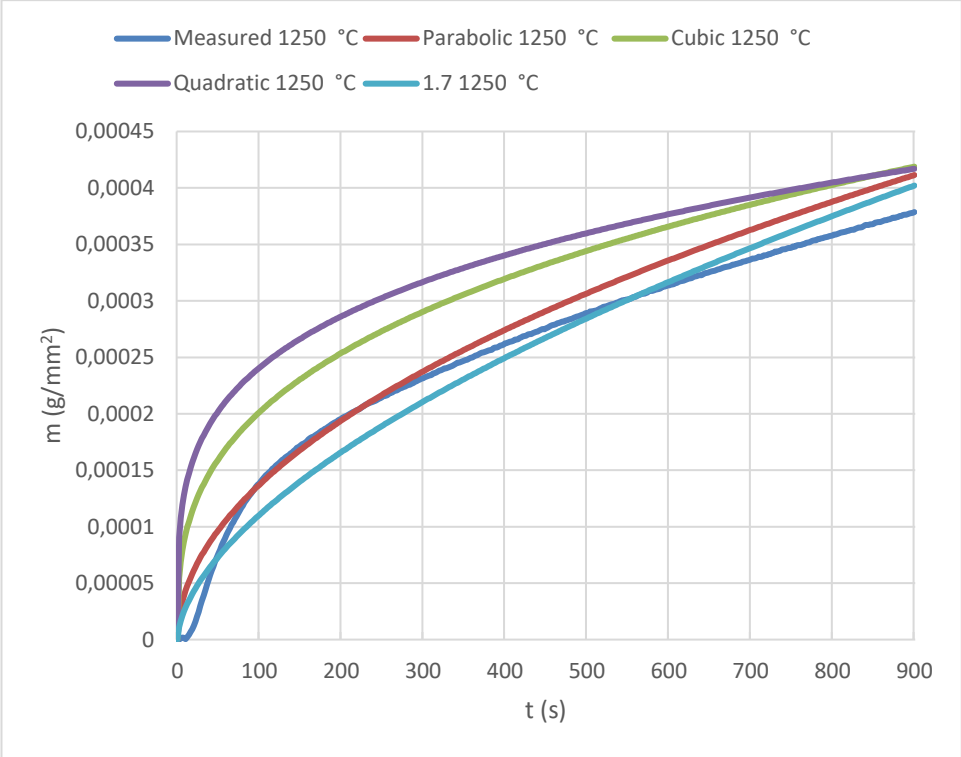

Figure 74. Comparison of measured and predicted scale growth calculated with all four models on AISI 304 at 1250 °C in the H_2 Oxyfuel atmosphere.

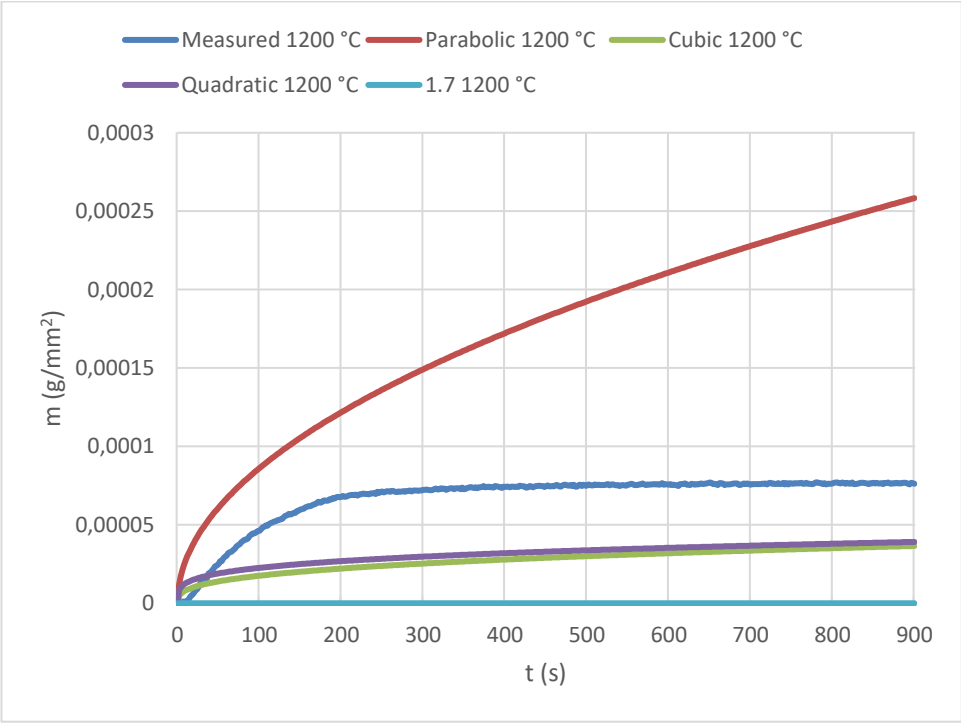

Figure 75. Comparison of measured and predicted scale growth calculated with all four models on AISI 309 at 1200 °C in the CH_4 Air atmosphere.

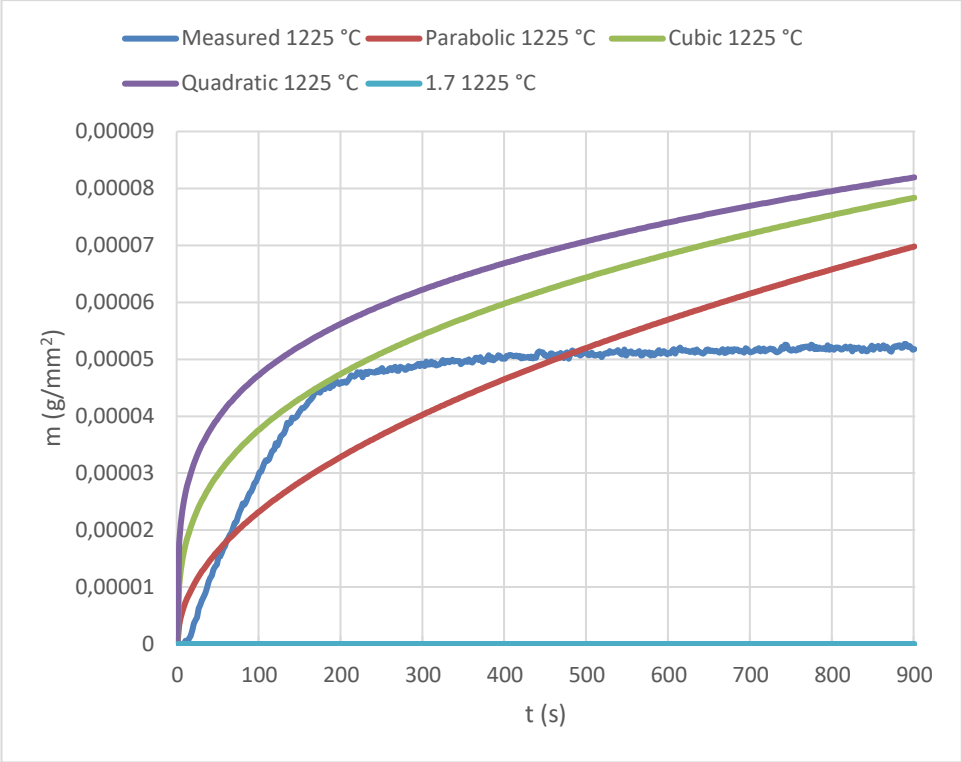

Figure 76. Comparison of measured and predicted scale growth calculated with all four models on AISI 309 at 1225 °C in the CH_4 Air atmosphere.

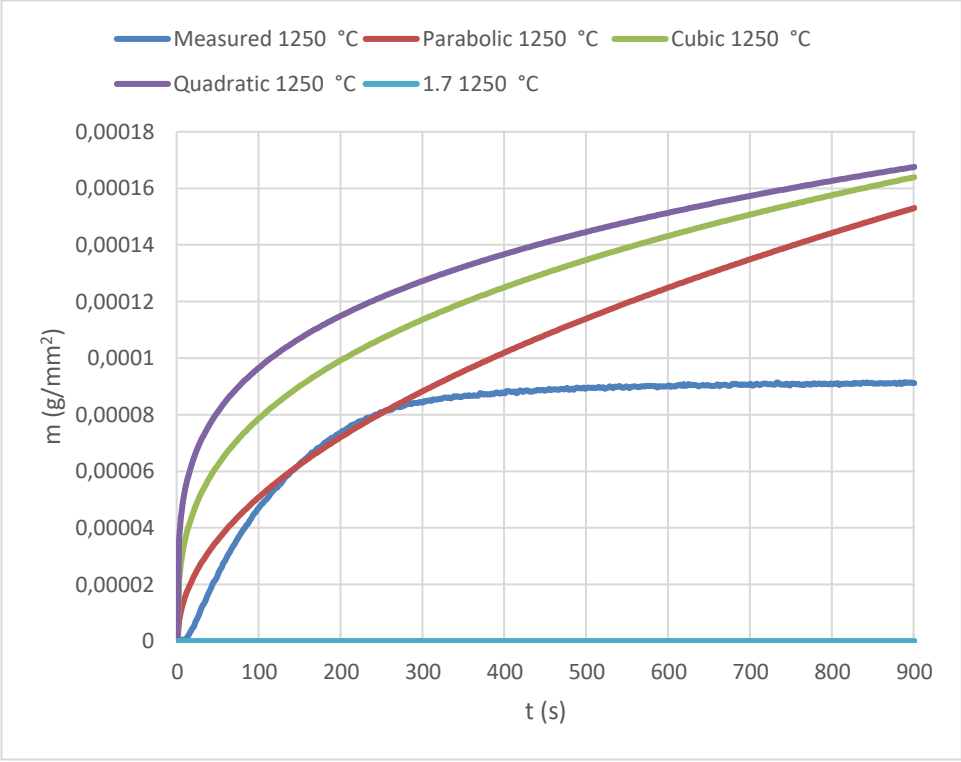

Figure 77. Comparison of measured and predicted scale growth calculated with all four models on AISI 309 at 1250 °C in the CH_4 Air atmosphere.

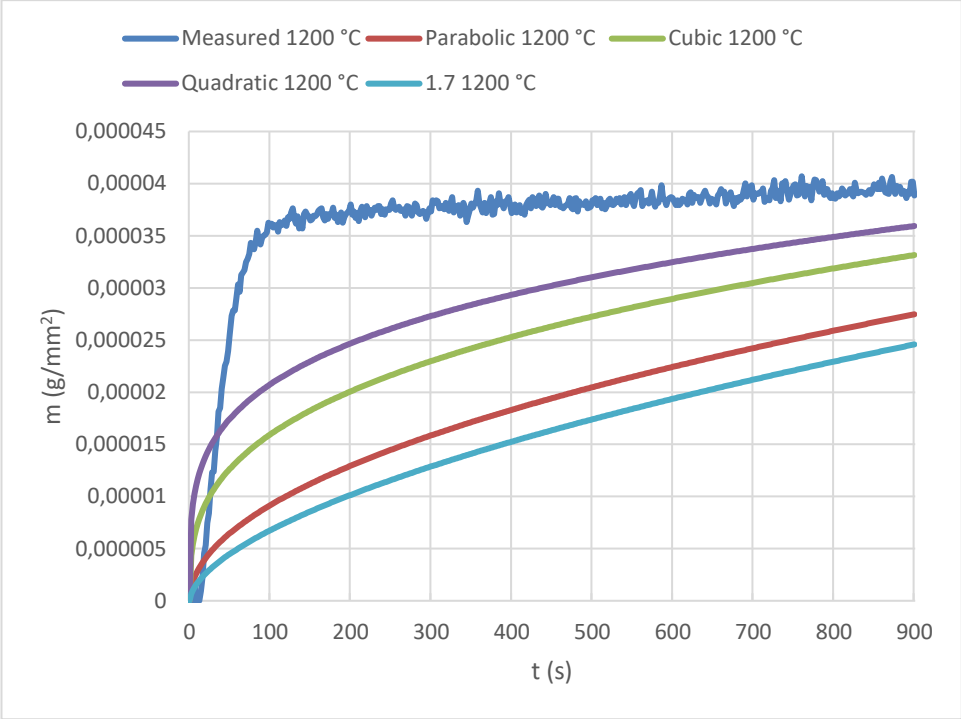

Figure 78. Comparison of measured and predicted scale growth calculated with all four models on AISI 309 at 1200 °C in the CH_4 Oxyfuel atmosphere.

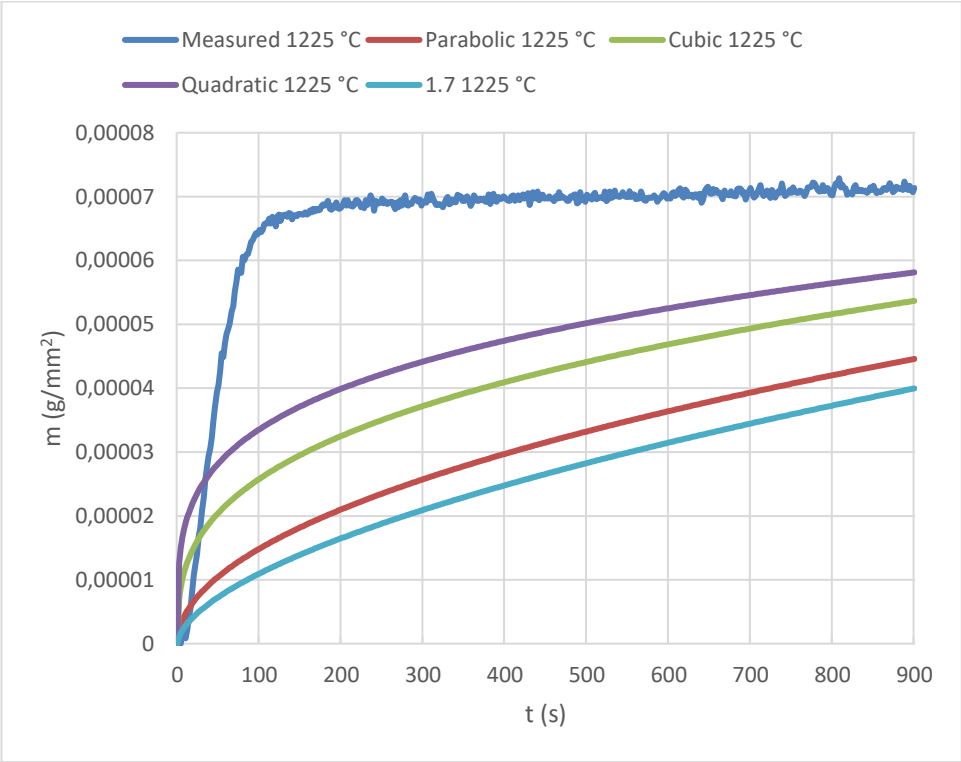

Figure 79. Comparison of measured and predicted scale growth calculated with all four models on AISI 309 at 1225 °C in the CH_4 Oxyfuel atmosphere.

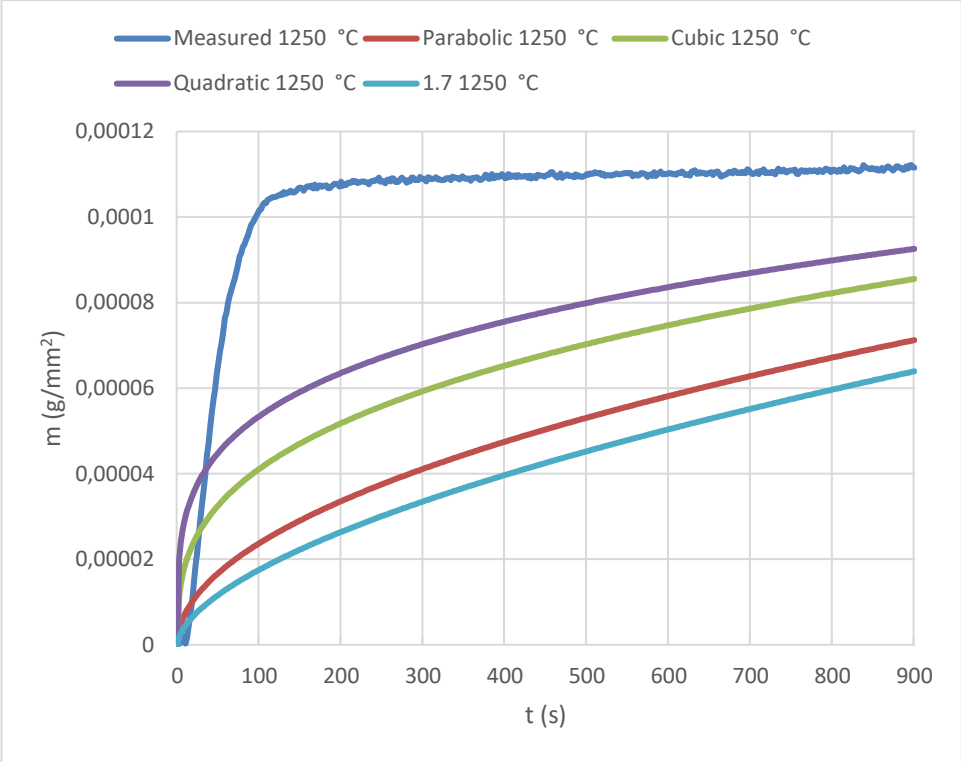

Figure 80. Comparison of measured and predicted scale growth calculated with all four models on AISI 309 at 1250 °C in the CH_4 Oxyfuel atmosphere.

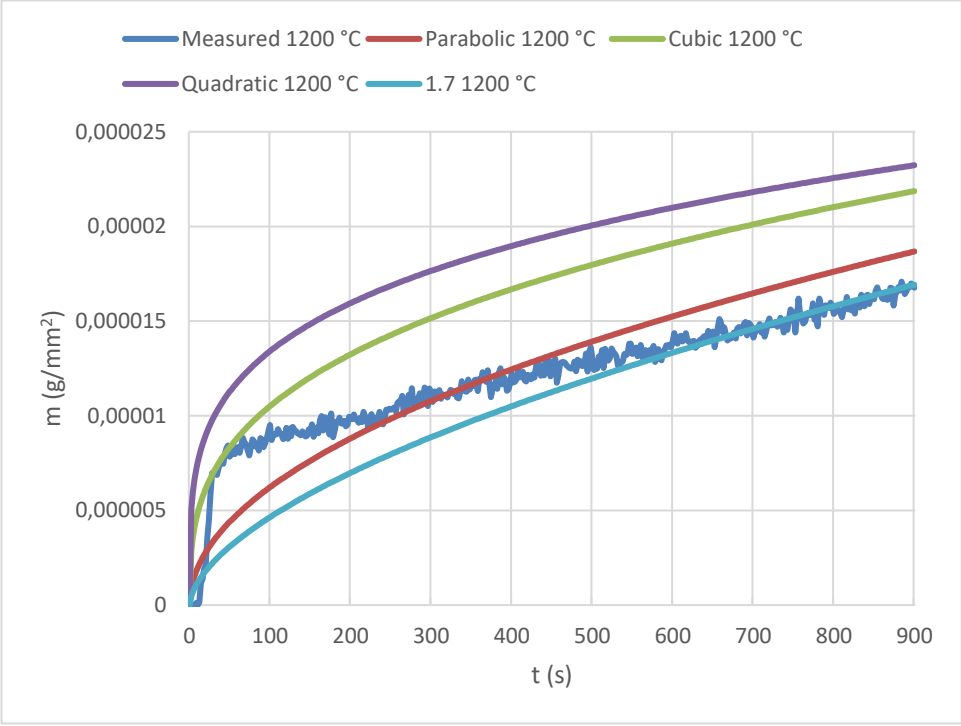

Figure 81. Comparison of measured and predicted scale growth calculated with all four models on AISI 309 at 1200 °C in the H_2 Oxyfuel atmosphere.

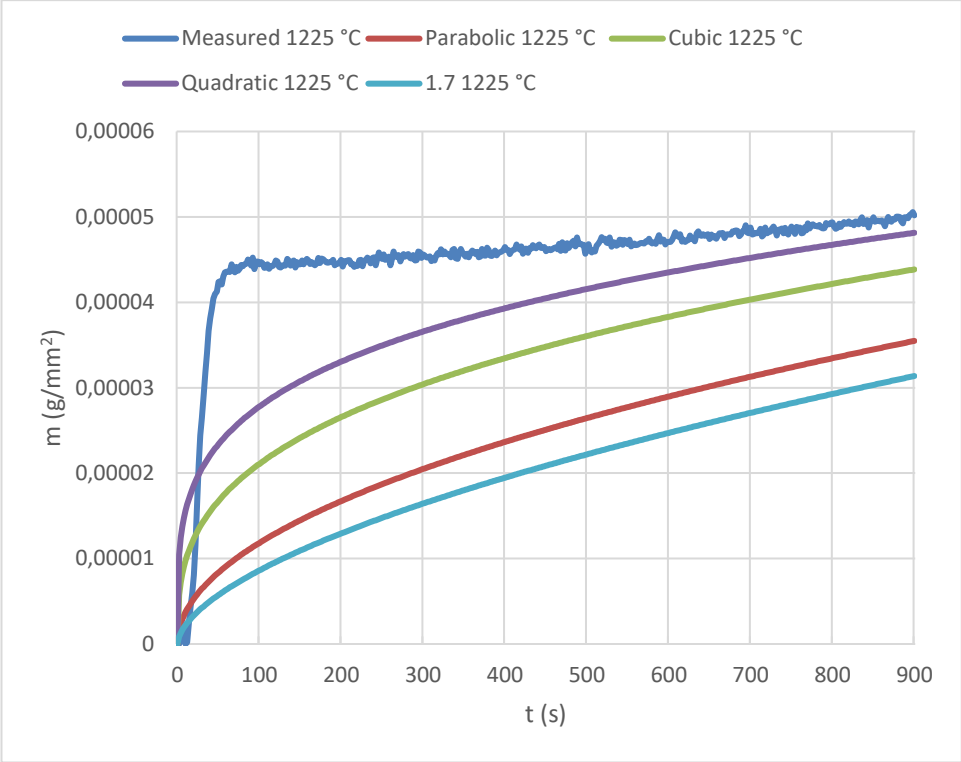

Figure 82. Comparison of measured and predicted scale growth calculated with all four models on AISI 309 at 1225 °C in the H_2 Oxyfuel atmosphere.

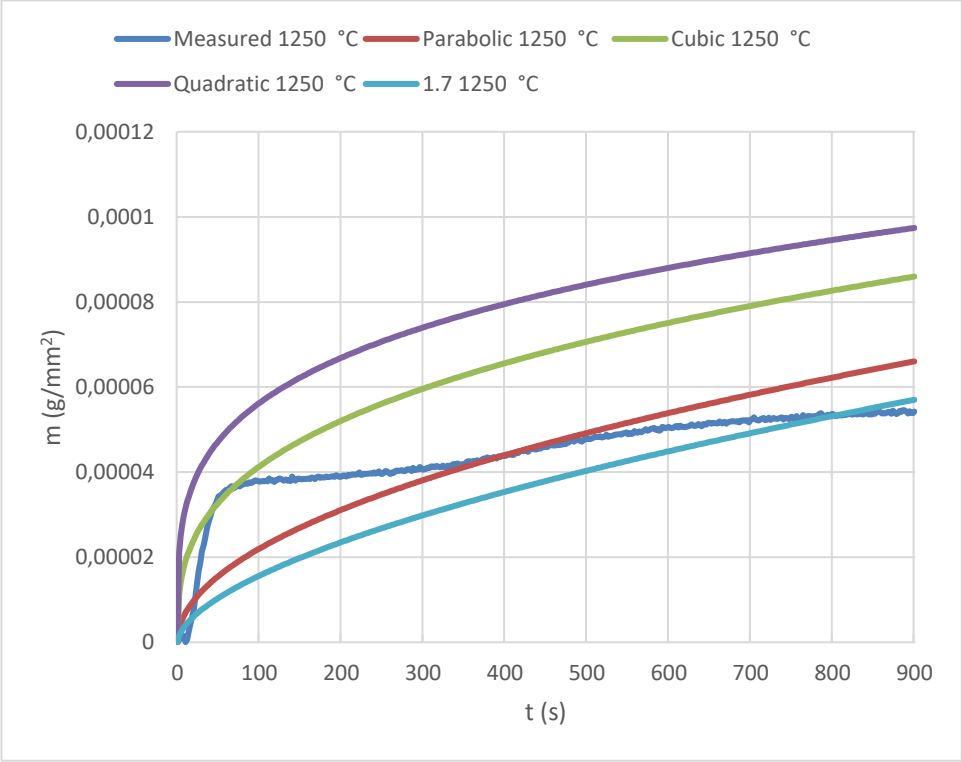

Figure 83. Comparison of measured and predicted scale growth calculated with all four models on AISI 309 at 1250 °C in the H_2 Oxyfuel atmosphere.

8. DISCUSSION

8.1 AISI 304

8.1.1 Experiments at different temperatures

The effect of temperature was studied in each atmosphere. In every case, a higher temperature caused more oxidation. This has been confirmed in earlier studies and discussed by e.g., Airaksinen et al. (2020). However, the gap between 1200 °C and 1225 °C annealing temperatures was much more significant than the gap between 1225 °C and 1250 °C. In **Figure 6.,** considering the CH_4 Air atmosphere, we can see a nudge early on into experiment A1.1 taking place at 1200 °C. No explanation was found for this, and the cause was not studied further due to its insignificance. The difference in scale formation caused by different temperatures is very clear in **Figure 6.** The case was not quite as clear in **Figure 7.** considering the experiments in the CH_4 Oxyfuel atmosphere, so the experiment conducted at the temperature of 1250 °C was repeated once more for a total of three experiments at this temperature. The third experiment, labelled E1, was nearly identical to the initial experiment A2.3. The difference in scaling is very clear when comparing 1200 °C to higher temperatures, but the gap between 1225 °C and 1250 °C was not quite as clear this time around. The amount of scale per surface area is very similar until around the 500 second mark. At the end of the experiment, however, the difference is quite clear. The third and last atmosphere, H_2 Oxyfuel, is depicted in **Figure 8.** Once again, the experiment performed at 1200 °C clearly differs from other experiments. However, the initial experiment at 1250 °C, labelled A3.3, gained lower oxidation per surface area than the experiment conducted at 1225 °C, labelled A3.2. The initial repeated experiment, labelled A3.3.5, oxidized the most out of all experiments conducted in the H_2 Oxyfuel atmosphere. Therefore, the experiments at 1250 °C were performed twice more. Out of these two experiments, the experiment labelled E4 performed similarly to the experiment conducted at 1225 °C, but experiment E2 was very similar to experiment A3.3.5. It was concluded, that experiments A3.3.5 and E2 are the most trustworthy results due to their higher scaling and similarity between one another.

The total scale gworth for every experiment conducted for AISI 304 is presented in **Table 3.** When we compare the total scale growth within each atmosphere, we can clearly see, that a higher annealing temperature causes more oxidation.

8.1.2 Experiments in different atmospheres

When it comes to studying the effect of atmosphere on scaling, the order in total scaling at the end of the experiments changed at every temperature. As we can see in **Figure 9.**, considering experiments taking place at 1200 °C, the H_2 Oxyfuel causes the most oxidation initially. The CH_4 Oxyfuel surpasses it at around the 200 second mark, and all three atmospheres meet at around the 50 second mark. After this, the CH_4 Air atmosphere, which caused the least amount of scaling initially, takes over, leading to highest amount of scale formed. After the 500 second mark the CH_4 Oxyfuel and H_2 Oxyfuel cause very similar amounts of scaling, with the CH_4 Oxyfuel causing just a little more oxidation in the end. When the annealing temperature rises to 1225 °C in **Figure 10.**, the order of the lines is very clear from the beginning all the way to the end. H_2 Oxyfuel causes the most scaling, but interestingly, CH_4 Air causes the lowest amount of scaling this time around. Due to a higher number of experiments conducted at 1250 °C annealing temperatures, **Figure 11.** was quite unreadable. Therefore, the number of experiments in each atmosphere was limited to one to produce a readable graph labelled **Figure 12.** H_2 Oxyfuel clearly caused more oxidation through the whole experiment, with CH_4 oxyfuel taking the ”second place.” However, at around the 750 second mark, CH_4 Air caught up to it causing just about the same amount of oxidation. The final scale amount for the CH_4 Oxyfuel experiment labelled A2.3.5 was approximately 0,000365 g/mm^2, whereas the amount for the experiment conducted in the CH_4 Air atmosphere labelled A1.3.5 was approximately 0,000364 g/mm^2. At the end of the experiments, at 900 seconds, the results between these two experiments were practically identically, and if given enough time, CH_4 Air could possibly surpass CH_4 Oxyfuel. For comparison, the experiment conducted in H_2 Oxyfuel caused a final scaling amount of 0,000394 g/mm^2, which is clearly a higher amount, but the difference is not too dramatic.

When we compare the final scale growth caused by atmosphere using **Table 3.**, we can see, that the CH_4 Oxyfuel caused the lowest amount of oxidation at 1200 °C, whereas the CH_4 Air causes the lowest amount of oxidation. When the annealing temperature rises to 1225 °C, the H_2 Oxyfuel atmosphere causes the highest amount of total oxidation, and CH_4 Air is again the one causing the least oxidation. At 1250 °C, the CH_4 Oxyfuel atmosphere causes the lowest amount of total oxidation, and the average oxidation amount of experiments conducted in H_2 Oxyfuel atmosphere is slightly higher than the singular experimental results of the experiment conducted in the CH_4 Air atmosphere.

8.2 AISI 309

8.2.1 Experiments at different temperatures

The results of the experiments performed on AISI 309 were not nearly as clear as with AISI 304. The results of the experiments conducted in the CH_4 Oxyfuel were the only clear ones out of the three atmospheres, and the results are presented in **Figure 16.** A higher temperature clearly caused more oxidation, and the difference between the initial and repeated experiments conducted at 1250 °C is not very significant. Therefore, there was no need to repeat any more experiments in the CH_4 Oxyfuel atmosphere. However, the two other atmospheres are a completely different story.

A total of nine experiments were conducted in the CH_4 Air atmosphere, which is over double the number of experiments conducted in the CH_4 Oxyfuel atmosphere. Two experiments were conducted at 1200 °C, and the same amount at 1225 °C. A total amount of five experiments were conducted at 1250 °C. All the results are presented in **Figure 13.** The repeated experiments conducted after the initial experiments produced wildly different results from the initial ones. These results were split into the initial ones labelled Bx and the later ones labelled Fx, and they are presented in **Figure 14.** and **Figure 15. Figure 14.** presents the results of the initial experiments. As expected, a higher temperature caused more oxidation. However, the results between the experiments

conducted at 1250 °C differed from one another far more significantly than in the CH_4 Oxyfuel situation discussed above. Therefore it was concluded that there was a need for further repeated experiments. For peace of mind, the experiments conducted at 1200°C and 1225 °C were repeated also. As mentioned above, the results of these experiments differed significantly from the initial experiments. This time around, the experiment conducted at 1200 °C, labelled F7, caused clearly the highest amount of scaling of the later repeated experiments. Also, the experiment F7 was the only one of the later experiments to cause more oxidation than their initial counterparts. When comparing F7 to the initial experiment conducted at 1200 °C, labelled B1.1, the difference is very significant. The final scaling amount of B1.1 was approximately 0.00004 g/mm^2, whereas the scaling amount for F7 was 0.000113 g/mm^2, which is more than 2.8 times higher. When we get to **Figure 15.** depicting the later experiments, the results are somewhat clear, if we ignore F7 conducted at 1200 °C. Experiment F9 conducted at 1225 °C causes lower oxidation than the three experiments at 1250 °C, as could have been expected. The difference between experiments F1 and F5 is less significant than with the initial experiments, B1.3 and B1.3.5, which sparked the need for more repeated experiments, However, experiment F3 differs from these two but once again, the difference is not as significant as with the initial experiments. It was decided, that the results of the initial experiments would be used for optimizing the scale growth model.

As with the CH_4 Air atmosphere, a significant difference between the results of the experiments conducted at 1250 °C, labelled B3.3 and B3.3.5, caused a need to perform more repeated experiments. The amount of experiments was the same as with CH_4 Air, two for each lower temperatures and a total of five for the highest temperature, 1250 °C. The results of all nine experiments are presented in **Figure 17.** As the graph presenting all the results is somewhat unreadable. the results were split again into initial and later experiments depicted in **Figure 18.** and **Figure 19. Figure 18.** presents the results of the initial experiments conducted on AISI 309 in the H_2 atmosphere. As could have been expected, the lowest temperature caused the least amount of oxidation. However, the experiment labelled B3.3 conducted at the annealing temperature of 1250 °C caused less oxidation than the experiment conducted at 1225 °C labelled B3.2. This, together with the significant difference between the results of the experiments conducted at 1250 °C, caused a need for further repeated experiments. The difference between B3.3 and the other experiment conducted at 1250 °C, B3.3.5, was quite significant: while experiment

B3.3 caused 0.000056 g/mm^2 of oxidation, the amount for B3.3.5 was 0.000114 g/mm^2. This was more than double than the first, initial experiment. As mentioned above, the results of the repeated experiments conducted later differed even more severely from the initial experiments. The results are presented in **Figure 19.** As we can clearly see, the shapes of the lines in the two graphs (figures **18.** are **19.**) are completely different. No explanation was found for this. However, the later repeated experiments conducted at 1250 °C are quite similar between the three. As with the initial experiments, the lowest annealing temperature caused the lowest amount of scaling. However, the experiment conducted at 1225 °C, labelled F10, caused the highest amount of oxidation initially. Two of the highest temperature experiments surpassed F10 at around the 400 second mark, and the final fourth one at around the 550 second mark. The higher initial oxidation could be caused by the dissolution of fayalite or some other factor. Therefore, it may not be due to bugs in the experimental equipment, measurement noise or other interference, but this is also possible. The final scaling amount of F10 is lower than all three of the experiments conducted at a higher annealing temperature, which was expected. As with the CH_4 Air atmosphere, it was decided, that the initial experimental results would be used in the optimization of the scale growth model.

Table 4. contains the total scale growth for each experiment conducted on AISI 309. The results are clear for the experiments conducted in the CH_4 Oxyfuel atmosphere, as a higher annealing temperature clearly causes a higher total amount of scale. For the H_2 Oxyfuel the results vary somewhat strongly, but by using averages we can come to the same conclusion. The results for CH_4 Air also vary, and when using averages, 1225 °C comes out as the least oxidizing annealing temperature. 1250 °C causes a higher average final scale growth than 1200 °C, but the different is not that great.

Due to the poor repeatability of the experiments conducted on AISI 309, it could be beneficial to repeat the experiments conducted in the CH_4 Air and H_2 Oxyfuel atmospheres several times. This would create a more reliable source for the optimization of the models, but this could not have been done within the time limits set for this thesis.

8.2.2 Experiments in different atmospheres

When comparing the three atmospheres in **Figure 20.**, at 1200 °C, the experiment F7 conducted in the CH_4 Air should be disregarded due to a much higher amount of oxidation. As mentioned above, F7 produced more than 2.8 times the scale compared to its counterpart, B1.1. When this is done, the two experiments conducted in CH_4 Oxyfuel (B2.1) and CH_4 Air (B1.1) produce the highest amount of scale per surface area, and are almost identical. At the end of the experiments B1.1 has gained slightly more scale, 0.00004 g/mm^2, compared to B2.1's 0.0000389 g/mm^2. Out of all the five experiments conducted at 1225 °C presented in **Figure 21.**, CH_4 Air caused the highest and lowest amount of scaling. This brings forth the poor repeatability of these experiments quite well. The former of the experiments conducted in the H_2 Oxyfuel atmosphere, B3.2, produces slightly more oxidation when compared to the only experiment conducted in the CH_4 Oxyfuel atmosphere, B2.2. Initially, B3.2 causes more oxidation, but B2.2 catches up to it at around 200 seconds. However, the later repeated experiment, F10, causes much less scaling than its counterpart. In this case, we should use the averages of the results of the experiments conducted in the CH_4 Air and H_2 Oxyfuel atmospheres. When comparing these averages to the CH_4 Oxyfuel experiment B2.2's final scale amounts to each other, we get a CH_4 Oxyfuel/ CH_4 Air/ H_2 Oxyfuel-ratio of of roughly 1.4/1/1. This means, that the CH_4 Oxyfuel atmosphere causes the most oxidation at 1225 °C, whereas the CH_4 Air and H_2 atmospheres cause roughly the same amount of final scaling. When comparing the results at 1250 °C, we have the results from twelve different experiments, As expected, **Figure 22.** depicting these results is quite hard to interpret. As mentioned above, the results of the initial experiments are used in optimizing the scale growth model, so three initial experiments are chosen to compare the effect of the atmosphere at 1250 °C. The three experiments chosen are B1.3, B2.3.5 and B3.3.5, and they are presented in **Figure 23.** The CH_4 Air atmosphere causes the least amount of oxidation initially, but surpasses the two atmospheres at approximately 150 seconds. Once again, H_2 Oxyfuel causes the most oxidation early on into the experiments, but CH_4 Oxyfuel surpasses it slightly at approximately 90 seconds. The final scale amounts for B2.3.5 and B3.3.5 are 0,000119 g/mm^2 and 0,000114 g/mm^2. The difference between these two is quite minimal. The final scaling amount of B1.3 is significantly higher, at 0,000203 g/mm^2.

We can use **Table 4.** to compare the final scale growth in each atmosphere at each temperature. When we use averages for experiments conducted at 1200 °C, the CH_4 Air atmosphere causes the highest amount of final scale growth, whereas the H_2 Oxyfuel is the one causing the lowest amount of oxidation. When 1225 °C is used as the annealing temperature, the H_2 Oxyfuel is again the one causing the lowest amount of total scale growth, but the difference when compared to the CH_4 Air atmosphere is just 0.000002 $\frac{g}{mm^2}$ on average. CH_4 Oxyfuel is the one causing the highest amount of final scale growth. When using the averages for 1250 °C, the differences are far clearer. CH_4 Oxyfuel causes the most total scale growth, whereas the H_2 Oxyfuel causes the lowest amount of oxidation in total.

8.3 AISI 441

8.3.1 Experiments at different temperatures

AISI 441 is a ferritic stainless steel, and it was annealed at appropriate temperatures, 950 °C, 1000 °C and 1050 °C, which were clearly lower than the ones used with austenitic steels. Due to lower temperatures the steel oxidizes far less, and this lower amount of formed scale is harder to measure. This, together with other interference, causes far more measurement noise in the thermogravimetric analysis experiments. Therefor, the graphs drawn from the results are far more difficult to interpret. Comparing the final scaling amounts is a good guess at best, for the noise is so great. Already at the first graph, **Figure 24.**, the measurement points have been reduced to 25 % of the original to create a readable graph. As could have been expected, the highest temperature (1050 °C) causes the highest amount of oxidation. The initial and repeated experiment are very similar with one another. Interestingly, the lower temperature of 950 °C seems to produce more oxidation than 1000 °C throughout the experiment. In the CH_4 Oxyfuel the results presented in **Figure 25.** are far more clear. As expected, the highest annealing temperature causes the most oxidation. However, the difference is quite significant, and the repeated experiment follows the initial one quite well. This time around, 1000 °C causes more scaling than 950 °C. The results of the experiments conducted in the H_2 Oxyfuel and

found in **Figure 26.** start to become clear at approximately 380 seconds. Once again, the highest temperature causes the most oxidation. However, the experiment conducted at 1000 °C labelled C3.2 surpasses the experiment C3.1 conducted at 950 °C only near the 750 second mark. The experiments conducted at 1050 °C produced very similar results.

The final scale growth amounts for experiments conducted on AISI 441 are found in **Table 5.** When comparing the final scale growth amounts, the results are clear and identical in each atmosphere: a higher temperature causes more total scale growth.

8.3.2 Experiments in different atmospheres

When comparing the results of different atmospheres at 950 °C, the measurement points had to be reduced to 25 % of the original to create a somewhat readable graph. The results are presented in **Figure 27.** The comparison is somewhat clear throughout the experiments: H_2 Oxyfuel causes the most oxidation, whereas CH_4 Oxyfuel is the one causing the least. However, due to measurement noise and possible interference, the measurement points of CH_4 Oxyfuel are found very often on the negative half of the y-axis, which means a negative weight gain. This is not completely impossible due to vaporization on components for example, but measurement noise and possible interference are the probable causes for this. When we move up to 1000 °C in **Figure 28.**, we notice that experiment C3.2 conducted in the H_2 Oxyfuel also spends most of the first 480 seconds on the negative half of the y-axis. At around 650 seconds it surpasses the CH_4 Air experiment in the amount of scaling, and the final result is clearly above C1.2 depicting the CH_4 Air experiment. However, at around the 500 second mark C2.2 depicting the CH_4 Oxyfuel experiment starts rising in a similar angle to C3.2 ending clearly above it, i.e. causing the highest amount of oxidation. **Figure 29.** depicting the results of the experiments at 1050 °C is very clear. It consists of six experiments, of which every one follows their counterpart quite well. CH_4 Oxyfuel causes significantly more oxidation than the two other atmospheres, whereas the CH_4 air takes the place of the one causing the lowest amount of scaling. All three atmospheres are quite evenly matched until aprroximately the 280 seconds mark, where CH_4 Oxyfuel rises above the other two.

They continue quite evenly until around the 450 second mark, after which H_2 starts to produce more oxidation, ending up clearly above the CH_4 atmosphere.

Table 5. can be used to compare the effect of atmosphere at each annealing temperature. At 950 °C, the H_2 Oxyfuel is the one causing the highest amount of final scale growth, whereas CH_4 Oxyfuel causes the lowest amount of total oxidation. At 1000 °C the results are very clear; CH_4 Oxyfuel causes the most total scaling, and CH_4 Air is the one causing the lowst amount of total scaling. The results at 1050 °C are similar to 1000 °C; CH_4 Oxyfuel is the highest oxidizing atmosphere in total scaling, and CH_4 Air is the least oxidizing one.

8.4 Microscopy

8.4.1 The effect of temperature on oxidation and a comparison between the CH_4 Air and H_2 Oxyfuel atmospheres

A FESEM image of three AISI 304 stainless steel samples annealed at three different temperatures for 15 minutes in the CH_4 Air is presented in **Figure 30.** As we can see, using a higher annealing temperature causes more oxidation. The cavities found in the oxide layer also shrink as the temperature rises, and the location of the old metal surface becomes more unclear. The intermediate in each sample can be split into two unequal parts in thickness in every sample. The part closer to the metal surface has a higher amount of metal, whereas more oxides have formed in the higher section. The amount of metal, pictured in white, decreases throughout the intermediate sections as the temperature rises, and is replaced by oxides, pictured in gray and black.

A similar image was produced for the H_2 Oxyfuel atmosphere, which is found in **Figure 31.** As expected, the lowest annealing temperature causes the least amount oxidation. Interestingly, the intermediate section between the metal and oxide layer seems thicker at 1225 °C than at 1250 °C. The former metal surface can be seen very clearly in all three temperatures. The amount of metal within the intermediate section is reduced when the temperature rises due to formation of oxides. There is no clear split into two or more parts in the intermediate section, although more oxides can be found closer to the oxide layer

The oxide layer seems to transform somewhat drastically. As the temperature rises, vertical cavities start to shrink and they seem to be non-existent at 1250 °C. When comparing the images from 1225 °C and 1250 °C, the amount of pores are higher at 1250 °C, but they are smaller in size, as if bigger pores had been broken into several smaller ones. Some sort of cracks and cavities can be seen in the oxide layer of the sample annealed at 1250 °C.

A side-by-side comparison between the CH_4 Air and H_2 Oxyfuel atmospheres is made in **Figures 32 - 34. Figure 32.** presents the FESEM images of samples annealed at 1200 °C. As we can see, the oxide layer formed in both atmospheres is very similar in thickness. However, the largest pores seem to be vertical in the sample annealed in the CH_4 Air atmosphere, whereas the one annealed in H_2 Oxyfuel has a much larger somewhat uniform horizontal pore. The old metal surface is easily visible in both cases, and there are similar pores in its close proximity. The intermediate section of the CH_4 Air sample is clearly thicker, but the composition is very similar, and the split into two separate sections is equally clear in both cases. The comparison made in the annealing temperature of 1225 °C is found in **Figure 33.** As we can see, the oxide layer is very similar between the two. The pores are similar in shape and size, and the old metal surface is very clear. The intermediate section formed in the H_2 Oxyfuel atmosphere is the thicker one this time around. The split into two sections is much clearer in the CH_4 Air atmosphere, and the higher section is clearly richer in oxides. The results of the highest and final annealing temperature comparison is presented in **Figure 34.** The pores found in the oxide layer of the sample annealed in the H_2 Oxyfuel atmosphere are clearly greater in number and size. The CH_4 Air oxide layer lacks the cracks of cavities found in its counterpart. The old metal surface is clear in both cases, although not as clear as in lower temperatures. As with the case of 1200 °C, the intermediate section is thicker in the CH_4 Air atmosphere. The split into two sections is much clearer than in colder annealing temperatures, and the CH_4 Air sample's higher section is much more rich in oxide than its H_2 Oxyfuel counterpart. Based on these images, the rise in annealing temperature seems to have a more linear effect in the CH_4 Air atmosphere than in the H_2 Oxyfuel atmosphere.

8.4.2 Effect of annealing time on scale growth on AISI 304 in the CH_4 Air atmosphere

The affect of annealing time on the scale growth on AISI 304 was studied in the CH_4 Air atmosphere at 1250 °C. Four different annealing times were used, which were one, five, ten and 15 minutes. The results are presented in **Figure 35.** for one and five minutes, and in **Figure 36.** for ten and 15 minutes. As we can see, the oxide layer formed after one minute of annealing is very thin. It resembles the intermediate sections of samples annealed for a longer period of time, as discussed above. When the annealing time is increased to five minutes, the oxidation is clearly stronger. Similar behaviour is also discussed by Ariaksinen et al. (2020). An oxide layer with small pores and an intermediate section can be separated from one another. The intermediate layer is rich in metal in the close proximity of the metal surface, and the amount of oxide increases towards the oxide surface. When the annealing time is double to ten minutes, the oxidation increases drastically. There is a thick oxide layer with large pores, and an even thicker intermediate section. The old metal surface is clearly visible. This intermediate section is also rich with metal in close proximity of the metal surface, with higher amounts of oxides when moving closer to the oxide layer. The final annealing time of 15 minutes differs from ten minutes mainly in the morphology of the oxide layer: large pores have vanished, and only small ones can be found. The intermediate section is similar in composition, and only slightly thicker. The old metal surface remains clear with all four annealing times.

8.4.3 Distribution of elements

The distribution of the five most significant elements (iron, chromium, oxygen, silicon and nickel) in the oxide layer and intermediate section was studied on AISI 304 annealed in the CH_4 Air atmosphere for ten and 15 minutes at 1250 °C using t. Each element was assigned their own colour, which are explained in the images. **Figure 37.** and **Figure 39.** present the sites of the EDS analyses in each sample. **Figure 38.** presents the distribution of elements in the sample annealed for ten minutes. Iron can be found throughout the sections, with a somewhat poor section found just below the oxide-intermediate section-interface. The black, completely ironless spots found in the oxide layer are pores. The

oxide layer is clearly richer in iron than the intermediate section. The oxide layer has very low amounts of chromium, whereas the intermediate section has quite a lot of it. Oxygen is found in every part of the image, excluding the pores. Unlike with iron, there is no oxygen-poor section. Silicon is spread throughout the image, although silicon content is low throughout the whole section. Silicon is found in greater quantities within proximity of the metal surface. Only very low amounts of nickel can be found in the oxide layer, and the intermediate section is also quite poor. A clear border can be seen between the two of them. **Figure 39.** presents the results for the annealing time of 15 minutes. The results are presented in **Figure 40.** The results are exactly same as in with the annealing time of ten minutes.

8.4.4 Chemical composition of oxides and metals using EDS

EDS Analysis was used to study the chemical compositions of intermediate zones and oxides of some of the samples. The results from samples A3.1 (AISI 304 annealed for 15 minutes at 1200 °C in the H_2 Oxyfuel atmosphere) and D3 (AISI 304 annealed for 10 minutes at 1250 °C in the CH_4 Air atmosphere) are presented in **Figure 41.** and **Figure 42.** with the chemical compositions listed in **Table 6.** and **Table 7.** In the images white areas are metal, and gray and black areas are oxides. It was assumed, that the spectrums studied composed only of oxygen, silicon, chromium, manganese, iron and nickel. The only way to be completely certain of the compositions of the spectres found in **Figures 41.** and **42.** is to study them by Wavelength-dispersive spectroscopy (WDS). Without WDS, only educated guesses can be made of the compostion of these spectres. As microscopic study was not the main aim of thesis, WDS-analysis was not performed.

Spectrums 29 and 30 found in **Figure 41.** are placed in the oxide area. When comparing their compositions found in **Table 6.**, we can see, that their composition differs mainly in chromium and iron. Both have under half a percent of silicon, around 1.6 % of nickel and little over 22 % of oxygen. The amount of chromium varies from around 24 % to around 33 %, and the amount of iron varies from around 39 % to around 48.5 %. Spectrums 31 and 32 are placed on metal. Their composition varies somewhat strongly excluding nickel and the non-existent silicon. The amount of oxygen varies from around 4 % to around 10

%, which is a somewhat large difference in percentages. The amount of chromium varies from around 7.5 % to around 12.5 %. There is also a significant difference in iron, as its amount varies from around 33 % to 43 %. Spectrum 9 found in **Figure 42.** is placed in metal. It has no oxygen, silicon or manganese present. According to **Table 7.**, it has a low amount of chromium, only around 5.5 %. It consists mainly of iron, around 70 %, with the rest being nickel, around 30 %. This adds to around 106 %, but there is a margin of error to be expected in this type of analysis. Spectrums 10-12 are placed in oxides. Based on their compositions found in **Table 7.**, they might be three complelety different oxides. Spectrums 10 and 11 differ from one another mainly in chromium and iron, as other elements accounted for are found in similar quantities. Spectrum 12 has nearly 20 % of nickel, which is not found in Spectrums 10 and 11. Spectrums 11 and 12 share a similar amount of iron. All three spectrums placed on oxide have a similar amount of manganese. Spectrum 12 is more rich silicon when compared to the other two, but is poor in oxygen and chromium in comparison.

8.5 Optimization of models

The results of experimental work were fitted to existing mathematical models. As mentioned above, four models were found suitable for the goals of this thesis. These models were the Parabolic, Cubic, Quadracic and the ”1.7”-model, which was iterated using Microsoft Excel’s Solver tool. Some other models were also studied, but found dysfunctional. As mentioned above, these models would not fit every single steel grade. The problem was present with the AISI 441 stainless steel grade due to low scaling amounts, measurement noise and possible interference. AISI 441 had trouble with the Parabolic and ”1.7”-models within the CH_4 Oxyfuel atmosphere and with all models within the H_2 Oxyfuel atmosphere. This problem was overcome for the Parabolic, Cubic and Quadratic models withing the H_2 Oxyfuel atmosphere by using the averages for every 50 measuring points, but this had no affect on the last three occasions. This also lead to the impossible calculation of activation energies and frequency factors for these models. This problem could, however, be overcome with more experimentation, as the results for failure was a negative slope value for one of the annealing temperatures. As mentioned

above, this would not fit the timeframe of this thesis, but could easily be verified given enough time and resources.

In order to fit the experimental results into the chosen models, the results of the TGA-experiments had to be raised to the power of each respective model, e.g. to the power of two (α^2) with the Parabolic model. These calculations are presented in odd numbered graphs between **Figures 43. – 59.** and in **Figure 60.** Arrhenius plots were also drawn in order to calculate the activation energies and frequency factors for each model within every steel grade and atmosphere. The Arrhenius plots are presented in even numbered graphs between **Figures 44. – 58.** and in **Figure 61.** The calculated activation energies are presented individually for every stainless steel grade and atmosphere in **Tables 8. – 15.**, and compiled together in **Table 16.** The calculated reaction rate constants are compiled in **Tables 17. – 19.**, one for each stainless steel grade between temperatures 1100 – 1300 °C. The reaction rate constants for AISI 304 are also compiled and presented in graphic form in **Figures 62. – 64.** The reaction rate constants for AISI 309 and 441 are not presented in graphic form due to their poor interpretability.

The predicted scale growth for AISI 304 annealed in the CH_4 atmosphere for 15 minutes at 1300 °C is presented in **Figure 65.** as an example. The temperature 1300 °C was not used as an annealing temperature in the experiments in this research, and therefore this is a prediction. This was done to demonstrate the possibility to extend the range of these models beyond the studied temperature range. As we can see, the model utilizing a higher power of the experimental results predicts a higher oxidation than one with a lower power, e.g. the Quadratic model (α^4) predicts a higher oxidation than the Cubic model (α^3).

Figures 66. – 83. present the comparison of each model and measured TGA-data for AISI 304 and AISI 309. The more linear the behaviour of the model is, the better the model works in predicting the scale growth in real world applications. **Figures 66. – 68.** present the comparison of models to the measured data of AISI 304 annealed in the CH_4 Air temperature. As we can see, every single model predicts a higher oxidation than measured during the experiments. The scale growth predicted by the 1.7-model is closest to the measured data for the most part, and is the closest to linear behaviour of the four models. According to these conclusions, the 1.7-model fits the CH_4 Air atmosphere best between 1200 – 1250 °C. **Figures 69. – 71.** depict the comparison of models to the measured data for AISI 304 in the CH_4 Oxyfuel atmosphere. Again, the 1.7-model is has the most lineat

behaviour at every temperature. However, none of the models follow the measured data as closely as in the CH_4 Air atmosphere. The H_2 Oxyfuel comparison for AISI 304 is presented in **Figures 72. – 74.** The 1.7-model has the most linear behaviour once again, but the Parabolic model follows the measured data somewhat better. **Figures 75. – 77.** present the comparison in the CH_4 Air atmosphere for AISI 309. For some reason, the 1.7- model predicts very low oxidation. The operation of the Parabolic model is similar at every temperature, and the behaviour is not that far off from linear. The Cubic and Quadratic models predict oxidation lower than measured at 1200 °C, but higher at 1225 °C and 1250 °C. Their behaviour is quite linear at 1200 °C, but less linear than the Parabolic model at 1200 °C. More conclusive results could be achieved with more experimentation. The models predict lower oxidation than measured in the CH_4 Oxyfuel for AISI 309 presented in **Figures 78. – 80.** The Quadratic model's prediction of amount of oxidation is closest to the measured data, but the 1.7-model has the most linear behaviour. Once again, more conclusive results could be achieved through more experimentation. The H_2 Oxyfuel differs from other atmospheres described above. Every model predicts lower oxidation than measured at 1225 °C, but 1200 °C and 1250 °C are similar when compared to one another. The shape of the measured curve is similar at all temperatures. The Cubic and Quadratic models predict higher oxidation than measured at 1200 and 1250 °C, but lower at 1225 °C. The 1.7-model has the most linear behaviour at all temperatures. The most linear behaviour for each atmosphere used to study AISI 304 and AISI 309 are presented below in **Table 20.**

Table 20. The models with the most linear behaviour in each atmosphere studied for AISI 304 and AISI 309 between annealing temperatures of 1200 – 1250 °C.

	AISI 304	AISI 309
CH_4 Air	1.7	Parabolic
CH_4 Oxyfuel	1.7	1.7
H_2 Oxyfuel	1.7	1.7

9. CONCLUSIONS

The aim of this study was to optimize the scale growth model of AISI 304, AISI 309 and AISI 441 stainless steels under simulated final annealing line conditions. A thermogravimetric analysis furnace was used to simulate conditions created in industrial furnaces where Liquid natural gas (LNG) was used as fuel and being burned with air and oxygen enriched air (Oxyfuel) and hydrogen used as fuel burned with enriched air (Oxyfuel). The used temperatures for austenitic stainless steels AISI 304 and AISI 309 were 1200 °C, 1225 °C and 1250 °C and for ferric stainless steel AISI 441 the temperatures were 950 °C, 1000 °C and 1050 °C. The annealing times for the main experiments were 15 minutes, and for the stopped experiments utilized in microscopic studies were one, five, ten and 15 minutes. The atmospheres were created by feeding air, water vapour, nitrogen, carbon dioxide and pure oxygen into the furnace through a preheater.

The thermogravimetric analysis results showed that a higher temperature causes more oxidation in most cases. The biggest variance was found in AISI 309 stainless steel, where in some cases, lower temperatures caused more oxidation. This could be due to the complex dissolution of fayalite, or some other factor. When it comes to different atmospheres simulated, there was not one clear atmosphere causing the most oxidation. Annealing time was also a factor when comparing atmospheres, for one atmosphere would start the experiments as the least oxidizing atmosphere, but would surpass the other two atmosphere before the end of the experiments. Also, high variance was found in the results of the AISI 309 experiments, as experiments in same temperatures and atmospheres would end up in completely different results. The low amount of oxidation on AISI 441 due to low annealing temperatures together with measurement noise and other possible interference caused the results to be highly unclear. This was, ofcourse, predicted beforehand, and the results were adjusted using averages for more clear results.

Microscopic analysis was performed using a FESEM in order to study some of the samples in order to compare the effect of atmosphere and annealing time. In addition, EDS analysis was performed on some of the samples to study the structure of the oxidized

areas within the samples and to portray the distribution of some of the most significant elements. No definite stronger oxidizing atmosphere was found when comparing the samples annealed in the CH_4 Air and H_2 Oxyfuel in each temperature. As expected, when studying the effect of annealing time, longer times caused more oxidation.

Different models befitting the aim of this study were researched, and a total of four models were found to operate well. Three of them were already studied and verified, and one was iterated using Microsoft Excel. No verification of this model was found in the research, although it may already have been studied elsewhere. Activation energies and frequency factors were calculated successfully for most cases, although more experimental work is needed for the models to fit all studied steel grades and atmospheres. The results were successfully implemented to thermodynamically calculate a predicted amount of scale formation for a range of temperatures in all studied atmospheres on AISI 304.

As a result of this study, the operation of four models can be implemented in optimizing the operation of an industrial scale final annealing furnace used in stainless steel production. However, further studies should be conducted on AISI 309 and AISI 441 to optimize these models even further.

10. FURTHER STUDIES

Due to the wide range of stainless steels in production today, in addition to new steel grades being created all the time, the implementation of the results of this study are very limited. Although, some steel grades share similar scaling behaviour, but the relation between these stainless steels and the implementation of these models is to be studied further. The methods of this study could, of course, be implemented in study of other stainless steel grades. Comparing these results between one another could also lead into the discovery of before unknown relations between different stainless steel grades.

More experimental work on AISI 309 and AISI 441 should be conducted in order to further validate the functionality of these models. Due to high variation, measurement noise and interference, a high number of experiments should be conducted in order to create more conclusive results. With AISI 309 the main interest is the significant difference in scaling behaviour. With AISI 441, the challenge is to find coherent scaling behaviour, perhaps through the use of average values from several experiments. Also, the results of these collected average values could be averaged between every 10, 20, 50 etc. steps in order to create functional results.

11. REFERENCES

Airaksinen, S. 2019. Hilseen muodostuminen ruostumattoman teräksen hehkutuksessa

Airaksinen S., Tuovinen T., Laukka A., Vuolio T., Heikkinen E-P., Riekki E., Manninen T., Fabritius T. 2020. Effect of simulated annealing conditions on scale formation and neutral electrolytic pickling

Atkinson, A. 1988. Wagner theory and short circuit diffusion

Berthod, P. 2005. Kinetics of High Temperature Oxidation and Chromia Volatilization for a Bimary Ni-Cr Alloy. Oxidation of Metals, Springer Verlag, 2005, 64 (3-4), pages 235-252.

Center For Material Analysis, https://www.oulu.fi/cmnt/node/15439 [Cited on 11.5.2021]

Ermoline, A., Dreizin, E. 2011. Equations for the Cabrera-Mott kintics of oxidation for spherical nanoparticles. Chemical Physics Letters Vol. 505, pages 47-50.

Hosseini, A. 2020. Numerical study of inlet air swirl intensity effect of a Methane-Air Diffusion Flame on its combustion characteristics

Martin, J.W. 2007. The Chemical Properties Of Materials. 423-430.

Metalcor, 2021, date of publication unknown, AISI 304 datasheet, https://www.metalcor.de/en/datenblatt/5/ [Cited on 23.4.2021]

Metalcor, 2021, date of publication unknown, AISI 309 datasheet, http://www.metalcor.de/en/datenblatt/56/ [Cited on 23.4.2021]

Metalcor, 2021, date of publication unknown, AISI 304 datasheet, https://www.metalcor.de/en/datenblatt/25/ [Cited on 23.4.2021]

Metallin jalostajat ry. 2014. Teräskirja (9). Helsinki, 65-67. ISBN 978-952-238-120-0

North American stainless, 2021, date of publication unknown, AISI 304, AISI 304 L and AISI 304H datasheet,

https://www.northamericanstainless.com/wp-content/uploads/2010/10/Grade-304-304L-304H.pdf [Cited on 1.7.2021]

North American stainless, 2021, date of publication unknown, AISI 309S datasheet,

https://www.northamericanstainless.com/wp-content/uploads/2010/10/Grade-309S.pdf [Cited on 1.7.2021]

North American stainless, 2021, date of publication unknown, AISI 441 datasheet, https://www.northamericanstainless.com/wp-content/uploads/2010/10/Grade-NAS441-NAS-18CrCb.pdf [Cited on 1.7.2021]

Ohta, N., Yanagishima, F., Kaihara, T., Kishida, A., Sato, K., Ochiai, M. 1987. Continuous annealing and pickling method and apparatus for steel strips. US4713154A. United States of America. 8-11 s.

https://patentimages.storage.googleapis.com/c8/7f/56/dcc7559571f490/US4713154.pdf

[Cited on 11.5.2021]

Palosaari, M. 2020. Ruostumattomat teräkset ja niiden kuuma- ja kylmävalssaus

Metallien valmistus Suomessa -seminaari. Oulu, 56.

Patel V., Shah R. 2018. Experimental investigation on flame appearance and emission characteristics of LPG inverse diffusion flame with swirl

Xu, Z., Rosso, K.M., Bruemmer, S. 2012. Metal oxidation kinetics and the transition from thin to thick films. Physical Chemistry Chemical Physics Vol. 14.